Structure and dynamics of calcium aluminosilicate melts

Jad Kozaily

▶ **To cite this version:**

Jad Kozaily. Structure and dynamics of calcium aluminosilicate melts. Other. Université d'Orléans, 2012. English. NNT : 2012ORLE2003 . tel-00717373

HAL Id: tel-00717373
https://theses.hal.science/tel-00717373

Submitted on 12 Jul 2012

HAL is a multi-disciplinary open access archive for the deposit and dissemination of scientific research documents, whether they are published or not. The documents may come from teaching and research institutions in France or abroad, or from public or private research centers.

L'archive ouverte pluridisciplinaire **HAL**, est destinée au dépôt et à la diffusion de documents scientifiques de niveau recherche, publiés ou non, émanant des établissements d'enseignement et de recherche français ou étrangers, des laboratoires publics ou privés.

UNIVERSITÉ D'ORLÉANS

ÉCOLE DOCTORALE SCIENCES ET TECHNOLOGIES

LABORATOIRE : INSTITUT LAUE LANGEVIN / CEMHTI

THÈSE présentée par :

Jad KOZAILY

soutenue le : **26 janvier 2012**

pour obtenir le grade de : **Docteur de l'université d'Orléans**

Discipline : **Sciences des Matériaux**

Structure et dynamique d'aluminosilicates de calcium fondus

THÈSE dirigée par :

Louis HENNET	Ingénieur de Recherche, CEMHTI - Orléans

RAPPORTEURS :

Andreas MEYER	Professeur, DLR – Cologne, Allemagne
Noel JAKSE	Professeur, SIMAP - Grenoble

JURY:

Dominique MASSIOT	Directeur de Recherche, CEMHTI – Orléans, Président
Andreas MEYER	Professeur, DLR - Cologne, Allemagne
Noel JAKSE	Professeur, SIMAP - Grenoble
Salvatore MAGAZU	Professeur, Université de Messine, Italie
Henry FISCHER	Chercheur, ILL - Grenoble
Louis HENNET	Ingénieur de Recherche, CEMHTI - Orléans

ACKNOWLEDGMENTS

First I would like to thank my thesis supervisor, Louis Hennet, for finding funding and offering me the possibility to finish this thesis under his supervision, for his continuous support during the complete thesis time as well as for introducing me into this very interesting field of physics and to the levitation technique.

I would also like to thank my secondary supervisors at the ILL: Henry Fischer and Marek Koza. Henry Fischer for being always next to me, giving me not only professional but personal advice too, for his tremendous general and scientific knowledge from which I learned a lot. Marek Koza for keeping his door always opened for me, answering my questions and for providing all the help to make sure my first experiment works.

I thank Prof. Andrew Harrison, director of ILL, for trusting and appreciating my research work and providing me support and funding to go and visit/work in foreign international labs such as the German Aerospace Center and the European Space Agency. I would like to thank as well Juan Rodriguez-Carvajal, head of the diffraction group, for welcoming me in his group and providing all the available means.

I am also indebt to my collaborators: Salvatore Magazù (Università di Messina, Italy) and Florian Kargl (Deutschen Zentrums für Luft und Raumfahrt DLR, Cologne, Germany) for their insightful conversations during the development of the ideas in this work. Daniel Neuville (Institut de physique du globe de Paris, France) for his generous provision of samples and fruitful discussions.

Essential to this research are the instrument scientists and technicians who have helped me run my experiments at the various central facilities used. At ILL, I would particularly like to thank Marek Koza, Richard Ammer (who taught me machining) and Steve Jenkins (IN6), Henry Fischer and Alain Bertoni (D4), Eddy Lelièvre-Berna, Paul Martin and Frederic Marchal (Sample Environment). At the ESRF, I would like to thank Giulio Monaco and Valentina Giordano (ID16), Aleksei Bytchkov and Loredana Erra (ID11).

I have had the good fortune to have: Prof. Andreas Meyer (Director of the Institut for Materials Physics in Space, DLR, Germany), Prof. Salvatore Magazù (Università di Messina, Italy), Dr. Dominique Massiot (Director of CEMHTI, Orléans) and Prof. Noel Jakse (SIMAP, Grenoble) on my thesis defense jury.

Finally, I would like to thank all of my family and friends for never giving up on me and for consistently telling me that I would be a doctor one day!

CONTENTS

LIST OF FIGURES

LIST OF TABLES

INTRODUCTION (FRANÇAIS)

Comprendre la structure et la dynamique des aluminosilicates de calcium (CAS) dans leurs états vitreux et liquide présente un grand intérêt pour diverses applications technologiques ou géologiques.

En sciences de la terre, l'importance de bien comprendre la structure et la dynamique des silicates fondus découle du fait que le silicium et l'oxygène sont les deux éléments les plus abondants dans la croûte et le manteau terrestre. Avec la vapeur d'eau, ils constituent le magma qui monte vers la surface de la terre par activité volcanique. Ce sont principalement les silicates qui déterminent la viscosité du magma et donc sa capacité à s'écouler. Les variations observées de la viscosité ont abouti à l'un des systèmes de classification des laves le plus répandu: basaltiques, andésitiques et rhyolitiques, dans l'ordre croissant de leur composition en silicium. La lave basaltique forme de longues rivières, comme ce qui se produit typiquement dans les éruptions volcaniques hawaïennes, alors que la lave rhyolitique tend à éclater en raison de sa forte viscosité. Dès qu'elle atteint la surface de la terre ou bien le fond de l'océan et en fonction de sa composition chimique, la lave commence à se refroidir et à se solidifier en différents types de roches et de verres. Il est donc important de pouvoir étudier les propriétés des silicates fondus à haute température afin de mieux comprendre et modéliser les propriétés du manteau terrestre.

Du point de vue industriel, les verres CAS sont également des matériaux attirants pour de nombreuses applications en raison de leur caractère réfractaire et leurs très bonnes propriétés optiques et mécaniques. Quelques compositions vitrifiables de ce système ternaire sont des matrices potentielles pour le confinement des déchets nucléaires. Ces verres présentant des propriétés structurales intéressantes de ce point de vue. Le traitement des combustibles usés consiste d'abord en une séparation des éléments valorisables tels que l'uranium ou le plutonium. Les déchets de haute activité sont ensuite incorporés dans une matrice vitreuse en vue d'un stockage ultérieur. Le choix du verre pour confiner durablement les déchets nucléaires vient de la capacité du réseau vitreux à incorporer une très large variété d'espèces chimiques. Sa structure désordonnée permet non seulement l'incorporation à l'échelle atomique de la quasi-totalité des éléments contenus dans la solution de produits de fission,

mais elle est capable de s'adapter aux différences de composition de cette dernière en gardant toujours une bonne homogénéité et une bonne stabilité chimique et thermique.

Bien que les verres soient fabriqués depuis des millénaires, les phénomènes de surfusion et de transition vitreuse sont encore mal connus et l'étude des mécanismes microscopiques qui régissent le comportement complexe dans les liquides en surfusion est encore actuellement un défi. En particulier, ce domaine fait partie des problèmes non encore complètement résolus de la physique de la matière condensée. Une telle compréhension peut être obtenue à partir de l'étude de l'évolution des propriétés structurales et dynamiques des liquides, non seulement dans leur régime stable au-dessus du point de fusion, mais aussi dans leur état métastable comme la surfusion.

Un paramètre important lors de formation des verres est la viscosité du système et son évolution avec la température. En particulier son comportement proche de la température de transition vitreuse se caractérise par un terme de « fragilité » du système qui dépend bien sûr de la composition. L'objectif principal de ce travail est donc de comprendre et d'expliquer l'évolution de la fragilité de différents CAS fondus dans le diagramme de phase $(CaAl_2O_4)_{1-x} - (SiO_2)_x$ en fonction de leur composition x en SiO_2 et de considérer le rôle de l'ordre à courtes et moyennes distances dans l'évolution des propriétés dynamiques.
Le but de cette thèse est donc d'essayer de fournir une description des propriétés structurales et dynamiques des systèmes CAS et d'acquérir de nouvelles connaissances dans des phénomènes importants qui peuvent survenir dans les états liquide et surfondu, c'est-à-dire l'augmentation brusque de la viscosité qui accompagne la surfusion. Pour atteindre ces objectifs, nous avons utilisé et développé des équipements sophistiqués utilisant des techniques sans contact sur les grands instruments (synchrotrons et sources de neutrons). En particulier, des mesures de diffusion quasi-élastique de neutrons (QENS) ont été effectuées pour la première fois sur des aluminosilicates de calcium en lévitation aérodynamique.

Cette thèse comprend ainsi deux aspects complémentaires : un coté développements instrumentaux (i) et un coté expérimental (ii).

(i) Développements instrumentaux.

Cette partie comprend:

- Le développement d'un nouveau montage de lévitation aérodynamique conçu spécialement pour permettre la diffusion quasi-élastique des neutrons sur l'instrument IN6 à l'ILL (Institut Laue Langevin, Grenoble).

- Le développement d'une nouvelle technique de lévitation aérodynamique à multi-buses qui permet de mieux contrôler la position de l'échantillon.
- L'optimisation du montage de lévitation aérodynamique utilisé sur l'instrument D4C à l'ILL pour la diffraction des neutrons aux grands angles.

(ii) Etude experimentale.

Toute la partie expérimentale a été effectuée à l'ILL et à l'ESRF (European Synchrotron Radiation Facility, Grenoble). En particulier, plusieurs instruments ont été utilisés:

- IN6 (spectromètre en temps-de-vol) pour la diffusion quasi-élastique des neutrons afin d'examiner les processus de relaxation.
- ID16 (diffusion inélastique des rayons X) pour étudier la dispersion et la viscosité longitudinale.
- D4C (diffraction des neutrons) et ID11 (diffraction des rayons X) pour l'étude structurale.

Cette thèse est organisée en cinq parties.

Le **chapitre 1** rappelle brièvement les concepts fondamentaux des liquides et des verres et décrit plus en détail le système CAS, objet de cette étude.

Le **chapitre 2** décrit le nouveau dispositif de lévitation aérodynamique avec chauffage laser qui a été développé dans le cadre de la thèse et utilisé pour effectuer les mesures QENS. Une évolution du dispositif de lévitation permettant de mieux contrôler la position de l'échantillon est aussi présentée.

Le **chapitre 3** est une introduction aux principes de base de la diffusion des rayons X et des neutrons et définit les principaux paramètres et fonctions qui sont utilisés dans la thèse.

Le **chapitre 4** présente les résultats structuraux obtenus par diffraction de neutrons et de rayons sur ce système CAS.

Le **chapitre 5** constitué de deux parties, détaille l'étude de la dynamique effectuée par diffusion quasi-élastique des neutrons et diffusion inélastique des rayons X.

Une **conclusion** générale rappelle les principaux résultats obtenus dans ce travail et propose plusieurs pistes de continuation.

INTRODUCTION

Benefits

Understanding the structure and dynamics of calcium aluminosilicates (CAS) glasses and melts is of great interest for various technological or geological applications.

In earth sciences, the importance of understanding the structure and dynamics of molten silicates arises from the fact that silicon and oxygen are the two most abundant elements that are present in the Earth crust and mantle. Along with water vapour, they constitute the magma which rises toward the Earth's surface through volcanic activity and where mainly the silicates determine its viscosity and thus its capacity to flow. Variations in viscosity have resulted in one of the most commonly used classification systems of lava: basaltic, andesitic and rhyolitic, in order from least to greatest silicate content. Basaltic lava form long rivers, such as those that occur in typical Hawaiian volcanic eruptions, whereas rhyolitic lava tends to erupt explosively because of its poor fluidity. As soon as it reaches the surface of the earth or the ocean floor, the lava starts to cool and solidify into different types of rock and glasses, according to its original chemical composition. Studying the properties of high temperature silicate melts is then very important to better understand and model the Earth's properties.

For the industrial side, CAS glasses are also attractive materials for a wide range of technical applications due to their highly refractory nature, their very good optical and mechanical properties, and some glasses in this ternary system are promising materials for containing and storing nuclear waste. They have interesting structural properties in this matter. In a nuclear waste treatment, valuable elements (like Uranium and Plutonium) are first separated from other fission products. Highly active waste is then incorporated into glass matrices for ultimate long period storage. In fact, glasses have the ability to incorporate a wide variety of chemical species due to their random atomic arrangement and networking. Its disordered structure allows it to adapt to the different compositions of the incorporated fission products while always maintaining a good homogeneity, chemical and thermal stability.

Objectives

Although the phenomena of supercooling and the glass transition have been known for millennia, the microscopic mechanisms that govern the complex behaviour in supercooled liquids are still currently a challenge. In particular, the complex behaviour of viscous liquids and the nature of the glass transition itself are recognized as important, unsolved problems in condensed matter physics. Such an understanding can be obtained from studying the evolution of structural and dynamical properties of such liquids not only in the stable regime above the melting point, but also in the metastable supercooled (or undercooled) regime down to the grass transition.

The objective of the present study is to understand the "fragility" of various CAS melts in the phase diagram $(CaAl_2O_4)_{1-x} - (SiO_2)_x$ as a function of the composition x of SiO_2 and to consider the role of Short Range Order (SRO) and Medium Range Order (MRO) in their dynamical properties.

The aim of this thesis project is thus to try to provide a description of the structural and dynamical properties of CAS systems and to gain new insights in important phenomena that may occur within the liquid and supercooled states, i.e. the extraordinary viscous slow-down that accompanies supercooling. To attain these objectives, we will use and develop sophisticated experimental equipment making use of containerless techniques at large-scale facilities (synchrotron and neutron sources). In particular, Quasi Elastic Neutron Scattering (QENS) measurements are performed for the first time on aerodynamically levitated liquid CAS.

This thesis can be seen as comprising two complementary aspects (i) instrumentation development, and (ii) scientific studies:

(iii) Instrumentation developments

This part includes:

- The development of a new version of the levitation apparatus that enables the study of high temperature liquids by neutron time-of-flight spectroscopy.
- The development of a novel aerodynamic levitation technique that have more control on the levitated sample's height.
- The optimization of the existing laser-heated aerodynamic levitation setup at the D4C instrument used for Wide Angles Neutron Scattering at the ILL.

(iv) Scientific studies

The experimental work was mainly carried out at the ILL and the ESRF at the European Photon and Neutron (EPN) campus in Grenoble, France. In particular, various instruments were used:

- IN6 (time-of-flight spectrometer) for QENS experiments towards the study of the relaxation dynamics.
- ID16 (Inelastic X-ray Scattering (IXS) beamline) to investigate the dispersion and the longitudinal viscosity.
- D4C (neutron diffractometer) and ID11 (synchrotron x-ray diffractometer) for the structural investigations.

Thesis Layout

This thesis is divided into five chapters:

Chapter 1 gives a brief review on the fundamental concepts of liquids and glasses and describes the CAS system that has been studied in this work.

Chapter 2 describes the new aerodynamic levitation setup that was used in our QENS experiments. The technical developments brought by the present work to the aerodynamic containerless technique are also presented.

Chapter 3 provides a basic introduction to neutron and x-ray scattering, including the definition of useful correlation functions.

Chapter 4 presents the structural results obtained from neutron and x-ray diffraction on the CAS systems.

Chapter 5 presents the dynamical study results from the QENS and IXS measurements. The outcome of each technique is presented and discussed separately.

Finally, we give a general conclusion with recommendations for future work.

Résumé du Chapitre 1

Dans ce chapitre on trouvera une introduction aux principales caractéristiques de la phase vitreuse qui souligne les particularités de cet état de la matière condensée qui sont à la base de l'intérêt de notre étude. On trouvera aussi une vue générale et les notions de base nécessaires à la compréhension de la structure à l'échelle atomique et des propriétés dynamiques des liquides et des verres, ainsi qu'un résumé des principales propriétés des verres CAS étudiés.

Nous présentons, tout d'abord, les notions de transition vitreuse, température de transition vitreuse et viscosité qui caractérise un verre. La partie suivante décrit la structure des liquides en termes de fonction de corrélation de paires et de sa transformée de Fourier, le facteur de structure, qui est mesuré expérimentalement dans ce travail. Le lien avec les interactions interatomiques au travers de l'hamiltonien est discuté. Les propriétés dynamiques sont ensuite abordées avec les fonctions de corrélation temporelles et la fonction de Van Hove qui est considérée comme une quantité centrale. La transformée de Fourier de cette dernière, le facteur de structure dynamique, est la quantité mesurée dans le cadre de ce travail. Ce chapitre traite aussi le problème de la dynamique du verre et nous introduisons le concept de fragilité au travers des notions de temps de relaxation, les coefficients cinétiques, la viscosité et la diffusion.

La dernière partie de ce chapitre détaille l'intérêt d'étudier les CAS et décrit leurs propriétés structurales et la notion d'oxygène pontant et non pontant. La variation non-linéaire de la température de transition vitreuse en fonction de la composition est évoquée. Nous montrons aussi, dans le cas d'un verre d'aluminate de calcium, que les changements structuraux sont observables par des mesures résolues en temps et mettent en évidence une évolution de l'ordre à courtes et moyennes distances au cours du refroidissement. A la fin de cette partie, nous détaillons les différentes compositions CAS étudiées dans ce travail.

CHAPTER 1

1 SCIENTIFIC BACKGROUND

In this chapter, the fundamental concepts of the liquid structure and dynamics are introduced. The compositions of our samples are presented in the last section.

1.1 The Glass Transition

Although glass is known to be one of the oldest materials in humanity, a comprehensive and detailed description of its structure and properties is yet not clear. This is due to its disordered nature, where unlike crystals, glasses are amorphous solids that lack the periodicity and Long Range Order (LRO), while retaining various degrees of Short Range Order (SRO).

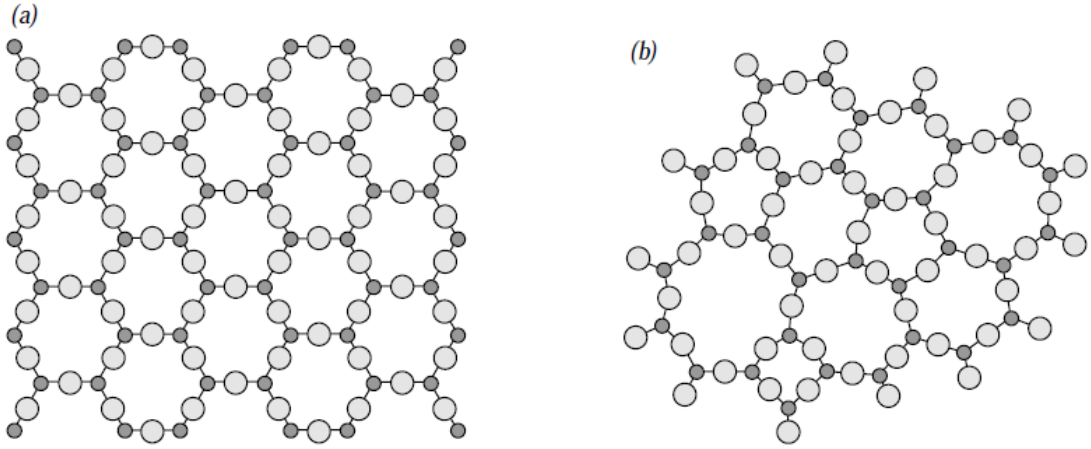

Figure 1.1 Schematic drawing depicting a two-dimensional oxide structure in its crystalline phase (a) and amorphous one (b).

Glassy materials are generally obtained by fast quenching from the liquid. While cooling, the liquid first undergoes what is called supercooling (or undercooling), whereby a liquid is cooled metastably below its melting point.

During cooling, the liquid rearranges progressively as a function of temperature and the system is then called "relaxed". As the temperature decreases, the molecules start to lose their mobility and the viscosity of the liquid increases gradually. If the nucleation rate is high enough, the liquid would then crystallize through an equilibrium first-order phase transition. However, if we quench the liquid fast enough, the molecules will lack the time to rearrange in equilibrium with temperature and end up by "freezing" in their metastable state. For this reason, glasses are structurally very similar to their liquid precursors.

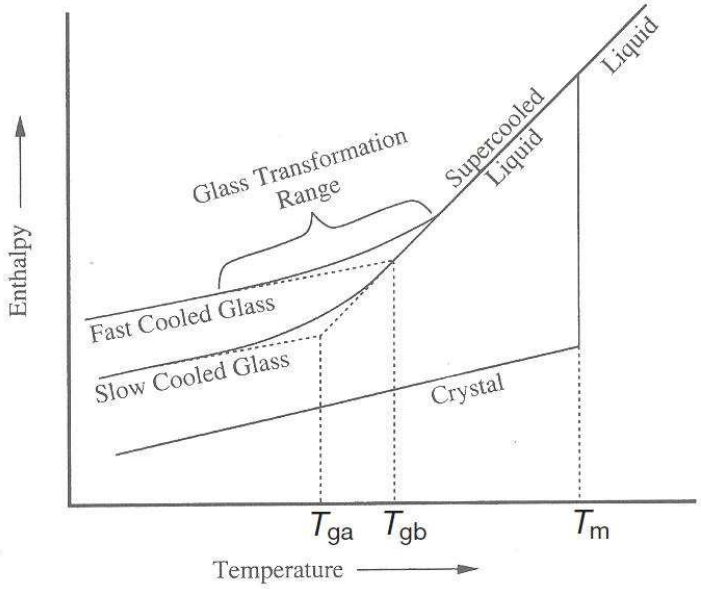

Figure 1.2 Temperature dependence of a liquid's enthalpy at constant pressure. T_m is the melting temperature. A slow cooling rate produces a glass transition at T_{ga}; a faster cooling rate leads to a glass transition at T_{gb} [1].

For silicate glasses, a cooling rate between one and ten Kelvin per second is sufficient to reach the glassy state. Whereas for some alloys for example, quench rates of up to 10^6 kelvin per second are needed to bypass crystallization.

The temperature T_g at which equilibration becomes unlikely is called the glass transition temperature. Experimentally, T_g is usually defined as the temperature at which the shear viscosity, η, reaches a threshold $\eta(T_g) = 10^{12}$ Pa.s (10^{13} poise). This viscosity corresponds to a characteristic relaxation time of 100s.

Clearly, T_g depends on the conditions under which the quench is performed and is thus subject to convention. It can be seen from Fig. 1.2 that a slower cooling will result in a lower T_g and a

more “ordered” glass [2]. The supercooled state refers to the liquid state ranging between the melting and the glass-transition temperature.

1.2 Structure of Liquids

Unlike crystals, the microscopic structure of liquids is generally defined in terms of probabilistic atomic distribution functions [3,4]. These comprise statistical averages of microscopic quantities that involve the positions and the momenta of the constituent particles. Since liquids are disordered, isotropic and generally homogeneous systems, their structure is limited to the Short and Medium Range Order (SRO & MRO) around each atomic species.

Experimentally, an accessible quantity that gives us the positional correlation between nearest neighbours is the Static Structure Factor $S(Q)$. Through a Fourier Transform (FT) of $S(Q)$, we get the so called Pair Distribution Function (PDF), denoted by $g(r)$, which describes the local environment within the liquid. $g(r)$ is in fact the probability to find an atom at a distance r from another taken at the origin. In the following, we will see how we derive these basic structural quantities, which are remarkably similar but surely have different physical meaning.

We first consider the case of a mono-atomic liquid (i.e. one chemical species Z), where we have a fixed number of particles N brought to equilibrium at the temperature T. The thermodynamic properties of the system are driven by both the thermal motion of the atoms and the interaction between the atoms. In the classical model of liquids, these two contributions can be separated into kinetic and potential terms, K_N and V_N respectively. The Hamiltonian of our model can be written as the sum of both energies as follow:

$$H = (1/2m)\sum_{\mathrm{i}} p_{\mathrm{i}}^2 + V_{\mathrm{N}}(\mathbf{r}_1,...,\mathbf{r}_{\mathrm{N}}) \tag{1.1}$$

Where m and $p_{\mathrm{i}}^2 = m^2 v_{\mathrm{i}}^2 = 3mk_{\mathrm{B}}T$ are the particle’s mass and momentum respectively. If we consider the pairwise approximation, whereby only two atoms at a given time are allowed to interact together, the potential energy is then expressed as the sum of the pairwise contributions,

$$V_N(\mathbf{r}_1,...,\mathbf{r}_{\mathrm{N}}) = \frac{1}{2}\sum_{\mathrm{i}\neq\mathrm{j}} \phi(r_{\mathrm{ij}}) \tag{1.2}$$

Where $\mathbf{r}_{\mathrm{i}}$ is the position of atom i, ϕ is the pair potential of spherical symmetry and $r_{\mathrm{ij}} = \left|\mathbf{r}_{\mathrm{i}} - \mathbf{r}_{\mathrm{j}}\right|$ is the distance between the i^{th} and j^{th} atoms. In general, the r_{ij} are a function of time which we will consider in the next section. We consider the number density $\rho_0 = N/V$ which represents the number of atoms per unit volume. The internal energy of the system is given by

$$
\begin{aligned}
E = \langle H \rangle &= (1/2m)\sum_{\mathrm{i}} \langle p_{\mathrm{i}}^2 \rangle + \langle V_{\mathrm{N}}(\mathbf{r}^{\mathrm{N}}) \rangle \\
&= \frac{3}{2} N k_{\mathrm{B}} T + \frac{1}{2} \left\langle \sum_{\mathrm{i} \neq \mathrm{j}} \phi(r_{\mathrm{ij}}) \right\rangle \\
&= \frac{3}{2} N k_{\mathrm{B}} T + \frac{1}{2} N \rho_0 \int \mathrm{d}\mathbf{r} \phi(r) g(\mathbf{r})
\end{aligned}
\tag{1.3}
$$

Where we have defined the pair distribution function $g(\mathbf{r})$ as

$$
\rho_0 g(\mathbf{r}) \equiv (1/N) \sum_{\mathrm{i} \neq \mathrm{j}} \langle \delta(\mathbf{r} - \mathbf{r}_{\mathrm{ij}}) \rangle \tag{1.4}
$$

The Kronecker delta $\delta(\mathbf{r} - \mathbf{r}_{\mathrm{ij}})$ is zero everywhere except at the position $\mathbf{r} = \mathbf{r}_{\mathrm{ij}}$ which is independent of the choice of origin. And so $g(\mathbf{r})$ gives the probability to find at a given instant, two atoms separated by $\mathbf{r}_{\mathrm{ij}}$. Since the system is isotropic, $g(\mathbf{r})$ depends only on $|\mathbf{r}| = r$.

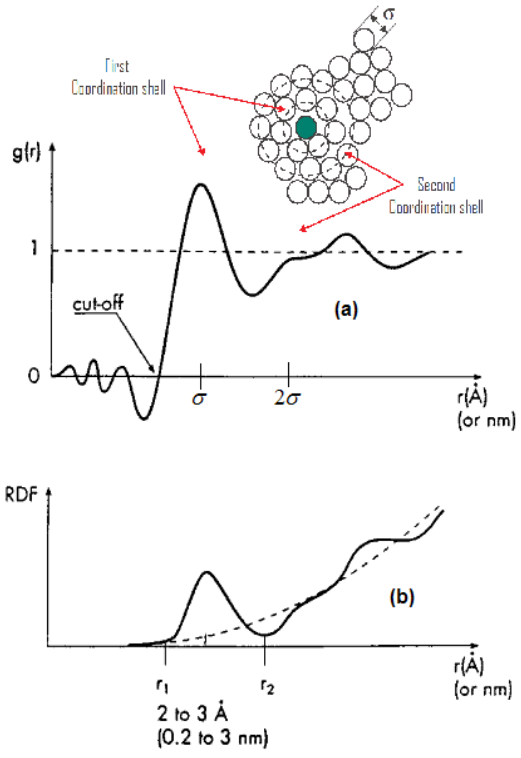

Figure 1.3 Real space functions for a monoatomic liquid : (a) pair-distribution function $g(r)$ and (b) radial distribution function RDF(r) [5].

Fig. 1.3(a) shows the typical features in a pair-distribution function for a monoatomic liquid. The oscillations below the cut-off threshold correspond to FT artifacts. Ideally, $g(\mathbf{r})$ goes to

very small values below the cutoff, because the very strong atomic repulsion makes it very unlikely to find two atoms separated by such small distances.

The first sharp peak corresponds to the radius of the first coordination shell. With increasing distance from the origin, the correlation between atoms becomes weaker and $g(\mathbf{r})$ approaches unity. This means that we're not probing a specific volume $\mathrm{d}v$ anymore and the local density number tends to its average value ρ_0. The system behaves like a structureless continuum.

We can define as well the Radial Distribution Function RDF(r) as follows:

$$\mathrm{RDF}(r) = 4\pi r^2 \rho_0 g(r) \tag{1.5}$$

which can be integrated to obtain the average number of neighbouring atoms in a coordination shell, or what we call the Coordination Number CN,

$$\mathrm{CN} = \int_{r_1}^{r_2} \mathrm{RDF}(r)\mathrm{d}r = 4\pi\rho_0 \int_{r_1}^{r_2} g(r) r^2 \mathrm{d}r \tag{1.6}$$

In practice, the coordination number is obtained by fitting Gaussian functions to the peaks delimited by two minima in the RDF.

The static structure factor is actually the measured quantity during a neutron or X-ray diffraction experiment and is the FT of $g(r)$,

$$\begin{aligned} S(\mathbf{Q}) &\equiv 1 + \rho_0 \int \mathrm{d}\mathbf{r}[g(\mathbf{r}) - 1]\exp(i\mathbf{Q}.\mathbf{r}) \\ S(Q) &= 1 + 4\pi\rho_0 \int_0^{\infty} \mathrm{d}r\, r^2 [g(r) - 1]\frac{\sin(Qr)}{Qr} \end{aligned} \tag{1.7}$$

The low Q values, typically between [0 – 0.3] Å^{-1}, correspond to the density fluctuations within the liquid. It describes the structure at a mesoscopic level. The Medium Range Order is in the range of [0.02 – 3] Å^{-1}. It gives information about heterogeneities and aggregations in the system. Whereas in the Q range of [0.2 – 30] Å^{-1}, lies the local order of interatomic and intermolecular structure.

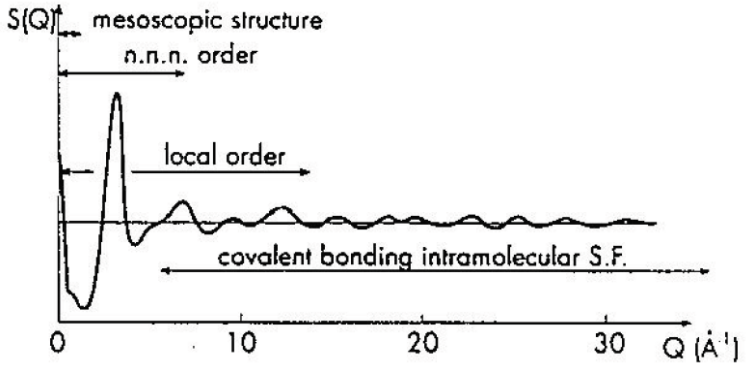

Figure 1.4 Illustrative $S(Q)$ plot showing the correspondence between the Q-range and the structural aspects [57].

Likewise via FT, we obtain the pair-distribution function $g(r)$ from $S(Q)$ as follows:

$$g(r)-1=\frac{1}{2\pi^2 r\rho_0}\int_0^\infty [S(Q)-1]Q\sin(Qr)\mathrm{d}Q \tag{1.8}$$

The formalism above is derived within the context of the static approximation which is why we have not indicated any time dependence for the $\mathbf{r}_{ij}$. This means that we make the assumption that the neutrons or X-rays are fast enough so that the time needed to cross from an atom to another is much smaller than the characteristic relaxation time of the system. It is as if we were taking "snapshots" of the local structure we're probing, and the resulting diffraction pattern represents an ensemble average of such local quasi-instantaneous structures, throughout the sample.

Polyatomic case:

For a polyatomic system, each atomic species has its own scattering length, and thus the scattering intensity in *S(Q)* is a contribution of all the correlations between the different atoms.
If we consider a system composed of n different types (i.e. different chemical species Z) of atoms, the resulting number of atomic pairs $\alpha\beta$ is $n(n+1)/2$. We can then define the partial static structure factor $S_{\alpha\beta}(Q)$ and the partial pair-distribution function $g_{\alpha\beta}(r)$ of each pair as follows:

$$S_{\alpha\beta}(Q)-1=\frac{4\pi\rho_0}{Q}\int_0^\infty r[g_{\alpha\beta}(r)-1]\sin(Qr)\mathrm{d}r \tag{1.9}$$

$$g_{\alpha\beta}(r)-1=\frac{1}{2\pi^2 r\rho_0}\int_0^\infty Q[S_{\alpha\beta}(Q)-1]\sin(Qr)\mathrm{d}Q \tag{1.10}$$

In this case, a peak in $S(Q)$ is a weighted sum of all the different pair contributions. $g_{\alpha\beta}(r)$ gives then the probability of finding an atom β at a distance r from an atom α taken as the origin.
Following the same reasoning, the partial Radial Distribution Function $\mathrm{RDF}_{\alpha\beta}$ can be written as,

$$\mathrm{RDF}_{\alpha\beta}(r) = 4\pi\rho_0 r^2 g_{\alpha\beta}(r) \tag{1.11}$$

And the partial coordination number,

$$\mathrm{CN}^{\alpha-\beta} = 4\pi\rho_0 c_\beta \int_{r_1}^{r_2} r^2 g_{\alpha\beta}(r)\mathrm{d}r \tag{1.12}$$

$\mathrm{CN}^{\alpha-\beta}$ now gives the average number of atoms β within two radii r_1 and r_2 around an atom α. We should note that, $S_{\alpha\beta}(Q) = S_{\beta\alpha}(Q)$ and $g_{\alpha\beta}(r) = g_{\beta\alpha}(r)$, and clearly $c_\alpha \mathrm{CN}^{\alpha-\beta} = c_\beta \mathrm{CN}^{\beta-\alpha}$.

1.3 Dynamics of glass-forming liquids.

1.3.1 Time-dependent correlation functions

In order to probe the dynamics of liquids, we have to involve the time as well in our correlation functions. One of the important correlations is the van Hove time-dependent pair-distribution function. It is a generalisation of $g(r)$ but without making the static approximation. The van Hove distribution function $G(r,t)$ will include the position (r) and the momentum (p) of the particles while involving the time (t) as well. It could be expressed as follows:

$$G(\mathbf{r},t) = (1/N)\sum_{i=1}^{\mathrm{N}}\sum_{\mathrm{j}=1}^{\mathrm{N}}\left\langle \delta[\mathbf{r} + \mathbf{r}_\mathrm{i}(0) - \mathbf{r}_\mathrm{j}(t)]\right\rangle \tag{1.13}$$

If we define the particle density operator,

$$\rho(\mathbf{r},t) = \sum_\mathrm{i} \delta(\mathbf{r} - \mathbf{r}_\mathrm{i}(t)) \tag{1.14}$$

The time-dependent pair-distribution function can be re-written as follow:

$$G(\mathbf{r},t) = (1/N)\int \left\langle \rho(\mathbf{r}' - \mathbf{r},0)\rho(\mathbf{r}',t)\right\rangle \mathrm{d}\mathbf{r}' \tag{1.15}$$

Physically, $G(r,t)$ gives the probability of finding an atom at r' at time t if there was an atom at r at time 0.

The quantity $G(r,t)$ could be separated into two contributions: the distinct part corresponding to two different atoms and the self part corresponding to an atom's correlation with itself.

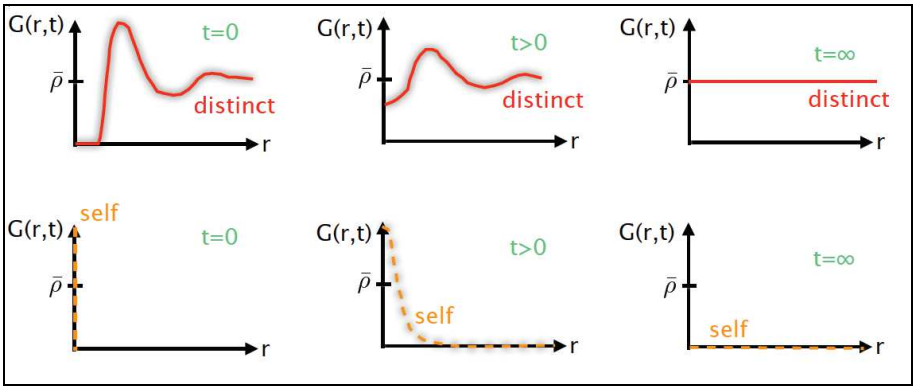

Figure 1.5 Illustrative plot to show the corresponding behavior of the distinct and self $G(r,t)$ with time [58].

Fig. 1.5 shows a qualitative behaviour of both, the distinct and the self contribution in the $G(r,t)$ for different times. If we look at the asymptotic behaviour of $G(r,t)$ for the distinct part, we can find that,

$$G^{\infty}(\mathbf{r}) = \lim_{t\to\infty} G(\mathbf{r},t) = (1/N)\int \rho_0(\mathbf{r}'-\mathbf{r})\rho_0(\mathbf{r}')d\mathbf{r}' = \rho_0 \tag{1.16}$$

This means that at long times, the two atoms are statistically independent, i.e. uncorrelated.

1.3.2 Relaxation time and viscosity

However, what is most relevant in studying glass-forming liquids is the intermediate scattering function $I(Q,t)$ or $S(Q,t)$ after accounting for the instrument resolution function. The $S(Q,t)$ function

$$S(\mathbf{Q},t) = (1/N)\sum_{i=1}^{N}\sum_{j=1}^{N}\left\langle \exp\{i\mathbf{Q}.[\mathbf{r}_i(0)-\mathbf{r}_j(t)]\}\right\rangle \tag{1.17}$$

is a central concept in our work and is related to $G(r,t)$ by space Fourier Transform. $S(Q,t)$ describes the decay in time of the density fluctuations within the liquid at fixed wave vector Q. $S(Q,t)$ can be obtained experimentally, and by fitting the data we obtain the characteristic

relaxation times of the system. In general we measure the dynamical structure factor $S(Q,\omega)$ and then obtain $S(Q,t)$ by time Fourier Transform.

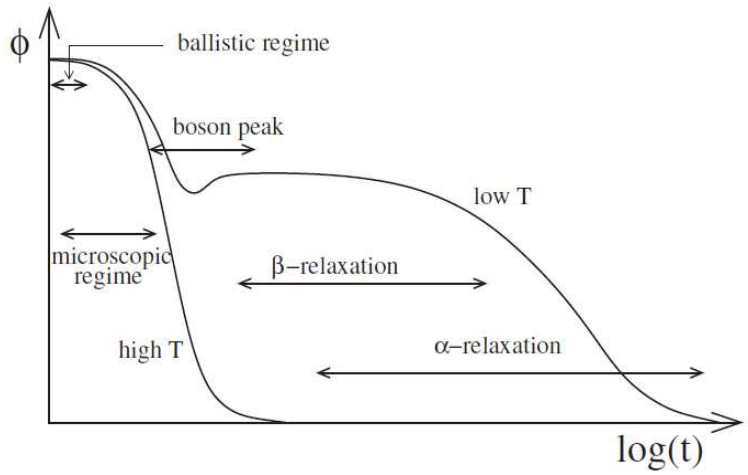

Figure 1.6 Sketch a typical relaxation behaviour of supercooled liquids [59].

Fig. 1.6 shows the typical behaviour of the intermediate scattering function in glass-forming liquids. We can see the difference in how quickly the system is relaxed in time as a function of temperature.

At high temperatures (left hand side curve), the system is relaxed in a short-time regime via what we call the Newtonian dynamics. This means that the particles move easily without any blockage effect coming from interactions with their environment. Such a regime is generally described by a simple exponential relaxation,

$$S(Q,t) = A\exp(-t/\tau) \tag{1.18}$$

and reflect a single dynamical regime occurring in the liquid, for instance the shear relaxation time. However, by lowering the temperature, we can see that the relaxation time increases and the decay is no longer purely exponential. After the first decay corresponding to the phonons at the smallest times, a two-step relaxation is observed.

The first step is the β-relaxation, described by a "plateau" varying little with time. This is generally a fast process reflecting the cage-effect where individual particles are rattling inside a cage formed by the surrounding atoms. Whereas the second and the slowest relaxation is called the α-relaxation, a collective process involving many atoms that is highly dependent on temperature and is conventionally called structural relaxation. Throughout this work, we discuss only this kind of relaxation process and is denoted by τ.

In General, glass-forming liquids exhibit a nonexponential relaxation [6,7] which is reasonably well fitted by a Kohlraush-Williams-Watt (KWW) stretched exponential form [8,9],

$$S(Q,t) = A\exp[(-t/\tau)^{\beta}] \tag{1.19}$$

where A is the amplitude, τ is the relaxation time and $\beta < 1$ is a stretching parameter. The KWW can easily be interpreted as arising from the superposition of different simple exponential relaxations weighted by a broad distribution of relaxation times (i.e. heterogeneous scenario, where it is expected that $\tau \sim Q^{-2}$, or by the sum of identical but intrinsically non exponential relaxations (i.e. homogeneous scenario, where it is expected that $\tau^{\beta} \sim Q^{-2}$.

According to Maxwell [10], liquids have a nonzero elastic response to shear for short enough times. This means that for times shorter than the structural relaxation time, liquids would behave mechanically like solids. And so the macroscopic shear viscosity η is directly related to its characteristic time τ,

$$\eta = G_{\infty}\tau \tag{1.20}$$

Where G_{∞} is the solid-like shear modulus at infinite frequency (i.e. infinitesimal time) and $\log(G_{\infty}) = 10$ [11]. However, it should be mentioned that the thermal dependence of G_{∞} is not yet precisely known, and its value for the liquid state differs slightly form that for solid. For simplicity reasons, we assume that G_{∞} is the same for both solid and liquid.

1.3.3 Fragility

According to their viscosity dependence upon temperature, glass-forming liquids can be classified into a fragile-to-strong scale. This was first introduced by Angell [12], where the log of the viscosity (hence the structural relaxation time), is plotted against the inverted temperature normalized to T_g. A typical Angell representation [$\log(\eta)$ vs. T_g/T] for different glass-forming liquids is shown in Fig. 1.7. By definition, at T_g/T=1, the viscosity $\eta \approx 10^{13}$ Poise whereas a value of $\eta \approx 10^{-4}$ poise corresponds to an "infinite" temperature limit for the material. We can clearly observe the different behavior of each system while approaching the glass transition. If we look at the network glass-forming liquids, like SiO_2 for instance, we see that its $\log(\eta)$ dependence upon temperature is nearly linear. It can therefore be described by an Arrhenius law,

$$\eta(T) = \eta_0 \exp\left(\frac{E}{T}\right) \tag{1.21}$$

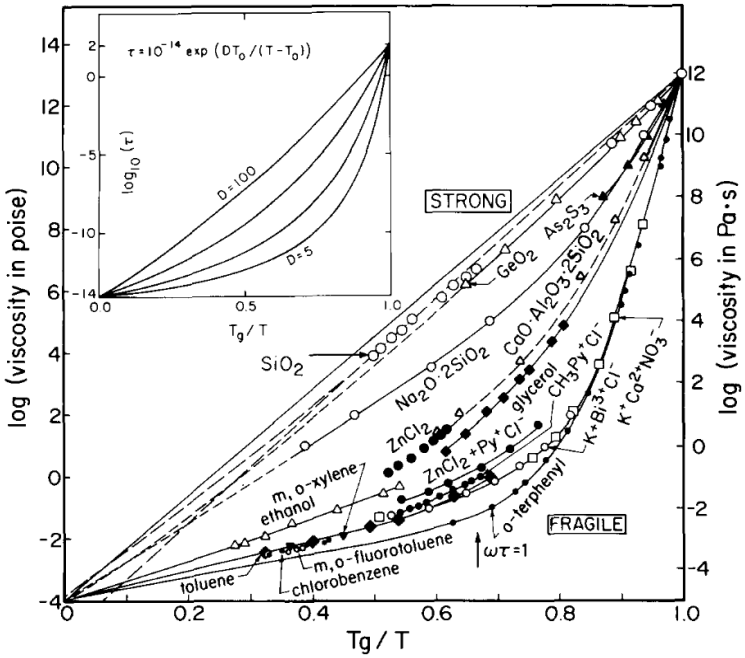

Figure 1.7 Angell plot of viscosity for different glass-forming liquids [12].

Where T is the temperature, $\eta_0 = 10^{-4}$ poise is the high temperature limit of the viscosity and E is the activation energy. Such systems are called "Strong" glass-formers and give a straight line on an Angell plot.

However, other systems are far from following an Arrhenius behavior and are called "Fragile" liquids, meaning they are poor glass-formers, due to a low viscosity near the melting point T_m. An important observation to highlight is that at $T_g/T \approx 0.8$, "Fragile" liquids have an increase in viscosity that differs from a system to another. The best fit to describe such behavior is a modified form of the well know Vogel-Fulcher-Tamman (VFT) law [13-15],

$$\eta = \eta_0 \exp\left[\frac{DT_0}{T - T_0}\right] \tag{1.22}$$

Where T_0 is a constant and the single parameter D describes the extent to which the liquid follows the Arrhenius behaviour. It is well known that a large value of D, on the order of 100, implies a strong liquid whereas a small value of D (less than 10) indicates a very fragile or non Arrhenius liquid (insert of Fig. 1.7). In general, strong glass formers tend to have strong (i.e. covalent) bonds between atoms, whereas fragile glass formers tend to exhibit weaker (i.e. Van der Waals) bonds.

Another quantitative way to classify their degree of fragility is to measure the slope of log(η) vs. T_g/T, in other words, measuring how steep does the viscosity approach $\eta(T_g) = 10^{12}$ Pa.s with decreasing temperature. The steeper, hence larger m, means more fragile. The steepness or fragility index "m" could be written as,

$$m = \lim_{T \to T_g} \frac{d(\log \eta)}{d(T_g / T)} \tag{1.23}$$

Fragility index ranges from $m \sim 17$ for strong liquids to $m \sim 150$ for fragile liquids.

An interesting feature of the fragility classification is that it tries to link the macroscopic properties like viscosity to the microscopic dynamics of the system.

The kinematic fragility described above has been found to be correlated as well to other properties of the glass-forming liquid such as the temperature dependence of the configurational entropy, referred to as thermodynamic fragility [16]. For the most fragile materials, the heat capacity of the liquid near T_g is about twice that of its glass, implying that the structure of the liquid changes rapidly with temperature and hence is "fragile". In such systems, the high cooperativity of the diffusive dynamics induces a high apparent activation energy. And so the statistics of the minima in the potential energy landscape description [17, 18] of the diffusion process in supercooled liquids [19-21] is related as well to both the kinetic and the thermodynamic fragility.

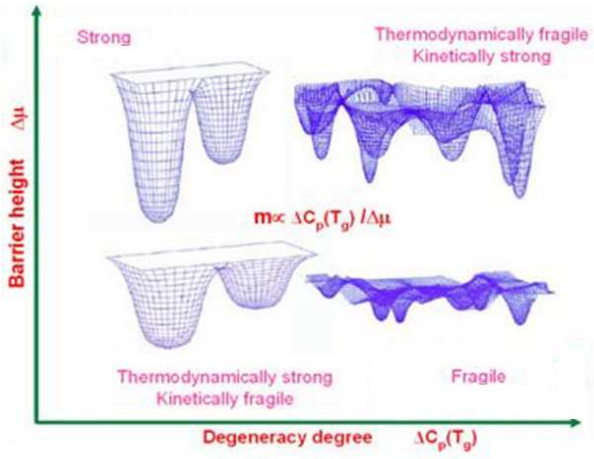

Figure 1.8 Characterization of the kinematic and thermodynamic fragility [60].

$$m = \lim_{T \to T_g} \underbrace{\frac{d(\log\eta)}{d(T_g/T)}}_{\text{barrier height}}^{\text{kinematic}} \vee \underbrace{\frac{\Delta C_p(T_g)}{\Delta\mu}}_{\substack{\text{minima density} \\ \text{(degeneracy)}}}^{\text{thermodynamic}} \tag{1.24}$$

From Fig. 1.8, we can see that the (3N+1)-dimensional potential energy hypersurface in the configurational space for fragile liquids is characterized by high configurational degeneracy $\Delta C_p(T_g)$ and by small barrier heights $\Delta\mu$. New physical insight has been offered by recent experimental [22-27], simulation [28-32] and theoretical [33], but the quest for a unified and quantitative description of fragility remains open.

1.3.4 Diffusion coefficient

One of the key parameters in viscous fluids is the diffusion coefficient, denoted by D. It affects a lot of properties in glass-forming liquids like relaxation times and electric conductivity. It could be defined as the migration of a single or flux of atoms towards a certain specific direction within the fluid to reduce the concentration gradient. Mathematically, this could be expressed as,

$$D\nabla^2 G_s(\mathbf{r},t) = \frac{\partial}{\partial t} G_s(\mathbf{r},t) \tag{1.25}$$

This equation is known as Fick's law where D is generally expressed in [$m^2.s^{-1}$]. The diffusion coefficient can be linked to the viscosity through the Stokes-Einstein relation [34],

$$D = \frac{k_B T}{6\pi r \eta} \tag{1.26}$$

Where k_B is the Boltzmann constant (1.38×10^{-23} $J.K^{-1}$), T is the temperature in K, r is the radius of the diffusing particle and η the viscosity in Pa.s. The Stokes-Einstein model assumes that the system is of low viscosity and that the diffusing particle is spherical and much larger than the surrounding particles within the liquid. This would apply reasonably well to high temperature liquid CAS close and above the melting temperature where it is assumed to have a lot of breaking bonds far from any polymerisation. Experimentally, the diffusion coefficient can be extracted directly from the self intermediate scattering function [35],

$$\begin{aligned} S_{self}(\mathbf{Q},t) &= \int G_s(\mathbf{r},t)\exp(-i\mathbf{Q}.\mathbf{r})\mathrm{d}\mathbf{r} \\ &= \exp(-DQ^2 t) \end{aligned} \tag{1.27}$$

$S_{self}(\mathbf{Q},t)$ involves the diffusion of a single atom (self-diffusion), however in a polyatomic system like CAS melts the total measured $S(\mathbf{Q},t)$ can be dominated, at least at low Q, by the distinct contribution making it difficult to extract diffusive coefficients for a given atomic species.

1.4 Calcium AluminoSilicates

Liquid Calcium Alumino-Silicates (CAS) belong to a class of refractory oxides that are of both geophysical and technological importance. They constitute a large fraction of the composition of natural magmas within the interior of the earth and terrestrial planets [36]. Their glass phases are attractive materials for a wide range of technical applications as well due to their highly refractory nature, their excellent optical and mechanical properties [37-39].

This ternary system ($CaO - Al_2O_3 - SiO_2$) is remarkable since glasses with very small SiO_2 content can be synthesized, contrary to alkali or Mg alumino-silicate glasses. In the following section, we are going to describe briefly silicate systems in order to better understand their characteristics.

1.4.1 Generalities

To be a good glass former, a material must have trouble nucleating seed crystals and must prevent those seed crystals from growing quickly. Because silica (amorphous SiO_2) is extraordinarily viscous at its melting temperature T_m, it's known to be an excellent glass former.

Silica is held together by covalent bonds which are highly directional. Each silicon atom in the silica forms covalent bonds with four oxygen atoms and orients those atoms at roughly the corners of a tetrahedron (Fig. 1.9). The result is an intricate network of silicon and oxygen atoms in which each oxygen atom acts as a bridge between two adjacent silicon atoms. These oxygen atoms are called Bridging Oxygen (BO) [40]. Therefore, because of its interlinking structure, silicon dioxide is often called a network former. When additional chemical species (like for instance the calcium cations in the CAS) are added, they are often regarded as network modifiers which compete with the network forming ions for anions (oxygen), affecting the network structure e.g give rise to a Non-Bridging Oxygen (NBO) that doesn't form a bridge between a pair of silicon atoms. There are also some chemical compounds that are known as intermediates. They can act as either glass formers or modifiers depending on the stoechiometric composition of the glass. The most important intermediate compounds are aluminum oxide or alumina Al_2O_3 (crystal form = sapphire).

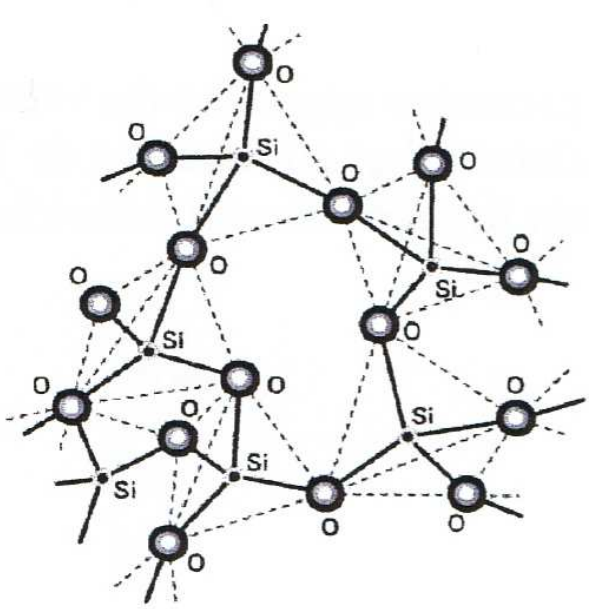

Figure 1.9 3D representation of a glassy silicate [41].

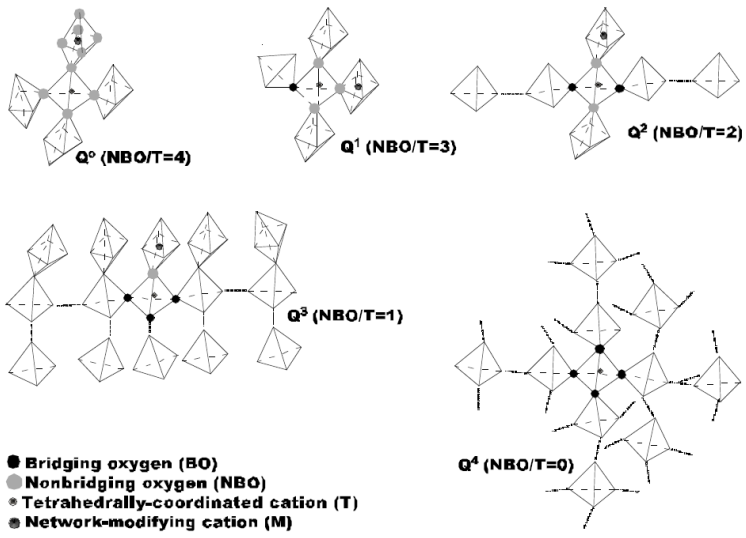

Figure 1.10 Schematic representation of the different types of silicate tetrahedra [42].

Often connectivity of tetrahedral glass networks is described in terms of fractions of Q^n-species where n = [0…4] describes the number of connected vertices (Fig. 1.10). For example a fully connected network consists of 100% Q^4 species, whereas a more complex system might contain 75% Q^3 (tetrahedra with one free, non-bridging vertex) 25% Q^2 (two, non-bridging vertices).

1.4.2 Scientific interest

By conventional cooling, calcium aluminate binary compounds $(CaO)_x - (Al_2O_3)_{1-x}$ can be vitrified to colourless transparent glasses in a narrow range of composition centered at $x = 0.65$ [43,44]. By using a containerless technique, it is possible to avoid heterogeneous nucleation and extend the vitreous domain to $x = 0.37 - 0.75$ [45,46] that includes the $x = 0.5$ ($CaAl_2O_4$) composition first studied in this work and termed "CA".

The introduction of small amount of the "canonical" strong glass-former SiO_2 allows a broadening of the glass forming ability over a larger calcium concentration range and a lowering of the liquidus temperature [47]. Usually, the glass transition temperature of a mixture can be expressed by a Gordon-Taylor type equation:

$$T_g = \frac{w_a T_a + k w_b T_b}{w_a + k w_b} \tag{1.28}$$

where T_g is the glass transition temperature of the mixture, $w_a(T_a)$ and $w_b(T_b)$ are the weight fractions (glass transition temperatures) of components a and b and k is a constant. However, the introduction of silica strongly affects the macroscopic properties and thus the structure and dynamics of these glasses. For instance, the glass transition temperatures, see Fig. 1.11 (left), obtained from Differential Scanning Calorimetry (DSC) measurements as a function of SiO_2 content for three joins SiO_2-R, with R=CaO/Al_2O_3 taken between 1 and 3 show that, contrary to the R=1 case, a striking behaviour is observed for the two joins R=1.57 and 3. In fact the T_g values present a maximum at 10 and 20 mol% of silica respectively. These augmentations are more important for the join R=3 than for the join R=1.57. Several models have been proposed to explain this behavior which results from an increase of the polymerization network but no comprehensive view has yet emerged [48].

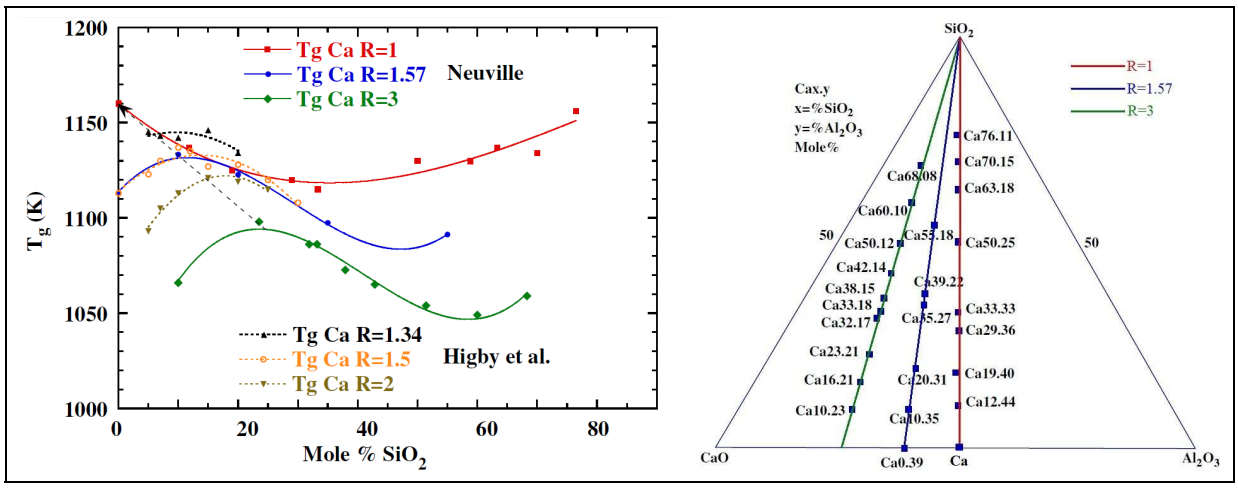

Figure 1.11 Glass compositions and glass transition temperatures for Calcium AluminoSilicate glasses [49].

According to the Angell's classification [56] scheme of glass forming liquids, the $(CaO)_x - (Al_2O_3)_{1-x}$ systems are extremely fragile, from both the kinematic and the thermodynamic point of view, showing both large departure from Arrhenius law and large heat capacity variation $\Delta C_p(T_g)$. To furnish an idea about their kinematic fragility, it should be noted that they have viscosities of less than 1 Poise at $T_g / T = 0.5$ e.g. for the CA (composition x=0.5), compared to for example, the value of 10^4 Poise for the "long glass" SiO_2.

It should be noticed that due to the difficulty of vitrifying Calcium Aluminate glasses with conventional methods, only few studies exist for the CA composition. The melting and glass transition temperatures of CA are around 1878 K and 1178 K respectively. In the liquid state some structural studies have been performed using NMR [50], neutron and x-ray scattering [51-53]. The x-ray and neutron structure factors $S^X(Q)$ and $S^N(Q)$ for the liquid CA at 2173 K displayed a first peak at $Q = 2.15 \pm 0.02$ Å^{-1} which is seen to be more pronounced in $S^X(Q)$ than in $S^N(Q)$. At high temperatures ($T > 1500$K), this first peak was observed to be almost at the same position [54]. The weights of the partial structure factors for x-rays (at $Q = 2.15 \pm 0.02$ Å^{-1}) and neutrons as calculated from molecular dynamics simulations attributed this first peak principally to cation-cation correlations [55].

In order to study the evolution of the structure during the cooling process, Hennet et al. [54] performed a time resolved x-ray measurement at intervals of 100 ms while cooling the CA rapidly (i.e. quench) from its stable liquid phase well above the melting point to the cold glass below T_g. The evolution of the first peak of $S(Q)$ is shown in Fig. 1.12.

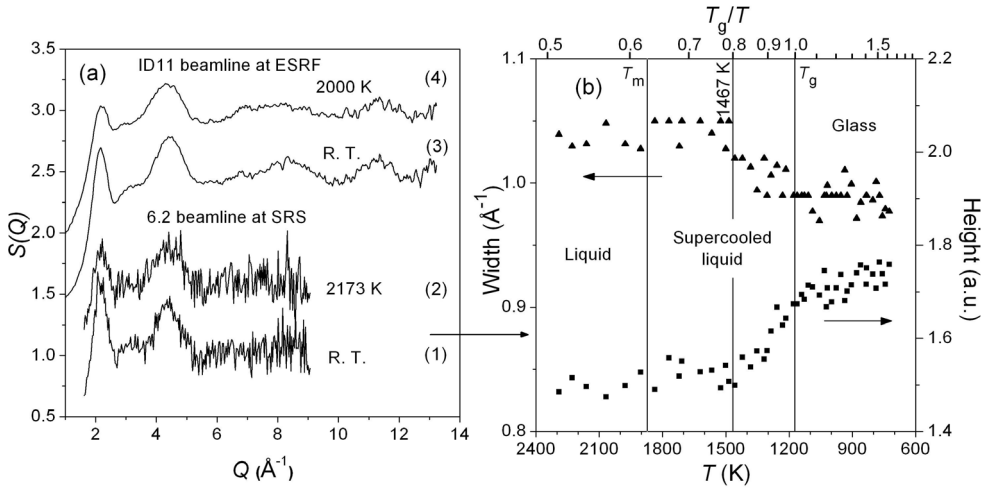

Figure 1.12 (a). Average structure factor of $CaAl_2O_4$ measured for 100 ms at room temperature (b) Dynamical evolution of the width and intensity of the first peak of $S(Q)$ during the cooling of the sample from 2173 K to room temperature [54].

Although the FSDP doesn't show any significant changes in position, we observe (i) a sharpening and (ii) an increase of its intensity at a temperature near $1.2T_g$. The corresponding real space obtained by FT shows also a shortening of the Al-O distance at the same temperature [54]. These two features indicate an increase in the degree of both intermediate-range order (IRO) and short-range order (SRO) occurring close to the dynamical crossover temperature that characterizes "fragile" liquids. Angell pointed out that this significant evolution of IRO as a characteristic feature of fragile liquids [56]. In the energy landscape picture, the deeper minima assumed by the CA melt must correspond to an increase in structural order on both short and intermediate length scales. However, as only the x-ray weighted average structure factor *S(Q)* is measured, there is no firmly established explanation about the microscopic origin of the evolution of SRO and MRO as a function of temperature.

1.4.3 Studied compositions

In this work we studied the structure and dynamics of several CAS glasses and melts along the join R=1 (R= CaO/ Al_2O_3) in the ternary phase diagram CaO-Al_2O_3-SiO_2 as shown in Fig. 1.11, which gives compounds in the binary system $(CaAl_2O_4)_{1-x} - (SiO_2)_x$. The compositions studied are summarized in Table. 1.

In order to study the liquid state, we used the aerodynamic levitation technique associated with a CO_2 laser heating. In particular this technique had not yet been applied for doing QENS experiments. Therefore the work presented in the following required first the design and development of specific levitation systems that will be presented in the next chapter.

Sample	SiO_2 (mol%)	Al_2O_3 (mol%)	CaO (mol%)	R=CaO/ Al_2O_3
CA	0	50	50	1
CAS 12.44	11.82	44.10	44.10	1
CAS 19.40	18.99	40.51	40.51	1
CAS 33.33	33.33	33.33	33.33	1
CAS 50.25	50	25	25	1

Table 1. Different CAS compositions studied in this work for which ND, QENS and IXS results are presented.

REFERENCES

[1] P. G. Debenedetti and F. H. Stillinger, Nature. 410-259 (2001).

[2] W. B. Hillig and D. Turnbull, J. Chem. Phys. 24, 914-914 (1956).

[3] J. P. Hansen and I. R. McDonald; Theory of simple liquids, Academic Press London (2006).

[4] Balucani and Zoppi; Dynamics of the liquid state, Clarendon Press (1995).

[5] H. E. Fischer, A. C. Barnes, and P. S. Salmon, Rep. Prog. Phys. 69, 233-299 (2006).

[6] A. Cavagna, Phys. Rep. 476, 51-124 (2009).

[7] A. Meyer, H. Schober, and D. B. Dingwell, Europhys. Lett. 59, 708 (2002).

[8] R. Kohlrausch, Ann. Phys. (Leipzig) 167, 179-214 (1854).

[9] G. Williams and D. C. Watts, Trans. Faraday Soc. 66, 80-85 (1970).

[10] J. C. Maxwell, Philos. Trans. R. Soc. London 157, 49-88 (1867).

[11] A. Angell, Pb. Elsevier, Oxford, 1-11 (2004).

[12] C. A. Angell, J. Phys. Chem. Solids 49, 863 (1988).

[13] H. Vogel, Phys. Z. 22, 645 (1921).

[14] G.S. Fulcher, J. Amer. Ceram. Soc. 8, 339 (1925).

[15] G. Tamman and W.Z. Hesse, Anorg. Allg. Chem. 156, 245 (1926).

[16] L.-M. Martinez, C. A. Angell. Nature 410, 663 (2001).

[17] M. Goldstein, J. Chem. Phys. 51, 3728 (1969).

[18] W. H. Stillinger, T. A. Weber, Phys. Rev. A 25, 978 (1982).

[19] R. Hall, P. Wolynes, J. Chem. Phys. 86, 2943 (1987).

[20] R. J. Speedy, J. Phys. Chem. B 103, 4060 (1999).

[21] S. Sastry, Nature 409, 164 (2001).

[22] K. Ito, C. T. Moynihan, and C. A. Angell, Nature (London) 398, 492 (1999).

[23] K. L. Ngai, J. Non-Cryst. Solids 275, 7 (2000).

[24] T. Scopigno, G. Ruocco, F. Sette, and G. Monaco, Science 302, 849 (2003).

[25] V. N. Novikov, Y. Ding, and A. P. Sokolov, Phys. Rev. E 71, 061501 (2005).

[26] H. Tanaka, J. Non-Cryst. Solids 351, 678 (2005).

[27] K. Niss, C. Dalle-Ferrer, G. Tarjus, and C. Alba-Simionesco, J. Phys.: Condens. Matter 19, 076102 (2007).

[28] C. De Michele, F. Sciortino, and A. Coniglio, J. Phys. Condens. Matter 16, L489 (2004).

[29] P. Bordat, F. Affouard, M. Descamps, and K. L. Ngai, Phys. Rev. Lett. 93, 105502 (2004).

[30] V. Molinero, S. Sastry, and C. A. Angell, Phys. Rev. Lett. 97, 075701 (2006).

[31] M. Sun, Y. Sun, A. Wang, C. Ma, J. Li, W. Cheng and F. Liu, J. Phys. Condens. Matter 18, 10889 (2006).

[32] D. Coslovich and G. Pastore, J. Chem. Phys. 127, 124504 (2007).

[33] G. Ruocco, F. Sciortino, F. Zamponi, C. De Michele, and T. Scopigno, J. Chem. Phys. 120, 10666 (2004).

[34] A. Einstein; Investigations on the Theory of Brownian Motion, Dover New York (1956).

[35] M. Bee; Quasielastic Neutron Scattering, Adam Hilger (1988).

[36] D. L. Anderson; New Theory of the Earth, Cambridge University Press p5 (2007).

[37] K. L. Scrivener, J-L. Cabiron and R. Letourneux, Cem. Concr. Res. 29 1215 (1999).

[38] H. F. W. Taylor; Cement Chemistry, Thomas Telford Publishing p295 (1997).

[39] L. L. Hench, J. Am. Ceram. Soc. 74 1487 (1867).

[40] B. O. Mysen, D. Virgo and F. A. Seifert, Amer. Min., 69, 834-848 (1984).

[41] DiNardo Christine, Etude et contrôle des réactions d'oxydoréduction au cours de l'élaboration des matrices vitreuses de confinement des déchets nucléaires, Thèse Université de Montpellier-CEA VALRHO (2003).

[42] B. O. Mysen and P. Richet; Silicate glasses and melts: Properties and structure. Elsevier, Amsterdam (2005).

[43] J. E. Shelby, C. M. Shaw and M. S. Spess, J. Appl. Phys. 66, 1149 (1989).

[44] Y-M. Sung and S-J. Kwon. J. Mater, Sci. Lett. 18 1267 (1999).

[45] M.-C. Badets, C. Bessada, P. Simon, A. Douy, D. Massiot, J.-C. Rifflet, F. Taulelle, and J. P. Coutures, Proceeding of the Seventh European Symposium on Materials and Fluid Sciences in Microgravity, Oxford, UK, ESA SP-295, pp. 511–517 (1990).

[46] L. Hennet, I. Pozdnyakova , A. Bytchkov , V. Cristiglio, D. Zanghi , S. Brassamin, J-F. Brun, M. Leydier and D. L. Price, J. Non-Cryst. Solids 354 5104 (2008).

[47] J. E. Shelby, J. Am. Ceram. Soc. 68 155 (1985).

[48] L. Cormier, D. R. Neuville and G. Calas, J. Am. Ceram. Soc. 88 2292–2299 (2005).

[49] D. R. Neuville, L. Cormier, A-M. Flank, V. Brios and D. Massiot, Chem. Geol. 213, 153–163 (2004).

[50] B. T. Poe, P. F. McMillan, B. Cote, D. Massiot and J. P. Coutures, Science 259 768 (1993).

[51] J. K. R. Weber, C. J. Benmore, J. A. Tangeman, J. Siewenie and K. J. Hiera, J. Neut. Res. 11 -113 (2003).

[52] V. Cristiglio, L. Hennet, G.J. Cuello, I. Pozdnyakova, M. Leydier, J. Kozaily, H. E. Fischer, M. R. Johnson and D. L. Price, J. Non-Cryst. Solids, 356 2492–2496 (2010).

[53] J. W. E. Drewitt, S. Jahn, V. Cristiglio, A. Bytchkov, M. Leydier, S. Brassamin, H. E. Fischer and L. Hennet, J. Phys. Cond. Mat. 23 155101 (2011).

[54] L. Hennet, I. Pozdnyakova, V. Cristiglio, G. J. Cuello, S. Jahn, S. Krishnan, M-L. Saboungi and D. L. Price, J. Phys. Condens. Matter 19 455210 (2007).

[55] V. Cristiglio, L. Hennet, G. J. Cuello, I. Pozdnyakova, M.R. Johnson, H. E. Fischer, D. Zanghi and D. L. Price, J. Non-Cryst. Solids 354 5337 (2008).

[56] C. A. Angell, J. Non-Cryst. Solids 73 1 (1985).

[57] P. Chieux J. Mol. Struct. 296 177 (1993).

[58] B. Frick. Hercules School, http://hercules-school.eu/.

[59] W. Kob. In Computer Simulations in Condensed Matter: From Materials to Chemical Biology. Volume 2 , Lecture Notes in Physics. Springer (2006).

[60] Salvatore Magazù, Studium Report, http://lestudium.cnrs-orleans.fr/francais/rubriques/actu/chercheurs/rapports/magazu.pdf.

Résumé du Chapitre 2

Ce chapitre est une description des méthodes de lévitation et des développements techniques réalisés dans cette thèse. En fait, malgré de nombreuses études réalisées au cours des 50 dernières années, l'état liquide n'est pas encore bien compris. Il est donc important de développer des techniques expérimentales permettant d'étudier les propriétés des liquides à haute température.

L'une des principales difficultés pour l'étude des matériaux en fusion est d'amener le matériau à haute température et cela dans de bonnes conditions expérimentales. Il est souvent difficile d'utiliser des fours traditionnels o*ù* le liquide est contenu dans un récipient. En effet, pour des températures supérieures à 1000°C, les expériences peuvent être confrontées à différents problèmes dont certains sont incontournables avec l'utilisation de fours traditionnels et qui deviennent critiques pour les très hautes températures:

- L'échantillon liquide peut réagir avec le support et ainsi être contaminé.
- Le support peut influencer les mesures expérimentales.
- Il est généralement difficile d'atteindre des températures supérieures à 1500°C avec des fours traditionnels.
- Il est difficile d'atteindre des états métastables comme la surfusion due à la nucléation hétérogène.

L'utilisation de techniques sans contact permet de contourner ces problèmes et d'accéder à de très hautes températures, de maintenir la pureté de l'échantillon, de contrôler sa composition chimique et de permettre un accès facile à l'état surfondu (l'échantillon pouvant rester liquide plusieurs centaines de degrés en dessous de la température de cristallisation).
Ce chapitre commence donc par un exposé sur les principales méthodes de lévitation qui sont utilisées dans le monde. La lévitation aérodynamique au cœur de ce travail est ensuite davantage détaillée en insistant sur la stabilité, la méthode de chauffage et la mesure de température de l'échantillon.

Une partie importante de ce travail de thèse à été le développement d'un dispositif de lévitation sur un spectromètre de diffusion inélastique de neutrons à l'ILL.
La faisabilité d'une telle combinaison de techniques avait déjà été démontrée pour les techniques de lévitation électromagnétique et électrostatique. Toutefois, ces deux techniques sont limitées à des échantillons conducteurs et aux échantillons qui peuvent être chargés électriquement ou qui présentent des transitions de phase lors du chauffage.
Le flux de neutrons relativement faible conduit à une diffusion inélastique du rayonnement très peu intense et proportionnelle au volume de l'échantillon. Ceci explique qu'à cause des petits

échantillons utilisés, la lévitation aérodynamique n'a pas été largement mise en œuvre avec les techniques de diffusion inélastique des neutrons.
Afin de pouvoir effectuer nos expériences sur la dynamique (QENS) présentées dans les chapitres suivants, il a fallut améliorer le dispositif. En particulier, nous avons dû modifier la configuration des buses de lévitation qui limitait la taille des échantillons pouvant être mis en lévitation (environ 2,7 mm de diamètre). Bien que cette taille d'échantillon soit acceptable pour les mesures de diffraction, elle n'est pas suffisante pour des expériences de diffusion inélastique des neutrons.

Dans la suite de ce chapitre, nous détaillons les principales étapes du développement et de l'optimisation du dispositif (optimisation de la buse, installation de masques, étude de l'effet du gaz…). En particulier, nous avons montré qu'il est possible d'augmenter le diamètre maximal de l'échantillon qui peut être lévité jusqu'à 4 mm. En réduisant au mieux le bruit de fond et en faisant usage d'un spectromètre à haut flux, nous avons ainsi réussi à effectuer pour la première des mesures de TOF-QENS sur des échantillons en lévitation aérodynamique.

Ce chapitre se termine par une description des derniers développements que l'on a apportés à la lévitation aérodynamique. Un système de lévitation avec des jets de gaz multiples qui devraient permettre de réaliser des expériences avec un échantillon de plus grand diamètre et qui ne sera pas caché partiellement par la buse de lévitation.

CHAPTER 2

2 CONTAINERLESS SAMPLE ENVIRONMENTS

Following a brief introduction, this chapter is divided into four sections. The first section gives an overview of the levitation techniques that have been used at synchrotron and neutron sources. The second part summarizes the different aerodynamic levitation setups used in the present work. The third part focuses on the new aerodynamic levitation setup that was designed for Quasi Elastic Neutron Scattering (QENS). Finally, some future developments that I developed are discussed.

2.1 Introduction – Objectives

While studies of liquids at high temperatures present an obvious interest from a fundamental point of view, they also present significant technological interest since the molten state is an essential stage in various industrial processes (glass making, semiconductor technologies, aerospace companies, iron and steel industry…). The high-temperature properties of oxide minerals or iron-based liquid alloys also play a crucial role in the geophysical behaviour of the earth.

Despite a considerable number of studies performed over the past 50 years, the liquid state is still not well understood. It is therefore important to develop experimental techniques as well as numerical simulation capabilities for studying the properties of high-temperature liquids.

Studies of liquid materials at high-temperature have to contend with various problems when they are carried out in a traditional furnace where the sample is held in a container:

- Chemical reactions between the sample and the container.
- Contamination of the sample from the container.
- Difficulty of reaching temperatures above 1500°C.
- Difficulty of undercooling the sample due to heterogeneous nucleation.

The use of containerless methods avoids these problems. Over the past few years an increasing number of studies devoted to high-temperature molten materials have been carried out as a result of the development of levitation techniques.
Several laboratories around the world have developed various kinds of levitation apparatus, including acoustic, electromagnetic, electrostatic and aerodynamic levitation techniques. They have been applied to determine physical properties of levitated liquids. A recent review can be found in ref [1]. Some of them have been combined with x-ray and neutron scattering techniques to study the structure and the dynamics of molten materials.

The CEMHTI in Orleans has chosen to combine aerodynamic levitation with a CO_2 laser heating [2-4]. The advantages of the technique are the simplicity and compactness of the device that allows its integration into different kinds of experiments. This technique makes it possible to access very high liquid temperatures while maintaining the sample's purity, and to investigate metastable states in the undercooled temperature range, down to a few hundred degrees below the equilibrium melting temperature.

2.2 Levitation Techniques

The principle of levitation is to create an opposing force to counteract the gravity of the sample and lift it away from support structures. In the past, four main levitation methods have been combined with x-ray and neutron scattering techniques at synchrotron and neutron sources: single-axis acoustic levitation (SAL), electromagnetic levitation (EML), electrostatic levitation (ESL) and conical nozzle levitation (CNL).

2.2.1 Acoustic levitation

Acoustic levitation can suspend small objects via the acoustic radiation force that results from an impedance difference between the suspension medium, normally a gas, and a solid or liquid sample. A single-axis acoustic levitator consists mainly of two parts: a vibrating source (or transducer) generating frequencies of a few tens of kHz (i.e. ultrasound) and a reflector with a concave surface to improve the efficiency. The vibrating source-reflector axis is parallel to the direction of gravity and an acoustic wave is generated along this direction to counteract gravity.
SAL can be used to study low melting point alloys and non-conducting materials as well as room temperature liquids. In the past, Trinth developed a device enabling to work up to 700°C [5]. Resistive heating coils were used to heat the sample. But even though, the accessible temperature range is limited and this technique is not for very high temperature studies.

2.2.2 Electromagnetic Levitation

Electromagnetic levitation is mainly suitable for electrically conductive materials. It will be discussed here only briefly since a detailed description of the EML can be found in the article of D. Holland-Moritz et al. [6] and [7,8].
With EML a radiofrequency electromagnetic field is generated by a levitation coil and Foucault currents are induced in the sample. This leads to an inductive heating of the sample, and at the same time, the interaction of the Foucault currents with the magnetic field of the coil leads to a force that counteracts gravity and makes it possible to levitate the sample. The electromagnetic force applied on the levitated sample depends on the power absorbed by the latter. It is essentially a function of the square of the magnetic field strength and the electrical conductivity of the sample material. So by varying the heating power, one can control the temperature of the sample. The levitation coil is situated in a vacuum chamber which is first evacuated and then filled with a very high purity gas, usually Helium (He) or a mixture He plus a few percent of Hydrogen (H_2).

Figure 2.1 shows a photograph of a typical electromagnetic levitation setup developed at the German Space Center (DLR) within the "Institut für Materialphysik im Weltraum" (Institut for Materials Physics in Space). It is used for neutron diffraction on the D20 instrument at the ILL [6].

2.2.3 Electrostatic Levitation

With ESL [9], the sample is electrically charged and levitated in a vertical electro-static field between two electrodes. Two pairs of smaller side electrodes are used to position the sample horizontally. When it levitates, the sample is melted using lasers. With this method, it is possible to study all samples that can be electrically charged. This method has various advantages. First, it works under vacuum, preventing contamination, and allows studying poor electrical conductors or materials with a low melting point. One drawback is the complexity of the setup that limits its combination with various spectroscopies. While some insulating oxides can be studied with this technique, it is used mostly with metals.

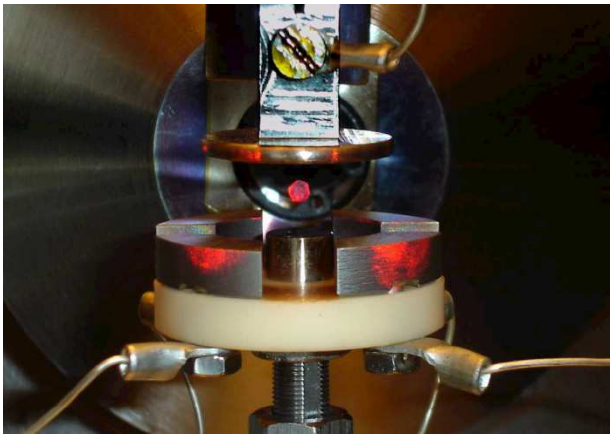

Figure 2.2 Levitated sample between the electrodes of an electrostatic levitator at DLR.

2.2.4 Aerodynamic Levitation

Aerodynamic levitation was first developed in the USA by D. A. Winborne and P. C. Nordine [10] then later adopted at the CEMHTI by J.-P. Coutures [11] for RMN studies. It has proved to be a powerful and versatile technique for studying highly reactive liquids in the equilibrium melt and the supercooled liquid state several hundred Kelvin below the melting point [12]. In particular, it is now widely used with neutron and x-ray diffraction techniques to investigate the structural properties of liquids [12–14]. The working principle of aerodynamic levitation is well known and is described in detail elsewhere [15]. Fig. 2.3 shows a standard aerodynamic levitation setup. The basic idea is to circulate levitation gas (usually argon) through a nozzle onto the sample from below in order to counteract gravity and lift it above the nozzle. The sample is then heated to the desired temperature by means of one or two focused CO_2 lasers. The levitation gas flow is accurately regulated and monitored by a mass flow controller enabling to maintain the sample sufficiently stable for long counting times.

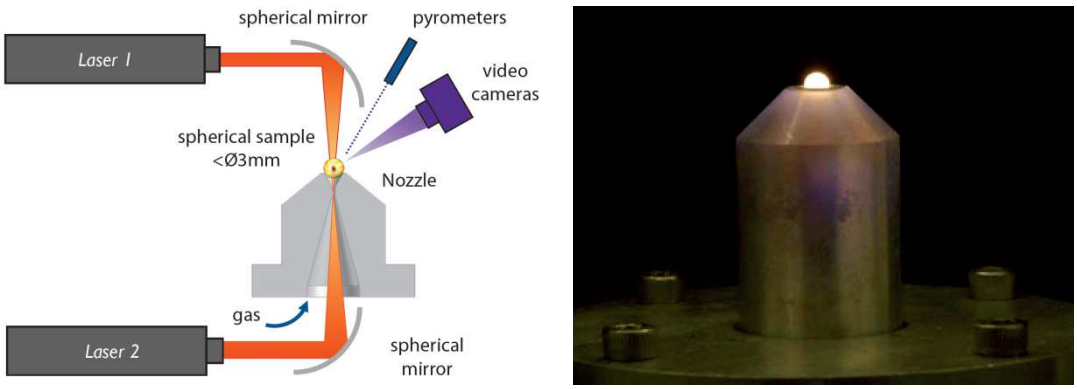

Figure 2.3 (left) schematic representation of the aerodynamic levitation working principle. (right) photograph of an illuminated levitated sample.

In comparison to the other levitation techniques (e.g. applying electromagnetic [16], electrostatic [9] or acoustic [17] fields), it has the outstanding advantage of supporting and melting any type of material ranging from insulators through semiconductors to metals. A current drawback is that samples need to be relatively small (~ Ø3 mm) in order to assure aerodynamic stability, but progress is now being made in this area.

Throughout all this work, we will be using only aerodynamic levitation. In the following section, we will give a general description of a basic experimental setup.

2.3 Experimental setups for aerodynamic levitation used in this work

Fig. 2.4 shows a 3D drawing of the basic components used in our aerodynamic levitation furnaces. A spherical sample with a diameter around 3 mm is situated on a levitator. The device is a convergent divergent nozzle enabling the diffusion of a gas jet below the sample (Fig. 2.5). Two continuous 125W CO_2 lasers operating at a wavelength of 10.6 μm are used for heating the sample from the top and a third one is used for heating the sample from below.

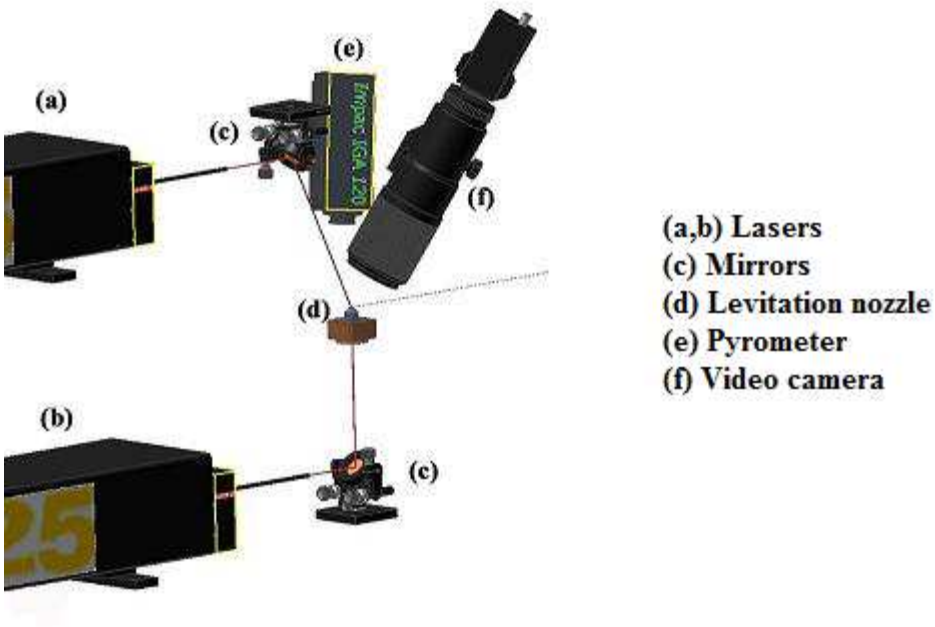

Figure 2.4 3D drawing of our aerodynamic levitation basic components.

The primary laser beams with a diameter of approximately 5 mm are focused on the sample using two spherical mirrors in order to obtain a final diameter of about 1 mm at the sample position. A third laser directed at the sample through the nozzle from below (Fig. 2.5) is used to compensate the cooling of the sample by the gas flow.

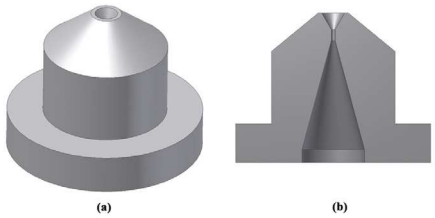

Figure 2.5 (a) Schematic view of an Aluminium nozzle used for x-ray diffraction. (b) Cutaway view highlighting the convergent-divergent geometry which allows a simple access of a laser beam onto the sample from below.

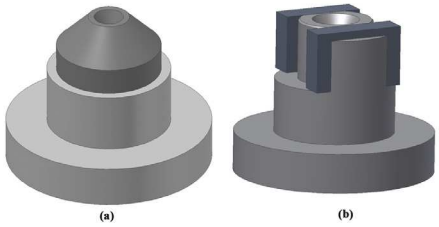

Figure 2.6 Schematic representation of the nozzle with a vanadium cover used for neutron diffraction experiments.

The nozzle support is cooled continuously with circulating water in order to prevent the nozzle from melting.

The temperature is measured by optical pyrometry. The choice of the pyrometer wavelength depends on the melting temperature of the sample material in question. For this reason, two different pyrometers are used to provide an accurate temperature measurement: a single wavelength pyrometer for the 75°C - 3000°C range and a two-wavelength one for only high temperatures going from 1000°C to 3000°C.
The levitation chamber is pumped down and then filled with the levitation gas. The gas can vary depending on the material being studied. Generally argon is used but sometimes a mixture of argon/oxygen is necessary to compensate for the loss of oxygen in the sample at very high temperatures.
Two video images of the sample taken from the top and from the side are continuously displayed in order to control the sample levitation during the heating process. Fig. 2.7 shows images of a levitated liquid yttrium aluminate at 2100°C. We can clearly see that one third of the sample is still hidden by the nozzle, and in general half of the sample is thus hidden.

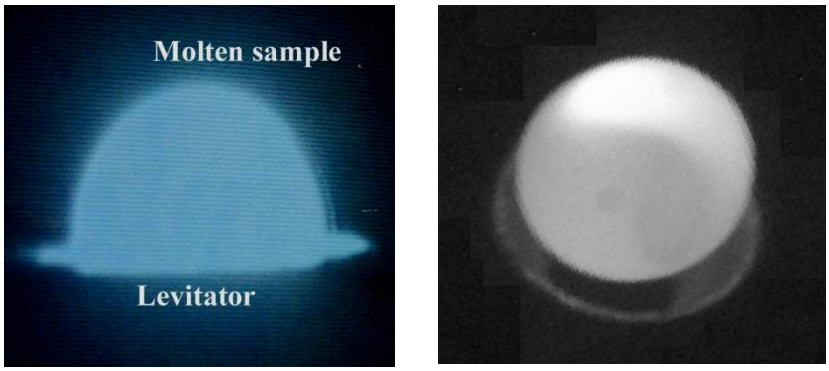

Figure 2.7 Images of a levitated liquid sample taken by the horizontale (left) and vertical (right) cameras.

Temperature measurement:

In such levitation experiments, temperature measurement is an important aspect. In fact, the quality of the results obtained is highly dependent on the temperature determination. For contactless measurement purposes, optical pyrometry is used. It is simple to use and convenient for such complicated setups in tight quarters. Nevertheless, in such a method, the emissivity of the sample should be known in order to distinguish the real temperature T of the sample from the apparent temperature Ta measured with the pyrometer as follows:

$$\frac{1}{T}-\frac{1}{T_a}=\frac{\lambda}{C_2}\ln\varepsilon_\lambda \qquad (2.1)$$

Where C_2 is the second radiation constant of Planck (C_2=1.4388 cm K) and ε_λ is the material emissivity at the working wavelength λ of the pyrometer. However, emissivity values for samples are often unknown and cannot be found in the public domain. In such a case, the measured temperature is calibrated according to the sample crystallization temperature expected from its phase diagram [18]. An example is illustrated in Fig. 2.8 that shows the temperature evolution with time upon cooling a levitated liquid alumina sample. The cooling process is performed by switching off the lasers and keeping the levitation gas flowing around the sample. The liquid alumina shows a crystallization peak near its melting temperature T_m = 2054°C. The pyrometer is then calibrated according to this value. The temperatures measured during experiments are often very stable with only minor periodic oscillations of ~ ± 30K due to the sample rotation.

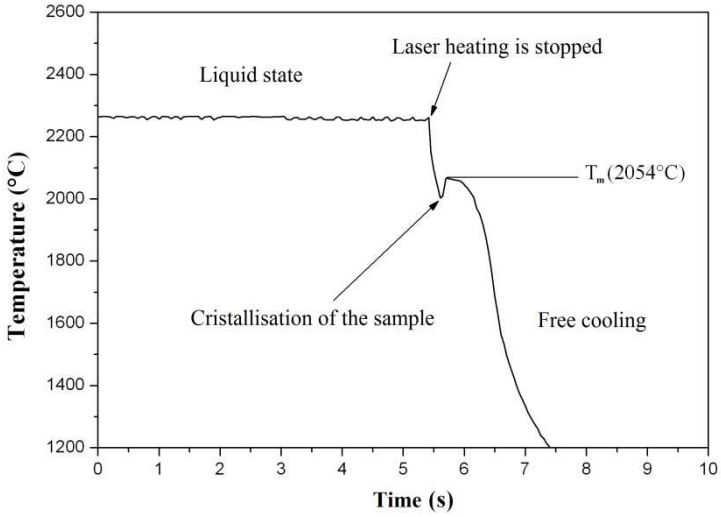

Figure 2.8 Cooling curve of a levitated liquid alumina sample after switching off the lasers.

2.4 Instrumentation developments

Over the past few years, the CEMHTI has developed various kinds of aerodynamic levitation setups to combine this technique with x-ray and neutron diffraction at large-scale facilities. Whereas x-ray techniques are now well exploited for levitation studies of liquids (e.g. x-ray diffraction (XRD) [2,12], x-absorption spectroscopy (XAS) [19] and anomalous x-ray scattering [20,21], the use of neutron techniques is still underexploited.

However, in order to have a full understanding of a liquid's properties, the knowledge of its atomic structure alone is not sufficient. The investigation of its dynamical properties is also required. To this end, aerodynamic levitation was first combined with Inelastic X-ray Scattering (IXS) [22,23] studying longitudinal excitations and estimating relaxation times via a generalized hydrodynamic model. The lower energies of neutrons compared to x-rays should then allow INS to probe more directly the viscosity-related slow relaxation in oxide melts.

Due to the reduced incident flux compared with IXS, hence much lower scattered intensities, aerodynamic levitation was not successfully implemented with Inelastic Neutron Scattering (INS) methods in the past. The general feasibility of a combination of levitation techniques with neutron Time Of Flight (TOF) spectroscopy using relatively small sample sizes has already been shown [16,24]. However, electromagnetic levitation as used in Ref. 16 is limited to electrically conductive samples. And electrostatic levitation discussed in Ref. 24 requires coating or pre-heating of non-conductive samples or samples showing phase transitions during heating, and it is therefore currently also restricted to conductive samples. On the other hand,

aerodynamic levitation has hitherto been limited by the relatively small sample size (about 2.7 mm diameter) that can be levitated using current configurations. Although this sample size is acceptable for neutron diffraction [13,14], it is not reasonable for INS experiments.

By increasing the maximum sample diameter to 4 mm, using appropriate neutron shielding to reduce background, and by making use of a high flux spectrometer, we have succeeded in performing the first TOF-INS experiment on aerodynamically levitated samples.

In the following subsections, I first describe this new laser-heated aerodynamic levitation setup that was designed specifically to be integrated into the TOF spectrometer IN6 at the ILL, and then discuss its optimization.

2.4.1 First Time-Of-Flight aerodynamic levitation

This first high temperature aerodynamic levitation environment was designed and machined in 2009. First tests were performed in October 2009. The setup is presented in Fig. 2.9 and fully described in Refs 25 and 26.

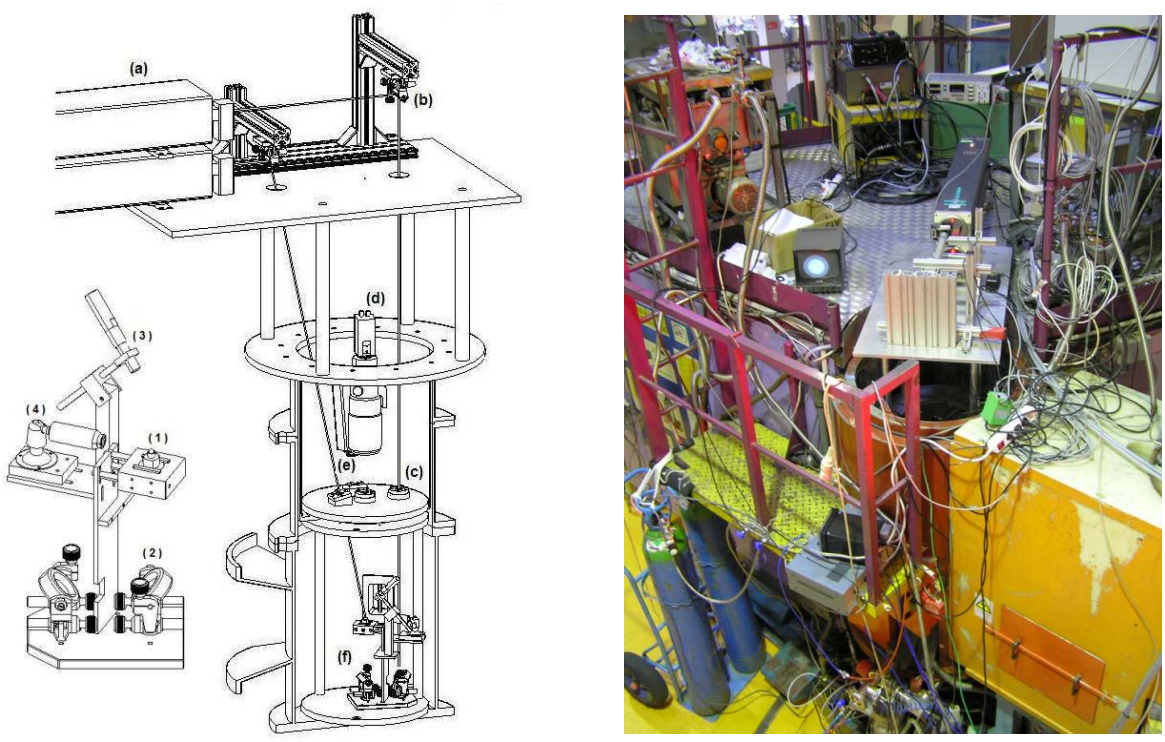

Figure 2.9 Levitation environment designed at the IN6 instrument. lasers (a), mirrors (b), NaCl windows (c), video camera (d), external pyrometer (e) and the levitator (f). The insert shows detail of the levitator: levitator nozzle (1), bottom concave mirror (2), internal pyrometer (3) and side view video camera (4).

For levitating the sample, an aluminum nozzle was used where the primary shape is shown in Fig. 2.10. It is a TOF optimized version of the standard levitation setup currently in service at the D4C neutron diffractometer at the ILL [14]. In fact, the aluminium (Al) nozzle was redesigned to permit sample diameters up to 4 mm which have a volume more than a factor of 3 greater than for a 2.7 mm diameter. One third or one half of the sample is still submerged within the nozzle. However, this does not negatively impact on counting statistics, contrasting with diffraction experiments where a vanadium nozzle is used.

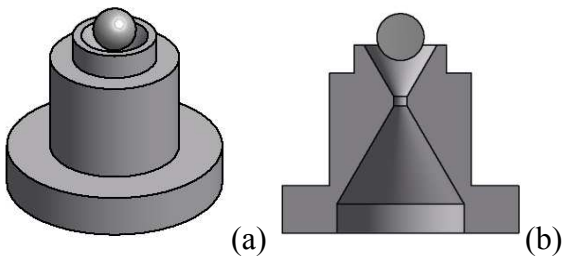

Figure 2.10 (a) Representation of the aluminium nozzle with the levitated sample. (b) Cutaway view highlighting the nozzle head thickness and the convergent-divergent geometry which allows a simple access of a laser beam onto the sample from below.

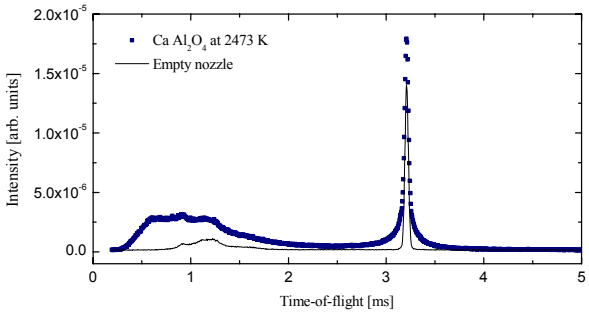

Figure 2.11 Measured Intensity of the sample at 2473 K and of the empty aluminium nozzle at a wavelength of 5.1 Å. This clearly shows that Al atoms have a different vibrational spectrum in the nozzle as compared to the sample and that the two spectra can easily be distinguished and separated.

The chosen wavelength of 5.1 Å and 4.1 Å is above the Bragg cutoff of aluminium. Hence, elastic scattering of the nozzle is strongly reduced and inelastic scattering is well separated from the region of interest around the elastic line as illustrated in Fig. 2.11.

As mentioned previously, inelastically scattered neutrons have a much lower intensity than the elastically scattered ones and so the acquisition time in a QENS measurement is longer than a diffraction experiment. Along with the capability of levitating bigger sample size, can we reduce further the acquisition time? It is a question of statistics that is Poisson like. This could be done by reducing further the background contribution to the signal measured. This will be especially appreciated during the phase of undercooling due to the limitation in sample size needed to overcome heterogeneous nucleation.

For this reason, many tests and technical interventions had to be performed during experiments under the neutron beam:

- Improvement of the shielding and collimation around the levitation part.
- Optimisation of the shape of the nozzle.
- Study of the effect of the surrounding atmosphere

2.4.2 Optimization of the shielding and collimation

The first step consisted of reducing the background resulting from the incident beam hitting parts of the levitator. Therefore, we installed and optimized the shielding of these parts by using cadmium foils. A circular cadmium collimation mask was mounted in front of the nozzle (Fig. 2.13) limiting the beam size to slightly larger than the sample.

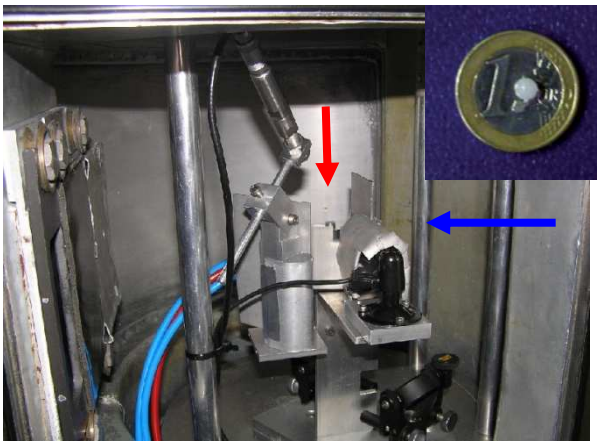

Figure 2.12 Photograph showing the part of the levitation set-up within the sample chamber of the IN6 time-of-flight spectrometer. Red arrow indicates the nozzle and, hence, the sample position. The incident beam direction is indicated by the blue arrow. Insert highlights the size of the glassy sample.

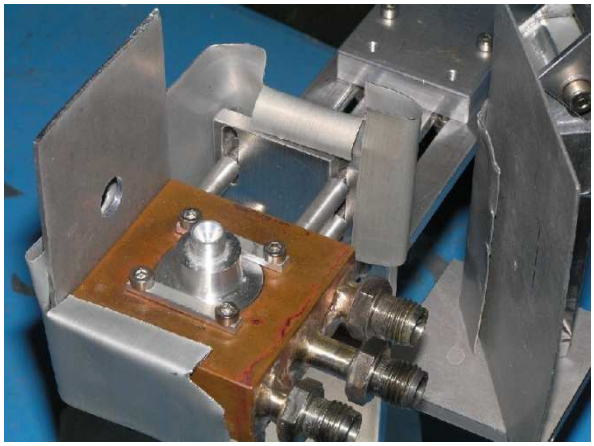

Figure 2.13 Photograph showing the cadmium shielding around the levitator, as well as the circular Cd collimation mask at left for the incident beam.

After each modification in shielding and collimation, the background scattering was remeasaured and compared with the previews.

2.4.3 Optimisation of the nozzle

Since inevitably some of the incident beam will strike the Al nozzle of the IN6 setup, the amount of Al in the beam should be minimized. However, the nozzle must remain thick enough in order to remain cool by conducting waste heat. The design of the nozzle can therefore be optimized with respect to these two constraints.

As it can be seen from Fig. 2.11, the contribution of the empty nozzle compared to the total signal is relatively low. Nevertheless, the nozzle was further machined in order to reduce the amount of Aluminum in the beam. In particular, we made a conical nozzle head shape (Fig. 2.14).

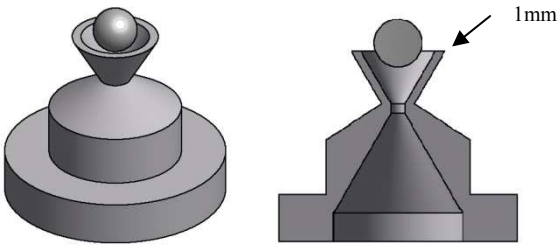

Figure 2.14 New optimized conical geometry of the nozzle with a head thickness reduced to 1 mm.

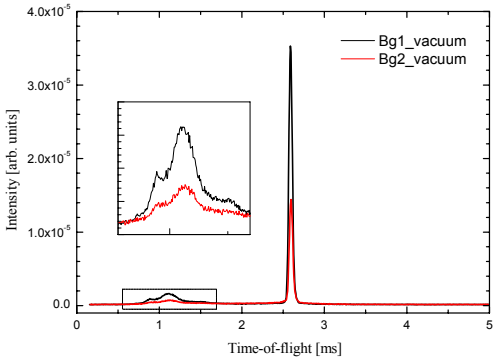

Figure 2.15 Comparison of the background obtained with the straight (black) and conical nozzle (red).

Figure 2.15 shows the difference in background between the 2 configurations. The improvement is obvious.

The nozzle then underwent different optimization stages trying to reach the minimum nozzle head thickness while maintaining a good thermal conductance. This resulted in four optimized nozzles in total that were used in the present work for INS-TOF experiments as listed below in Table 2:

Nozzle	Sample size [mm]	Head thickness [mm]	Use
Bg1	4	1 (straight)	High temperatures
Bg2	4	1 (cone)	High temperatures
Bg3	4	0.5 (cone)	High temperatures
Bg4	2.7	0.5 (cone)	Undercooling

Table 2. Summary of the different optimized nozzle geometries and their use.

Careful tests were performed to optimize the cooling of such nozzles. For this reason, the nozzle's support (Fig. 2.13) was made of high thermal conductivity material (copper) and water-cooled continuously during the experiment.

2.4.4 Study the effect of oxygen content in the levitation gas

In most cases, it is possible to make measurements with low oxygen content in the levitation gas. Usually we use a mixture of argon with 3.5% of oxygen. For silica rich samples for instance, it is necessary to increase the oxygen content to avoid evaporation of the more volatile SiO_2 component and thus a change in stoechiometry of the sample especially during very long acquisition time.
It was thus important to look carefully at the evolution of the background with the gas composition. In Fig. 2.16, the blue and red curves depict the background obtained with a mixture of pure argon and argon with 20% oxygen. We can clearly observe and quantify the scattering from oxygen close to the elastic line. This is then taken into consideration during the data treatment process.

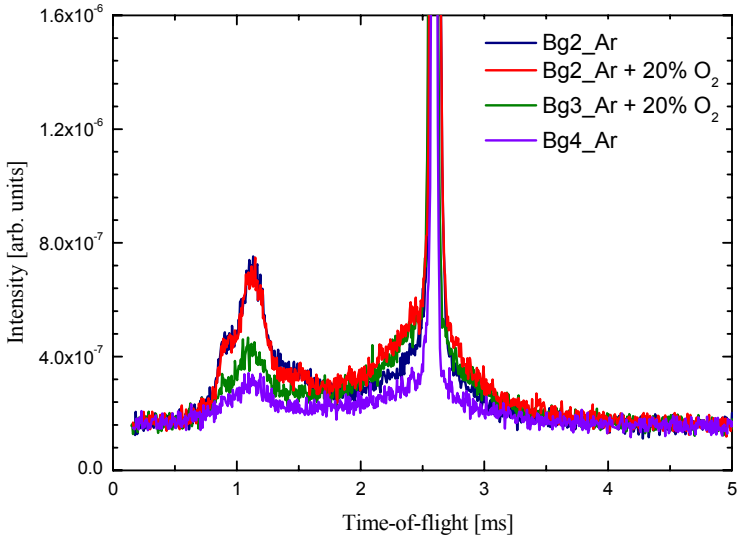

Figure 2.16 Evolution of the background for various configurations.

If we compare the same mixture but with different nozzle head thickness (Bg2_1mm and Bg3_500µm corresponding to the red and green curve respectively), we can see that the scattering contribution from the levitation gas near the elastic line stayed approx. the same whereas the nozzle Al contribution decreased by ~50%. This confidently confirms that the quasi-elastic signal measured is that of the levitation gas at the sample position and not that of the Al nozzle.

2.5 Work towards future improvements.

Motivated by the results of the experiments performed with the standard aerodynamic levitation furnace described in the previous section, we have investigated the possibility to levitate the samples well above the nozzle.

Currently, only two third or one half of the sample protrudes from the nozzle, but this is only viable for working at wavelengths far from the Bragg cutoff of the nozzle's material. Otherwise, even with an efficient collimation, one cannot prevent some neutrons to scatter from the nozzle and this leads background scattering that is particularly troublesome in the case of strong Bragg peaks from e.g. aluminium.

With the current technique, the levitation gas is driven onto the sample from below that will counteract gravity and lift it slightly above the nozzle. The horizontal position of the sample is not very stable; however, the oscillations are damped due to the proximity to the internal wall of the nozzle.

In order to start investigating different levitation configurations that will allow us to levitate the sample higher, Computational Fluid Dynamics (CFD) studies were carried out during the initial phase. A predictive numerical model of the current setup was first made. The model was validated by comparing the results of both numerical and experimental tests performed on solid alumina, Bohr and steel samples for different diameters.

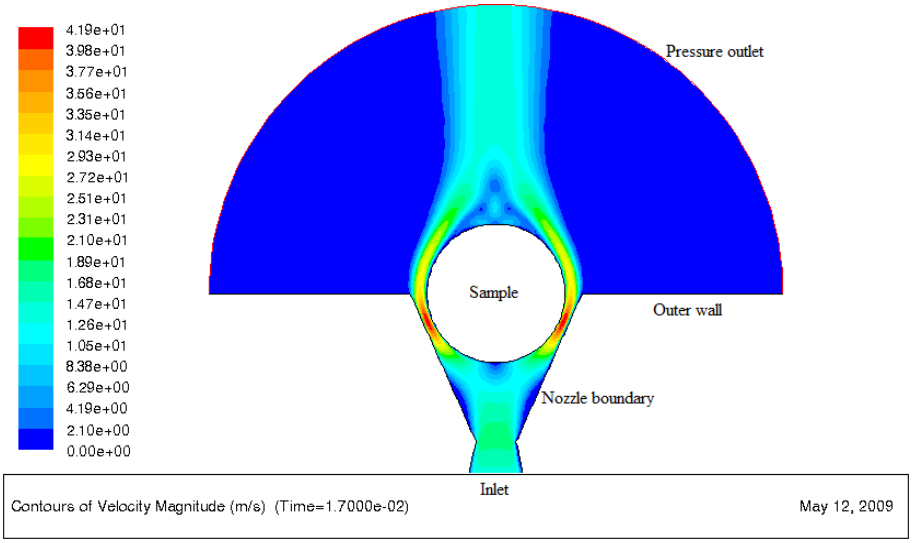

Figure 2.17 2D CFD simulation of a half levitated 4mm sample.

Fig. 2.17 presents the result of a 2D simulation that shows the contours of velocity magnitude around a half levitated 4 mm sample. In this simple static model, the sample is positioned at the

desired height. From simple aerodynamic calculations, one can estimate the mass flow needed to create an opposing force, $\vec{F}_{\text{aero}}$, on the sample in order to overcome its weight. This would give an estimate value of the inlet velocity. By integrating all the resulting aerodynamic forces on the sample geometry, one can match an equilibrium that corresponds to the experimental results.

In the example presented in Fig. 2.17, the velocity of the gas at the inlet of the nozzle is 15 m/s. The velocity then increases to ~ 20 m/s at the throat of this convergent divergent nozzle before reaching its maximum when the gas is flowing through the minimal area between the sample and the inner wall of the nozzle. This velocity is critical in such levitation configuration. An increased velocity will then result in a Venturi effect where the static pressure under the sample would decrease and the sample is stuck to the nozzle independently of inlet mass flow / velocity.

The detailed discussion about the model and the simulations outcome will not be presented in this thesis mainly because the CFD work was interrupted at some point in order to switch to experimental parametrical studies. When the simulations are resumed at a later stage, the complete work will then be presented.

A first prototype was then built based on the Bernoulli principle. The sample was injected into a sufficient gas stream in order to be fully levitated as shown in Fig. 2.18. Owing to the Bernouilli's principle, an increase in the speed of the fluid occurs simultaneously with a decrease in pressure or a decrease in the fluid's potential energy, which gives rise to a horizontal centering force.

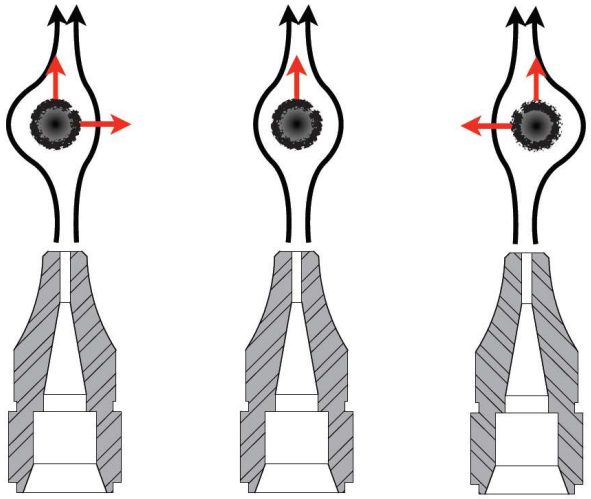

Figure 2.18 Bernouilli's principle applied to levitation: the suction is sufficient to overcome the weight of the spherical sample and the pressure differences tend to maintain the sample on the axis.

While the aerodynamic forces applied on the sample insure its vertical levitation, the change in momentum of the surrounding gas on each side will result in an opposite pressure difference and corresponding force that pushes back the sample to its middle position. However, it is hard to maintain a stable position of the sample because the flow is not laminar. Fig. 2.19 shows a photograph of an unstable levitated sample during the tests. The sample is vibrating in all directions with a remarquable vertical oscillations of about 15 mm.

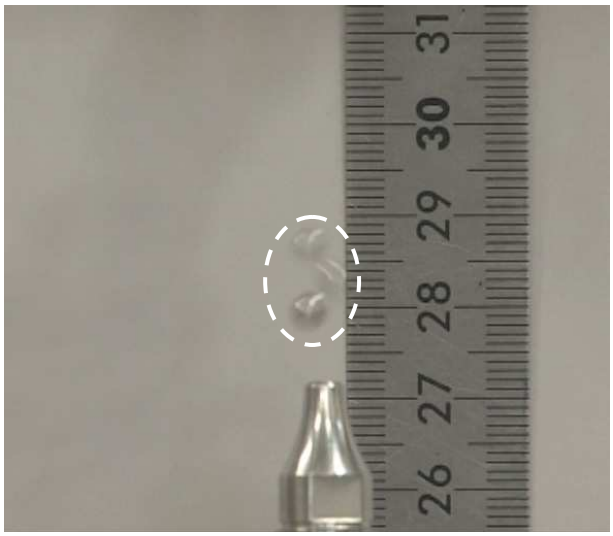

Figure 2.19 Unstable levitation based on the Bernoulli principle using a simple gas jet from below. The doted white oval delimits the oscillations range.

To avoid this problem, a secondary jet was added parallel to the main jet but directed in the opposite direction and off centred by the size of the sample as shown in Fig. 2.20.

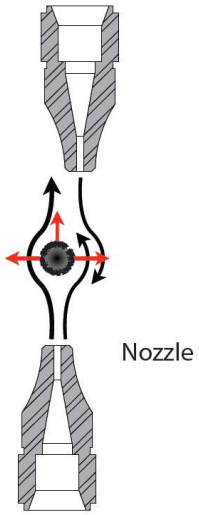

Figure 2.20 Double (Up/Down opposing) nozzle system: a way to horizontally stabilize the sample due the aerodynamic forces generated by the Magnus effect.

This technique breaks the symmetry of the main jet and seems to stabilize perfectly the horizontal position of the sample. And so using a double (Up/Down opposing) nozzle system allow us to control the height of the sample by adjusting independently the gas flow rates of each nozzle. Similarly, the addition of a third jet in a perpendicular (horizontal) and offset direction reduces the vertical oscillations. Schlieren photography measurements are planned to investigate the influence of these secondary jets.

We have extensively tested this innovative technique with samples of different sizes and densities, different geometries of nozzles and several gases. We summarize in the next graph (Fig. 2.12) the optimum argon flow rates for Ø2, Ø4 and Ø6 mm samples made from aluminium, stainless steel and lead in order to see the effect of mass density. The horizontal and vertical axes are the flow rates for the main (lower) and secondary (upper) nozzles respectively.

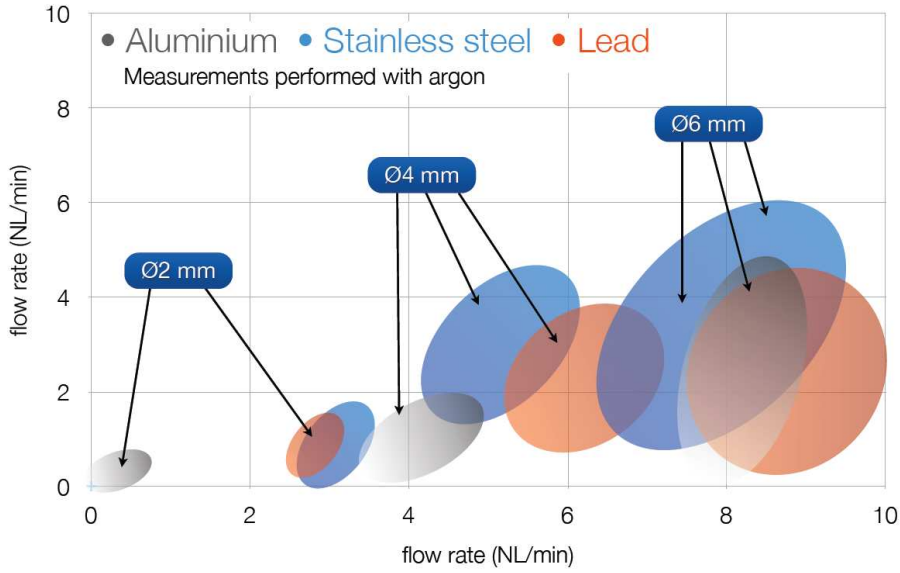

Figure 2.21 Optimum argon flow rates for different sample diameter / material density using the multiple nozzle aerodynamic levitation technique.

This multi-nozzle technique is very efficient and allows the levitation of light and heavy samples over long times, especially when using high-density gases. The horizontal oscillations of the samples do not exceed 0.1 mm and the vertical ones are reduced to about 0.5 mm. With a 125W 10 µm pulsed CO_2 laser, we have verified successfuly the possibility to levitate melted samples. However, the maximum temperature is determined by the reduction of the surface tension of the melt which leads to aerodynamic instabilities. A containerless furnace is now under construction that will include up to 4 motorized nozzles, a pyrometer, a camera and a sample manipulator.

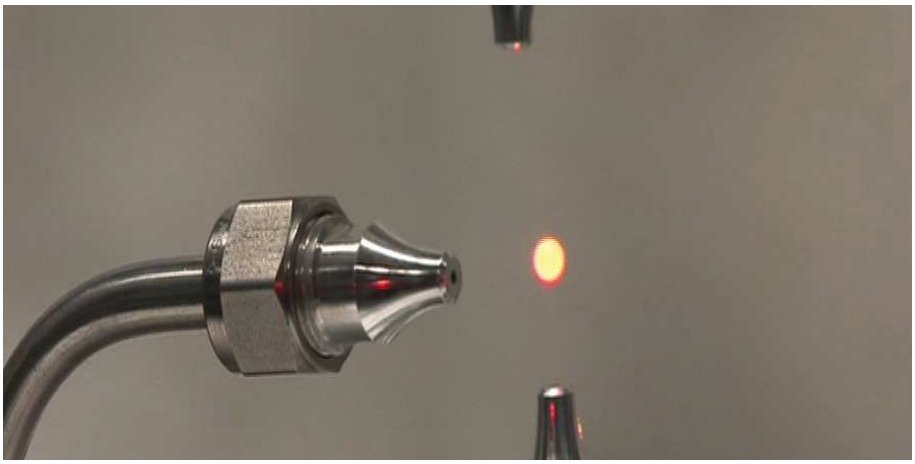

Figure 2.22 Photograph of a levitated molten sample in the innovative multiple nozzle aerodynamic levitation technique.

REFERENCES

[1] D.L.Price; High-temperature Levitated Materials, Cambridge University Press (2010).

[2] L. Hennet, D. Thiaudière, M. Gailhanou, C. Landron, J.P. Coutures and D. L. Price, Review of Scientific Instruments 73 124 (2002).

[3] G. N. Greaves, M. C.Wilding, F. Kargl, L. Hennet, O. Majérus, Adv. Mat. Res. 39-40 3-12 (2008).

[4] L. B. Skinner, A. C Barnes, P. S. Salmon and W. A. Crichton, J. Phys. Condens. Matter 20, 205103 (2008).

[5] E. H. Trinth, Rev. Sci. lnstrum. 56, 2059-07 (1985).

[6] D. Holland-Moritz, T. Schenk, P. Convert, T. Hansen, and D. M. Herlach, Meas. Sci. Technol. 16, 372 (2005).

[7] G. Jacobs, I. Egry, K. Maier, D. Platzek, J. Reske, and R. Frahm, Rev. Sci. Instrum. 67, 3683 (1996).

[8] K. Eckler, Dissertation, Fakultät für Physik und Astronomie der Ruhr- Universität Bochum (1992).

[9] P. F. Paradis, T. Ishikawa, J. Yu, and S. Yoda, Rev. Sci. Instrum. 72, 2811 (2001).

[10] D. A. Winborne, P. C. Nordine, D. E. Rosner and N. F. Marley, Metall. Trans. B 7, p. 711 (1976).

[11] J. P. Coutures, D. Massiot, C. Bessada, P. Echegut, J. C. Rifflet and F.Taulelle, C. R. Acad. Sci. 310 Ser. II, p. 1041 (1990).

[12] L. Hennet, I. Pozdnyakova, A. Bytchkov, D. L. Price, G. N. Greaves, M. Wilding, S. Fearn, C. M. Martin, D. Thiaudière, J.-F. Bérar, N. Boudet and M. L. Saboungi, Journal of Chemical Physics 126 074906 (2007).

[13] L. Hennet, I. Pozdnyakova, V. Cristiglio, G. J. Cuello, S. Jahn, S. Krishnan, M-L. Saboungi and D. L. Price, J. Phys. Cond. Mat. 19, 455210 (2007).

[14] L. Hennet, I. Pozdnyakova, A. Bytchkov, V. Cristiglio, P. Palleau, H. E. Fischer, G. J. Cuello, M. Johnson, P. Melin, D. Zanghi , S. Brassamin , J.-F. Brun and D. L. Price, M.- L. Saboungi, Rev. Scient. Instrum. 77, 053903 (2006).

[15] C. Landron, L. Hennet, J. P. Coutures, T. Jenkins, C. Aletru, N. G. Greaves, A. K. Soper, and G. Derbyshire, Rev. Sci. Instrum. 71, 1745 (2000).

[16] A. Meyer, S. St¨uber, D. Holland-Moritz, O. Heinen and T. Unruh, Phys Rev. B. 77, 092201 (2008).

[17] J. K. R. Weber, C. A. Rey, J. Neuefeind, and C. J. Benmore, Rev. Sci. Instrum. 80, 083904 (2009).

[18] L. Hennet, D. Thiaudiere, M. Gailhanou, C. Landron, J. P. Coutures and D. L. Price, Rev. Sci. Instrum. 73, p. 124 (2002).

[19] C. Landron , L. Hennet , J. P. Coutures , M. Gailhanou, M. Gramond and J. F. Berar, Europhysics Letters 44 429 (1998).

[20] L. Hennet, D. Thiaudière, C. Landron, P. Melin, D. L. Price, J.P. Coutures, J.-F. Bérar and M.L. Saboungi, Applied Physics Letters 83 3305 (2003).

[21] L. Hennet, D. Thiaudière, C Landron, J.-F. Bérar, M.-L. Saboungi, G. Matzen and D. L. Price, Nuclear Instruments and Methods in Physics Research Section B 207 447 (2003).

[22] H. Sinn, B. Glorieux, L. Hennet, A. Alatas, M. Hu, E. E. Alp, F. J. Bermejo, D. L. Price and M.-L. Saboungi, Science 299 2047 (2003).

[23] I. Pozdnyakova, L. Hennet, J.-F. Brun, D. Zanghi, S. Brassamin, V. Cristiglio, D. L. Price, F. Albergamo, A. Bytchkov, S. Jahn, M.-L. Saboungi, Journal of Chemical Physics. 126 114505-1-4 (2007).

[24] D. Holland-Moritz, FRM-II News No.4, page 7.

[25] J. Kozaily, R. Ammer, M. Koza, H. Fischer, E. Lelièvre-Berna, L. Hennet, S. Magazu and F. Kargl, ILL News 51 8-9 (2009).

[26] J. Kozaily, L. Hennet, H. E. Fischer, M. Koza, S. Brassamin, S. Magazu and F. Kargl, Phys. Stat. Sol. C **8**, No. 11–12, 3155–3158 (2011).

Résumé du Chapitre 3

Ce chapitre est une description des principales techniques utilisées pour notre étude expérimentale sur la structure et la dynamique des liquides. Après quelques généralités, une première partie décrit la diffraction et la diffusion quasi-élastique des neutrons et une deuxième partie détaille la diffusion inélastique des rayons X.

Dans la première partie de ce chapitre, nous présentons les techniques de diffraction de neutrons ainsi que les fondements théoriques associés. Les notions de section efficace et sa relation avec le facteur de structure statique, de diffraction cohérente et incohérente y sont abordées. Ensuite nous présentons la spectroscopie QENS en tant que technique qui permet d'avoir accès au facteur de structure dynamique $S(Q,\omega)$ du système dans un domaine de moments de transfert (Q) et énergies (ω). L'utilisation de la méthode en temps de vol (TOF) pour effectuer la diffusion quasi-élastique des neutrons est détaillée avec le traitement de données associé permettant d'extraire les temps de relaxation via le modèle KWW (Kohlrausch-Williams-Watts). Cette méthode expérimentale est particulièrement bien adaptée à l'étude de la dynamique des liquides,

Dans la seconde partie de ce chapitre, la diffusion inélastique des rayons X (IXS) est présentée. Cette technique a été largement utilisée pour l'étude des systèmes désordonnés. Elle permet d'extraire les relations de dispersion ainsi que la vitesse du son. Ce chapitre se termine par une description de la méthode utilisée pour l'analyse des données des mesures IXS. En particulier nous montrons comment passer de l'intensité diffusée au facteur de structure dynamique. Nous décrivons aussi le modèle viscoélastique qui nous sert à exploiter ces courbes afin d'en extraire les quantités physiques importantes, notamment la viscosité longitudinale de nos systèmes.

CHAPTER 3

3 NEUTRON AND X-RAY TECHNIQUES

This chapter gives a basic introduction to the neutron and X-ray scattering experimental techniques that were used for the measurements in this work. The first section outlines some details specific to the theory of neutron scattering whereas the second section gives some background to the synchrotron inelastic X-ray scattering technique. The data treatment of the different experiments is discussed in the corresponding section.

3.1 Neutron scattering

3.1.1 Basic properties of the neutron

The neutron is best known for being a basic constituent of atoms. In science, it is also used as a probe in scattering experiments. Neutrons are particularly useful for studying materials physics because of their unique combination of physical properties such as mass, charge and spin. The neutron was discovered by James Chadwick in 1932 as a result of his measurements on irradiated by alpha particles beryllium [1].

Property	Value
charge	0
spin	½
mass	1.675×10^{-27}kg

Table 3. Basic properties of neutron.

From the de Broglie relationship and the value of Planck's constant h, we know that all particles of mass m, and velocity v have a wavelength λ,

$$\lambda = \frac{h}{mv} \tag{3.1}$$

Using common equations [2] linking the temperature T, kinematic energy E, velocity v, wavelength λ and the wave vector k, we can deduce the following relations:

$$\lambda = 6.283\frac{1}{k} = 3.956\frac{1}{v} = 9.045\frac{1}{\sqrt{E}} = 30.81\frac{1}{\sqrt{T}} \tag{3.2}$$

$$E = 0.08617T = 5.227v^2 = 81.81\frac{1}{\lambda^2} = 2.072k^2 \tag{3.3}$$

Where T is in kelvin, E in meV, v in km.s^{-1}, λ in Å and k in 10^{10} m^{-1}.

3.1.2 Neutron sources

There are two methods currently employed to generate neutrons for use in scattering experiments, each with its pros and cons. The first method is nuclear fission, occurring in a traditional nuclear reactor with uranium as the fuel.

$$^{235}U + n \rightarrow 2.5n + 200\text{MeV} + nuclei$$

A reactor at a neutron scattering facility would be designed to produce an excess of neutrons beyond that required to maintain the chain reaction, and it is these excess neutrons which are used for scattering, once they make their way to the instruments.

But before, their velocity (and hence wavelength) is altered within the reactor by allowing them to reach thermal equilibrium with a moderator, giving a Maxwell-Boltzmann distribution with a peak around the moderator temperature (such as graphite at 2000 K for hot neutrons, water for thermal neutrons and heavy water D_2O for cold neutrons).

This provides large numbers of neutrons with particular ranges of wavelengths (Table 4). The wavelength of thermal neutrons is on a scale similar to interatomic distances within matter, enabling effective probing of the structural and dynamical properties of liquids and solids.

Source	Energy E/meV	Temperature T/K	Wavelength $\lambda/10^{-10}$ m
Cold	0.1-10	1-120	30-3
Thermal	5-100	60-1000	4-1
Hot	100-500	1000-6000	1-0.4

Table 4. Approximate neutron energies, temperatures, and wavelengths for cold, thermal and hot neutrons.

The other method of generating neutrons for scattering is with a spallation source. Accelerated protons strike a heavy metal target, and the impact of the proton beam triggers a nuclear reaction. The spallation process is the excitation and neutron emission of the target until it reaches a stable nuclear state. The spectrum of the neutrons is, as with a reactor source, modified by moderators. Such a source typically produces a lower flux of neutrons than a reactor. This is one main advantage of a reactor source is that it produces a high flux of neutrons at a steady state rate. On the other hand, the pulsed time structure of the neutron beam from a spallation source allows a larger fraction of the neutrons to be counted in a diffraction pattern.

3.1.3 Neutron diffraction theory

The derivation of the following results can be found in more detail in, for example, the book by Squires [2] or Lovesey [3]. Here, the important results are simply stated without their associated proofs.

In a scattering experiment, a beam of radiation (neutrons, photons, electrons, etc.) interacts with the sample and the resulting distribution of the scattered radiation from the sample is then measured through detectors placed at particular positions in (Q,ω) space. For now, we only consider that the incident energy $\hbar\omega_0$ of the neutron is larger than any energy exchange $\hbar\omega$ between a neutron and the sample, in other words, we assume the static approximation.

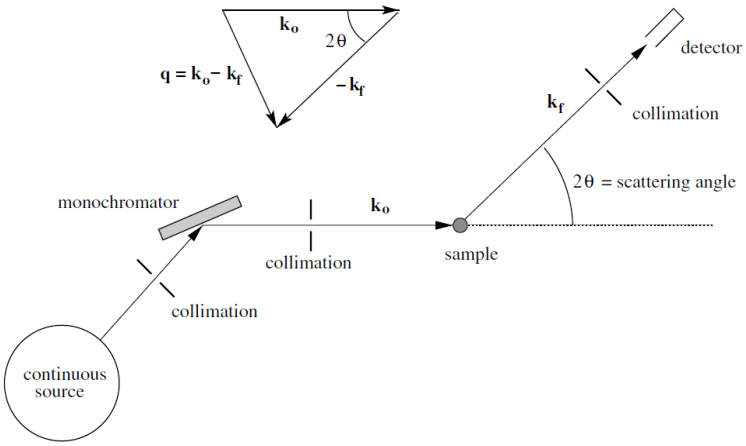

Figure 3.1 Schematic of a typical diffraction experiment from a continuous source of neutrons or x-rays. The scattering triangle of wavevectors is shown at the top [4].

In a neutron scattering experiment, the main interactions are of magnetic and nuclear origin. However, in the present work, our system is not magnetic and the entire scattered intensity comes from the nucleus-nucleus interaction of the neutron with atoms in the sample. The magnitude of these interactions for a given species of nuclei is given by the cross-section σ, measured in barns (1 barn = 10^{-28}m^2). In fact, σ is the effective area of the target as viewed by the incident neutrons.

Cross-Sections

Let us first consider a neutron scattering event from a single isolated nucleus *i*. An incident monochromatic beam of particles is mathematically represented by a wavefunction, $\Psi(\mathbf{r})$ and the probability of finding the particles in an infinitesimal volume dV is $|\Psi(\mathbf{r})|^2 \mathrm{d}V$.

The incident neutron wavepacket before scattering is considered to be an infinite plane wave,

$$\Psi_0 = \exp(\mathrm{i}k_0 z) \tag{3.4}$$

Where k_0 is the incident wavevector and z is the position of the neutron. After scattering, the single nucleus provides a weak perturbation to the incident neutrons and the scattered neutrons are then described by spherical waves,

$$\Psi_{SC} = -\frac{b_i \exp(\mathrm{i}k_f r)}{r} \tag{3.5}$$

where r is the distance from the scattering centre, k_f the magnitude of the final wavevector and b_i is the scattering length for the scattering centre *i*. Since ψ_SC is dimensionless, b_i has dimensions of length and the minus sign in the equation represents the convention in neutron scattering that a positive scattering length corresponds to a repulsive scattering potential.

However, the model of the neutron interacting with a nucleus contains some simplifications known as the "Born approximation". We assume that the nuclear potential is of a short range and we define the Fermi pseudopotential as $V(\mathbf{r}) = (2\pi\hbar^2 b_i / m)\delta(\mathbf{r} - \mathbf{R}_i)$. Here r denotes the position of the neutron and $\mathrm{R_i}$ the position of nucleus *i*. This can be thought of as indicating that most of the neutrons "miss" the nucleus and only a small fraction are scattered.

We define the total cross-section σ as,

$$\sigma = \frac{\text{Total no. particles scattered in all directions per sec.}}{\text{Incident flux } (I_0)} \tag{3.6}$$

The flux of particles is generally defined as the number of incident particles per unit normal area per second and is the product of the particle density and the velocity. We can then write the incident and the scattered flux at a distance *r* respectively as:

$$I_0 = |\Psi_0|^2 v = v \tag{3.7}$$

$$I_{SC} = |\Psi_{SC}|^2 v = b^2 v / r^2 \tag{3.8}$$

where $|\Psi|^2 = \Psi\Psi^*$. And so the total number of particles scattered per second is equal to the flux multiplied by the total area at distance *r*. In case of an isolated nucleus, this could be written as:

$$\begin{aligned} \text{Total no. particles scattered per sec.} &= I_{SC} \times \text{total area} \\ &= b^2 v / r^2 \times 4\pi r^2 \\ &= 4\pi b^2 v \end{aligned} \tag{3.9}$$

And thus the total cross-section,

$$\sigma = 4\pi b^2 \tag{3.10}$$

Let us now define the differential cross-section by:

$$\frac{d\sigma}{d\Omega} = \frac{\text{No. particles scattered into solid angle } d\Omega \text{ per sec.}}{I_0 \times d\Omega} \tag{3.11}$$

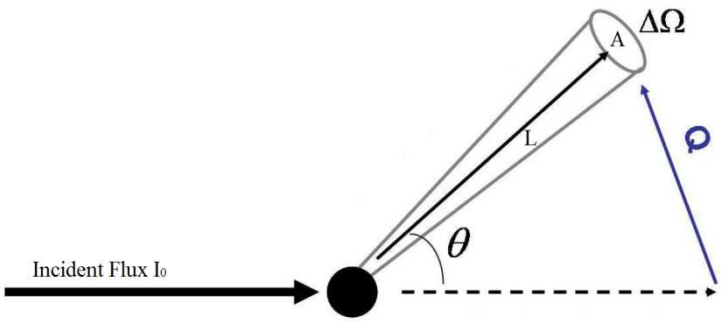

Figure 3.2 Illustration of parameters pertinent to the definition of a differential scattering cross-section.

The solid angle subtended by the detector at the sample is $\Delta\Omega = A/L^2$. From the definition of the differential cross section, the number of particles detected per second could be written as,

$$\text{no. particles detected per sec.} = I_0 \Delta\Omega \frac{\mathrm{d}\sigma}{\mathrm{d}\Omega} \tag{3.12}$$

But also, from equation (3.8), the number of particles detected per second is = $\left|\Psi_{SC}\right|^2 v \times A$, and so the differential cross section is,

$$\frac{\mathrm{d}\sigma}{\mathrm{d}\Omega} = \frac{\left|\Psi_{SC}{}^2\right|}{\left|\Psi_0{}^2\right|} L^2 \tag{3.13}$$

For an isolated nucleus, the scattered wave at the detector is $\Psi_{SC} = -\dfrac{b\exp(\mathrm{i}kL)}{L}$, and so

$$\frac{\mathrm{d}\sigma}{\mathrm{d}\Omega} = b^2 = \frac{\sigma}{4\pi} = \frac{\text{total cross section}}{\text{solid angle of a whole sphere}} \tag{3.14}$$

Now if we consider the differential cross-section for an assembly of nuclei N. We assume that the distance L_i (i=1,...,N) between any scatterer "i" and the detector is much bigger than d_{ij}, where d_{ij} is the biggest possible distance of two scattering nuclei in the sample. We can then make the approximation that $L_{i=1,..N} \sim L$, and this allows us to calculate the phase of the neutron wave scattered by an atom at position $\mathbf{r}_n$ (for arbitrary origin and at a given time) as $\mathbf{k}_i.\mathbf{r_n} - \mathbf{k}_f.\mathbf{r_n} = \mathbf{Q}.\mathbf{r_n}$ (i.e. $\mathbf{Q} = \mathbf{k}_i - \mathbf{k}_f$). The total scattered wave measured by the detector can then be written as:

$$\Psi_{SC} = \sum_n \Psi_{SC,n} = -\frac{\exp(\mathrm{i}kL)}{L} \sum_n b_n \exp(\mathrm{i}\mathbf{Q}.\mathbf{r}_n) \tag{3.15}$$

And the differential cross-section as:

$$\frac{\mathrm{d}\sigma}{\mathrm{d}\Omega} = \left| \sum_n b_n \exp(\mathrm{i}\mathbf{Q}.\mathbf{r}_n) \right|^2 \tag{3.16}$$

again, all within the static approximation.

Coherent and Incoherent Scattering:

The differential scattering cross-section is the probability that the neutron is scattered into a specified direction. b_n are the scattering length of the different species within the sample. It characterizes the range of the neutron-nucleus interaction. However, b_n depends on:

a) Which element
b) Which isotope
c) Relative spins of neutron and nucleus.

In principle, we can calculate $d\sigma/d\Omega$ exactly if we know the isotope and spin state of every nucleus. However, this is not feasible in practice. And for this reason, a simplifying assumption need to be made that is the distribution of isotopes and spin states is random and uncorrelated between the sites. And so $d\sigma/d\Omega$ for one particular sample is the same as the ensemble average over many samples with the same nuclear positions, and we can write,

$$\frac{d\sigma}{d\Omega} \approx \overline{\frac{d\sigma}{d\Omega}} \tag{3.17}$$

We note that,

$$\begin{aligned} \frac{d\sigma}{d\Omega} &= \left| \sum_n b_n \exp(i\mathbf{Q}.\mathbf{r}_n) \right|^2 \\ &= \sum_n \sum_m b_n b_m \exp[i\mathbf{Q}.(\mathbf{r}_n - \mathbf{r}_m)] \end{aligned} \tag{3.18}$$

assuming real-valued scattering lengths. If we apply the ensemble averaging, we replace $b_n b_m$ by $\overline{b_n b_m}$ and,

$$\begin{aligned} \overline{b_n b_m} &= \overline{b}_n \overline{b}_m \quad \text{if } n \neq m \\ &= \overline{b_n^2} \quad \text{if } n = m \end{aligned} \tag{3.19}$$

Therefore,

$$\begin{aligned} \frac{d\sigma}{d\Omega} &= \overbrace{\sum_{n \neq m} \sum \overline{b}_n \overline{b}_m \exp[i\mathbf{Q}.(\mathbf{r}_n - \mathbf{r}_m)]}^{\text{distinct scattering}} + \overbrace{\sum_{n=m} \overline{b_n^2}}^{\text{self scattering}} \\ &= \underbrace{\sum_n \sum_m \overline{b}_n \overline{b}_m \exp[i\mathbf{Q}.(\mathbf{r}_n - \mathbf{r}_m)]}_{\text{coherent scattering}} + \underbrace{\sum_{n=m} (\overline{b_n^2} - \overline{b_n}^2)}_{\text{incoherent scattering}} \end{aligned} \tag{3.20}$$

We can see that $\mathrm{d}\sigma/\mathrm{d}\Omega$ can be decomposed into a 'coherent' part and an 'incoherent' part, as shown by equation (3.20). The coherent part concerns diffraction from all atomic sites, including the 'self-scattering' from a single atom, but is independent of the distribution in scattering lengths; it is a function of the average scattering length alone. The incoherent part, by contrast, is independent of the spatial correlation of the atomic sites and depends only on the distribution of scattering lengths present in the sample, leading to isotropic diffraction.

Alternatively, and at particular utility for polyatomic samples, we can decompose $\mathrm{d}\sigma/\mathrm{d}\Omega$ into a « distinct » part (interference between 2 different atoms) and a « self » part (interference of an atom with itself).

By defining the static structure factor $S(Q)$ as,

$$S(Q) = \frac{1}{N}\sum_{\mathrm{n}}\sum_{\mathrm{m}} \exp[\mathrm{i}\mathbf{Q}.(\mathbf{r}_{\mathrm{n}} - \mathbf{r}_{\mathrm{m}})] \tag{3.21}$$

where N is the total number of atoms, it is dimensionless and converges to 1 as Q goes to infinity, we can write down another more common expression for the differential scattering cross section as:

$$\begin{aligned} \frac{1}{N}\left[\frac{\mathrm{d}\sigma}{\mathrm{d}\Omega}(Q)\right] &= \frac{1}{N}\left[\frac{\mathrm{d}\sigma}{\mathrm{d}\Omega}(Q)\right]_{\mathrm{coh}} + \frac{1}{N}\left[\frac{\mathrm{d}\sigma}{\mathrm{d}\Omega}(Q)\right]_{\mathrm{incoh}} \\ &= \bar{b}^2 S(Q) + (\overline{b^2} - \bar{b}^2) \\ &= b_{\mathrm{coh}}^2 S(Q) + b_{\mathrm{incoh}}^2 \end{aligned} \tag{3.22}$$

3.1.4 Inelastic neutron scattering

Up to now, we have been considering neutron scattering in the static approximation, meaning that the energy loss or gain of the neutron to the sample is always small compared to its incident energy. In the general case, neutrons scatter inelastically and the scattering event must conserve both momentum and energy. This can be expressed by the energy conservation equation as follows:

$$E_{\mathrm{i}} - E_{\mathrm{f}} = \frac{\hbar^2}{2m_{\mathrm{N}}}(k_{\mathrm{i}}^2 - k_{\mathrm{f}}^2) = \hbar\omega \tag{3.23}$$

Where $E_{\mathrm{i,f}} = \hbar^2 k_{\mathrm{i,f}} / 2m_{\mathrm{N}}$ are respectively the incident and the final energies of the neutron, $k_{\mathrm{i,f}} = 2\pi / \lambda_{\mathrm{i,f}}$ are the incident and final neutron wavevectors and $\hbar\omega$ is the energy of excitation in the sample. Meanwhile, momentum conservation gives us,

$$\mathbf{Q} = \mathbf{k}_{\mathrm{i}} - \mathbf{k}_{\mathrm{f}} \tag{3.24}$$

Where Q is the scattering vector. Taken together, equations (3.23) and (3.24) allow us to calculate from a given scattering event the wavevector and energy of the excitations in the sample.

And so with energy analysis of the scattered waves, this gives the double differential cross section, (3.25). That is, the number of waves scattered into a solid angle $\mathrm{d}\Omega$ per second with an energy between E and $E + dE$, which is related to a form factor, f and the dynamic structure factor $S(Q,\omega)$,

$$\frac{\partial^2\sigma}{\partial\Omega\partial E} = \frac{k_{\mathrm{f}}}{k_{\mathrm{i}}} f^2 S(\mathbf{Q},\omega) \tag{3.25}$$

The $k_{\mathrm{f}} / k_{\mathrm{i}}$ factor is sometimes important, for example if the neutron loses a lot of energy ($k_{\mathrm{f}} << k_{\mathrm{i}}$) then the intensity is much reduced. $S(Q,\omega)$ contains all the physics of the system as well as all the scattering that we observe (inelastic or elastic). Similarily, following the formalism described above, we can express the double differential cross section as:

$$\frac{\partial^2\sigma}{\partial\Omega\partial E} = \frac{k_{\mathrm{f}}}{k_{\mathrm{i}}} \frac{1}{N} \sum_{\mathrm{i}} \sum_{\mathrm{j}} \frac{1}{2\pi} \int_{-\infty}^{+\infty} \left\langle b_i b_j \exp\{\mathrm{i}\mathbf{Q}.[\mathbf{r}_{\mathrm{i}}(0) - \mathbf{r}_{\mathrm{j}}(t)]\} \right\rangle \exp(-\mathrm{i}\omega t)\mathrm{d}t \tag{3.26}$$

where the brackets $\langle ... \rangle$ represent the appropriate thermal and ensemble averages and so the scattering function $S(Q,\omega)$ could be written as,

$$S(Q,\omega) = \frac{1}{N} \sum_{\mathrm{i}} \sum_{\mathrm{j}} \frac{1}{2\pi} \int_{-\infty}^{+\infty} \left\langle b_{\mathrm{i}} b_{\mathrm{j}} \exp\{iQ.[r_{\mathrm{i}}(0) - r_{\mathrm{j}}(t)]\} \right\rangle \exp(-i\omega t)\mathrm{d}t \tag{3.27}$$

The principle of detailed balance

It can be shown that the scattering function is an asymmetric function of ω. The up-scattering (neutron energy gain) probability is not same as that of the down-scattering (neutron energy loss). At any given temperature, there will be a fraction $e^{-\hbar\omega / k_{\mathrm{B}}T}$ fewer excitations already

extant for neutrons to scatter from, compared to the number of excitations that can be created by the neutron (i.e. less up scattering than down scattering). This could be expressed as,

$$S(Q,\omega) = e^{-\hbar\omega/k_{\mathrm{B}}T} S(-Q,-\omega) \tag{3.28}$$

The measured intensity is in general a mixture of coherent and incoherent scattering contributions and can be written as follows:

$$\begin{aligned} \frac{\partial^2\sigma}{\partial\Omega\partial E} &= \left[\frac{\partial^2\sigma}{\partial\Omega\partial E}\right]_{\mathrm{coh}} + \left[\frac{\partial^2\sigma}{\partial\Omega\partial E}\right]_{\mathrm{incoh}} \\ &\approx \frac{\sigma_{\mathrm{coh}}}{4\pi} S_{\mathrm{coh}}(Q,\omega) + \frac{\sigma_{\mathrm{incoh}}}{4\pi} S_{\mathrm{incoh}}(Q,\omega) \end{aligned} \tag{3.29}$$

Where

$$\left[\frac{\partial^2\sigma}{\partial\Omega\partial E}\right]_{\mathrm{coh}} = \frac{\sigma_{\mathrm{coh}}}{4\pi}\frac{k_{\mathrm{f}}}{k_{\mathrm{i}}}\frac{1}{2\pi}\sum_{\mathrm{i}}\sum_{\mathrm{j}}\int_{-\infty}^{+\infty}\left\langle \exp\{iQ.[r_{\mathrm{i}}(0) - r_{\mathrm{j}}(t)]\}\right\rangle \exp(-i\omega t)\mathrm{d}t \tag{3.30}$$

$$\left[\frac{\partial^2\sigma}{\partial\Omega\partial E}\right]_{\mathrm{incoh}} = \frac{\sigma_{\mathrm{incoh}}}{4\pi}\frac{k_{\mathrm{f}}}{k_{\mathrm{i}}}\frac{1}{2\pi}\sum_{\mathrm{i}}\int_{-\infty}^{+\infty}\left\langle \exp\{iQ.[r_{\mathrm{i}}(0) - r_{\mathrm{i}}(t)]\}\right\rangle \exp(-i\omega t)\mathrm{d}t \tag{3.31}$$

showing explicitly that incoherent inelastic scattering is sensitive to only the self correlations of a given atom. The scattering function is related to the intermediate scattering function $S(Q,t)$ by the time Fourier-transform,

$$S(Q,\omega) = \frac{1}{2\pi}\int_{-\infty}^{+\infty} S(Q,t)\exp(-i\omega t)\mathrm{d}t \tag{3.32}$$

And by inverse Fourier-transform, we get the intermediate scattering function as follow,

$$S(Q,t) = \hbar\int_{-\infty}^{+\infty} S(Q,\omega)\exp(i\omega t)\mathrm{d}\omega \tag{3.33}$$

The intermediate scattering function is in turn related to the time dependent pair correlation function $G(r, t)$ by the Fourier transform,

$$G(r,t) = \frac{1}{(2\pi)^3}\int S(Q,t)\exp(iQ.r)\mathrm{d}Q \tag{3.34}$$

3.1.5 Time-of-Flight Spectroscopy

One of the best techniques for probing the atomic dynamics of solids and liquids is Inelastic Neutron Scattering (INS), and in particular, the technique of time-of-flight (TOF) inelastic neutron scattering is well-adapted to the study of dynamics in liquid or amorphous samples [5].

In this technique, the energy and momentum transfer of the scattered neutrons are determined simultaneously by measuring the neutron flight time from the sample position to the detectors and the scattering angles. Hence the dynamic scattering function $S(Q,\omega)$ is measured directly over a broad range of Q and ω.

All the neutron time-of-flight experiments in this work were performed on the direct geometry time focusing TOF spectrometer IN6 at the European High Flux Neutron Source of the Institute Laue Langevin (ILL) in Grenoble, France. The instrument provides a high neutron flux at the sample (~10^6 neutrons/cm^2/s) and possesses an excellent signal-to-noise ratio.

Fig. 3.3 illustrates the layout of the IN6 spectrometer. A more detailed description of the instrument could be found in [6]. It is designed for quasi-elastic and inelastic scattering for incident wavelengths in the range of 4 to 6 Å.
In order to measure a change in velocity (energy) at the sample, we need to be able to fix the neutrons incident energy and also chop the beam so as to create a pulse at time = 0. Therefore, the extracted neutron beam from the reactor source will strike a crystal monochromator that provides a monochromatic beam characterized by its energy E_0 and wave vector k_0. To achieve the time-focussing condition, the beam is then pulsed by a Fermi chopper. The pulsed and monochromated beam is then guided to the sample and the scattered neutrons will be detected at the end of the flight path by the detectors.

The detectors are mounted on the detector bank and with an equal sample-to-detector distance of 248 cm. Therefore, the energy of the detected neutrons is determined by the time they need to cross this flight distance and reach the detectors after being scattered by the sample. This time is called the time-of-flight (TOF), which is the inverse of the neutron velocity in the unit of [ms/m]. According to the neutron velocity typical flight times are in the order of milliseconds.

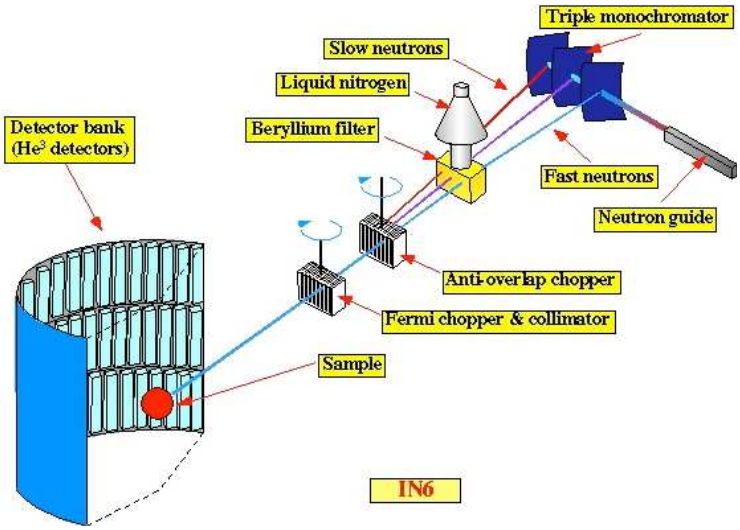

Figure 3.3 Schematic layout of the IN6 time-of-flight spectrometer.

When a bunch of neutrons arrives at the sample, it can be scattered either elastically or inelastically. Fig. 3.4 shows the energy distribution of the neutrons recorded by the detectors. Elastically scattered neutrons ($\hbar\omega = 0$) arrive at the detectors at a time determined by the incident neutron velocity and their flight path. Inelastically scattered neutron, depending on whether they gain ($\hbar\omega < 0$) or lose energy ($\hbar\omega > 0$), will arrive either earlier or later.

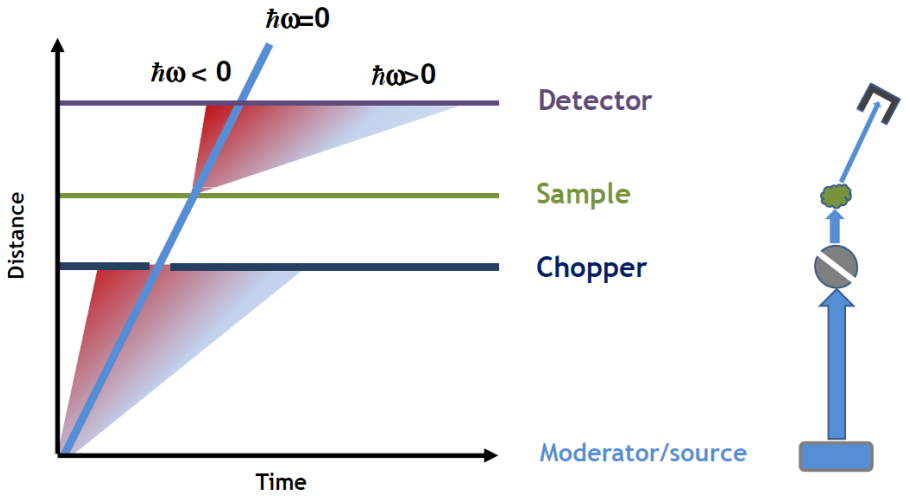

Figure 3.4 Neutrons energy distribution recorded by the detectors in a direct geometry TOF instrument.

However, if the time for the down-scattered ($\hbar\omega < 0$) neutrons to reach the detectors exceeds the time interval between two neutron pulses, there will be frame overlap. For this reason, an anti overlap chopper is placed before the Fermi chopper and collimator. The energy resolution

is determined by the accuracy of measuring the flight time and flight path. The width in time Δt of a pulsed beam when arriving at the detector can be derived directly from the time-distance diagram using purely geometric arguments.

The relation between the momentum transfer Q and the scattering angle for a direct geometry instrument can be expressed as follows:

$$\frac{\hbar^2 Q^2}{2m} = E_\mathrm{i} + E_\mathrm{f} - (E_\mathrm{i}E_\mathrm{f})^{1/2}\cos\theta \tag{3.35}$$

If we eliminate the energy $E_\mathrm{f} = E_\mathrm{i} - \hbar\omega$ from the equation, we get:

$$\frac{\hbar^2 Q^2}{2m} = 2E_\mathrm{i} - \hbar\omega - 2\cos\theta[E_\mathrm{i}(E_\mathrm{i} - \hbar\omega)]^{1/2} \tag{3.36}$$

It can be seen that each detector has a parabolic trajectory through the (Q,ω) space that is illustrated in Fig. 3.5.

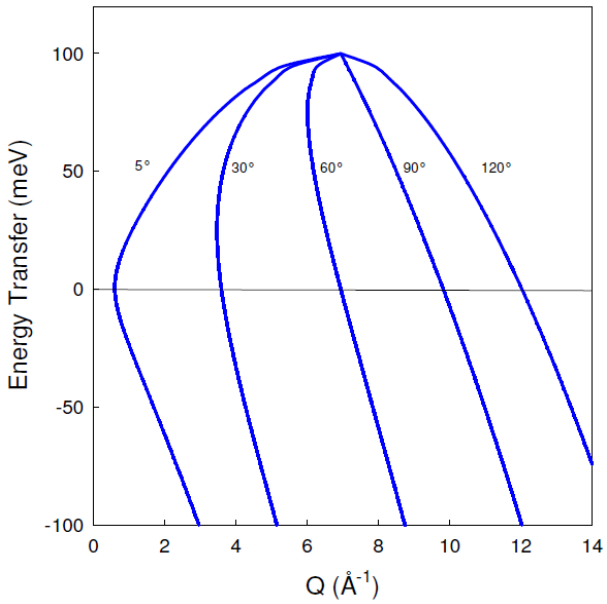

Figure 3.5 INS allowed kinematic region for selected fixed scattering angles.

For this reason, in order to make optimum use of spectrometers, we must equipe them with large detector arrays that allow simultaneous access to a large area of (Q,ω) space.

3.1.6 Data treatment

The measured scattering intensity requires some corrections in order to obtain the desired quantity $S(Q,\omega)$. This includes normalization to the incident beam intensity, subtraction of background intensities from the nozzle and levitation gas, correction for self-absorption of the sample and detector efficiency correction.

All the data corrections were performed using the FRIDA program developed originally by Joachim Wuttke [7].

First, the number of counted scattered neutrons is normalized to the monitor. This makes it independent of the incident neutron flux and counting time. The detector efficiency was corrected by the measurement of a vanadium sample. This is because vanadium is considered to be a pure incoherent scatterer. Only the intensity of the elastic peak of the vanadium sample was taken for the normalization. This normalizes the signal independently of the detection time interval and detection probabilities. Additionally vanadium can be used as a measurement of the instrument's energy resolution, which is the $\Delta\omega$ width of the elastic peak.

All the scattering from other sources besides the sample needs to be removed. This includes the aluminium nozzle, background scattering (e.g. from scattering within the empty instrument, levitator setup in the chamber, electronic noise…). However, a simple subtraction of the background signal is not precise. Attenuation and multiple scattering from the sample should be taken into consideration.

To this point, the spectrum $I(2\theta,tof)$ is still stored in a time channel – angle matrix format. Using the following equation relating the time-of-flight to the energy of the neutron,

$$\hbar\omega = \frac{1}{2} m_{\mathrm{N}} \left[\frac{1}{tof_{\mathrm{el}}^2} - \frac{1}{tof^2} \right] \tag{3.37}$$

(the subscript "el" denotes the elastic tof) and by interpolating the resulting $S(2\theta,\omega)$ to constant wave vector Q, we get finally the scattering function $S(Q,\omega)$. After these corrections, the scattering function $S(Q,\omega)$ is still convoluted with the instrument resolution function,

$$S'(Q,\omega) = R(Q,\omega) \otimes S(Q,\omega) \tag{3.38}$$

In order to analyse the data in the time domain, the Fourier-transform is applied to equation (3.8),

$$\mathrm{F}[\,S'(Q,\omega)\,] = \mathrm{F}[\,R(Q,\omega)\,] \times \mathrm{F}[\,S(Q,\omega)\,] \tag{3.39}$$

and the intermediate scattering function is obtained by simple division by the FT of the resolution function as follows:

$$S(Q,t) = \frac{S'(Q,t)}{R(Q,t)} \tag{3.40}$$

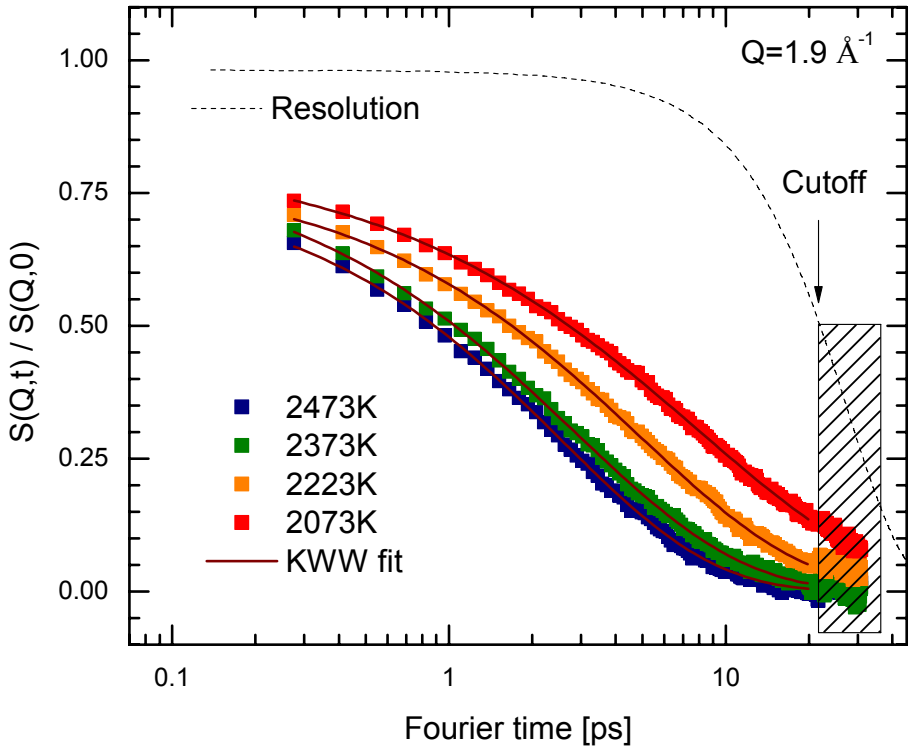

Figure 3.6 Example of $S(Q,t)$ spectra showing the cut-off at large times where the resolution drops to 50% of its initial value.

However, due to the finite range of the energy transfer, a proper $t \to 0$ limit cannot be obtained. Thus, the final normalization to $S(Q,t=0)$ does not correspond exactly to the static structure factor $S(Q)$.

Finally, a cutoff at large times was performed where the resolution function decays to about 50% of its initial value (Fig. 3.6). For times larger than the cutoff time, the spectra are dominated by the instrument resolution function.

3.2 X-ray scattering

3.2.1 The Synchrotron Source

An excellent description of the function of synchrotron light sources, as well as scattering theory for x-rays, may be found in the book by J. Als-Nielsen and D. McMorrow [8]. The following is an outline of the most relevant x-ray instrumentation and theory for this thesis. The x-ray experiments were carried out at the European Synchrotron Radiation Facility (ESRF) in Grenoble, France. The basic principle of a synchrotron light source is very simple: a beam of electrons (although they could be any charged particles) is accelerated in a linear accelerator and then again in a circular accelerator to near light speeds (~6GeV) and is then injected into a storage ring (circumference 844m at ESRF) and allowed to travel at constant speed around an approximately circular path. The acceleration of the electrons as they travel on their curved path results in emission of synchrotron x-rays.

In reality the circular path is made up of many straight sections, and at the end of each one there is a magnetic field which bends the electrons into the next straight section, the so-called bending magnet. The bending magnet is simply a static vertical magnetic field that deflects the electron path (describing a circular arc) due to the Lorentz force. The circularly accelerated electrons emit x-rays in the tangential i.e. forward direction (parallel to the electron beam, with a small divergence of about 0.08mrad) due to the relativistic Doppler effect.

Following the convention of Nielsen and McMorrow [8], let us define the energy of an electron in the synchrotron storage ring as ξ_e. The radius of curvature ρ, for the (useful) units shown in square brackets is given by

$$\rho[m] = \frac{3.3\xi_e[\mathrm{GeV}]}{B[\mathrm{T}]} \tag{3.41}$$

where B is the constant magnetic field applied by the bending magnet. The characteristic energy, $\hbar\omega_c$, of the emitted electrons, i.e. the energy at which the flux is greatest, is given by

$$\hbar\omega_c[keV] = 0.665\xi_e^2[GeV]B[T] \tag{3.42}$$

And the radiated power, P, is given by

$$P[kW] = 1.266\xi_e^2[GeV]B^2[T^2]L[m]I[A] \tag{3.43}$$

Where L is the length of the section over which the electron experiences a magnetic field, and I is the current of electrons in the storage ring.

Insersion Device

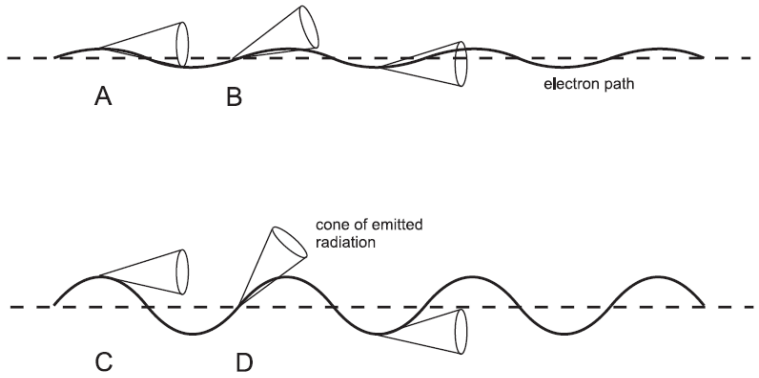

Figure 3.7 A schematic of an undulator (upper figure) and a wiggler (lower figure) insertion device. The cones shown at various points along the electron path show the direction of the emitted radiation.

Synchrotron light may be also be emitted by passing the electron beam through "wigglers" or "undulators" in the straight sections. A wiggler is a periodic array of alternating magnetic fields which cause the electron paths to bend (describing a circular arc) in alternate directions (wiggling), so essentially it is a series of alternating bending magnets. The electrons undergo the same process as with a bending magnet, but several times, so that the emerging radiation is the incoherent sum of $2n$ bending magnets, if the wiggler has n magnet periods. The period of the magnetic fields "seen" by the electrons is affected by relativistic Lorentz length contraction, so that for an array of n magnetic periods with overall length L the electrons see an array of magnets of length L/γ, with a period of $L/n\gamma$, where the relativistic Lorentz factor is given by

$$\gamma = \frac{1}{\sqrt{1-\frac{v_e^2}{c^2}}} \tag{3.44}$$

Where v_e is the speed of the electrons in the storage ring. In the laboratory frame this transforms to approximately $L/2n\gamma$ if $v_e \approx c$. The wavelength of the synchrotron light generated is of the same order of magnitude as the relativistic period of the wiggler magnets as seen in the laboratory frame. The angular divergence of the beam is $\approx 1/\gamma$.

An undulator is similar to a wiggler but works in a slightly different way. Fig. 3.7 shows schematically the main difference. At points like C on the electron path, radiation is emitted

along the electron beam tube and will be incident on the sample, whereas at points like D it will not. For an undulator radiation is emitted along the beam tube on to the sample at both of the corresponding points A and B. The result of this is that the overall intensity of radiation arriving at the sample, rather than striking the walls of the electron beam pipe, is higher for an undulator. In addition the radiation cones from the undulator interfere constructively so that the spectral weight is concentrated around just a few wavelengths (the fundamental and its harmonics), which further increases the available monochromated intensity. All of the experiments presented in this thesis that were performed at insertion device beamlines were performed on undulator beamlines, so detailed discussion of the expected x-ray spectrum from insertion devices is restricted to the case of undulators.

Let us define the magnetic field applied to the electrons, perpendicular to the plane of the undulations, as

$$B_Z = B_0 \sin(2\pi s / \lambda_u) \tag{3.45}$$

Where s is the spatial co-ordinate in the direction of the unbent electron path, λ_u is the period of the magnetic field, and B_0 is the maximum applied field. Define the dimensionless parameter K as

$$K = \frac{e}{2\pi mc}\lambda_u B_0 = 0.934\lambda_u[cm]B_0[T] \tag{3.46}$$

where the right-hand term gives the value in the most useful units. The frequency of emitted radiation from an undulator as a function of off-axis angle θ is given by

$$\omega_{und}(\theta) = \frac{4\pi c\gamma^2 M}{\lambda_u}\left(\frac{1}{1+K^2/2+\gamma^2\theta^2}\right) \tag{3.47}$$

where M represents the number of the harmonic, and λ_u is the wavelength of the electron undulation. Note that on-axis, where $\theta = 0$, only odd harmonics are produced. For all of the x-ray experiments described in this thesis linearly polarised incident x-rays were used. X-rays from bending magnets, undulators, and wigglers are linearly polarised in the horizontal plane if the x-rays are incident on a point that is in the plane of orbit of the electrons (i.e. the plane of the synchrotron ring).

3.2.2 Inelastic X-ray Scattering

In an IXS experiment, the x-rays are scattered by the electrons of the atoms within the material. For this reason, the energy of the incident x-ray beam should be far from any absorption edges of the species in the sample. This is called non-resonant scattering.

The intensity of scattering, I, from a single electron is then given by,

$$\begin{aligned} I &= I_0\left(\frac{\mu_0}{4\pi}\right)^2\left(\frac{e^4}{m^2r^2}\right)\left(\frac{1+\cos^2(2\theta)}{2}\right) \\ &= I_0\frac{r_0^2}{r^2}\left(\frac{1+\cos^2(2\theta)}{2}\right) \end{aligned} \tag{3.48}$$

where m is the mass of an electron, 2θ is the angle between the incident and scattered beam, I_0 is the intensity of the incident beam and r_0 is the Thomson scattering length which is equal to 0.282×10^{-4} Å and r is the distance from the electron.

Now if we consider the scattering from a large number of electrons within an atom, we must take into consideration the electron density $\rho(r)$. Due to the larger spatial extension of the electronic cloud with respect to the nuclear dimension, a form factor which is Q-dependent, $f(Q)$, should be introduced in the scattering function and can be written as:

$$f_0(\mathbf{Q}) = \int \rho(\mathbf{r})e^{i\mathbf{Q}.\mathbf{r}}d^3\mathbf{r}. \tag{3.49}$$

where r is the radial co-ordinate from the atomic nucleus. If we assume a spherical charge density, then

$$f_0(Q) = \int 4\pi r^2\rho(r)\frac{\sin(Qr)}{Qr}dr. \tag{3.50}$$

where Q is the magnitude of the scattering wavevector Q. If we assume that $\rho(r)$ decays exponentially and isotropically with characteristic distance $a/2$ then the form factor is

$$f_0(Q) \approx \frac{1}{[1+(Qa/2)^2]} \tag{3.51}$$

The inelastic scattered differential cross-section in an IXS case could then be written as,

$$\frac{\partial^2\sigma}{\partial\Omega\partial E} = r_e^2 \frac{k_i}{k_f}(\mathbf{e}_i.\mathbf{e}_f)\left|f(Q)\right|^2 S(Q,\omega) \tag{3.52}$$

where r_e is the classical electron radius and $e_{i,f}$ indicate the incident/scattered polarization direction.

Similarly to equation (3.36), the conservation laws along with the x-rays energy relation $E_i = \hbar c k_i$, allow us to define the kinematic accessibility (or energy dynamic range) in a scattering experiment as follow:

$$(k/k_i)^2 = 1 + [1-(E/E_i)]^2 - 2\cos\theta[1-(E/E_i)] \tag{3.53}$$

as illustrated in Fig. 3.8.

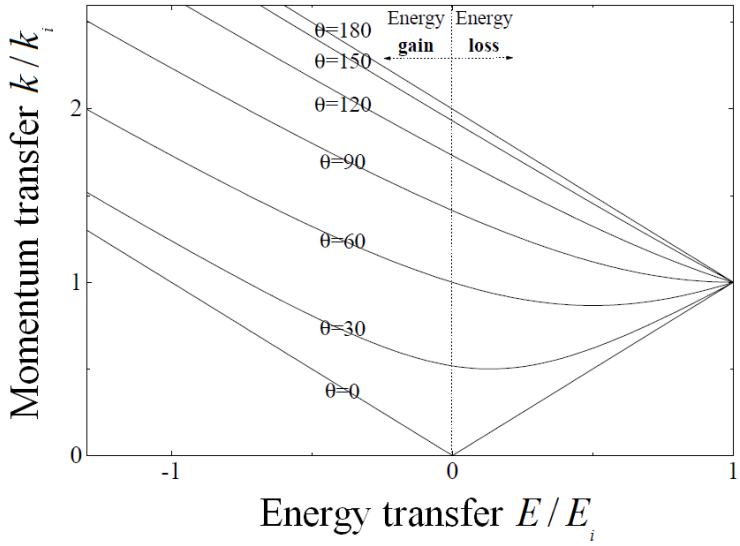

Figure 3.8 IXS allowed kinematic region for selected fixed scattering angles.

3.2.3 IXS Beamline ID16

All the IXS experiments reported in this work were performed at the ID16 beamline operating at ESRF. Fig. 3.9 illustrates a sketch of the beamline. A detailed description can be found in the literature [9]. Its working geometry is based on a triple axis neutron spectrometer: A very high resolution monochromator (1st axis), the sample (2nd axis) and the crystal analysers (3rd axis).

A high energy x-ray beam is extracted from the undulator with an energy range of [5-25.7] keV crosses a couple of Beryllium refractive lenses that collimate the beam before it hits the first monochromator.

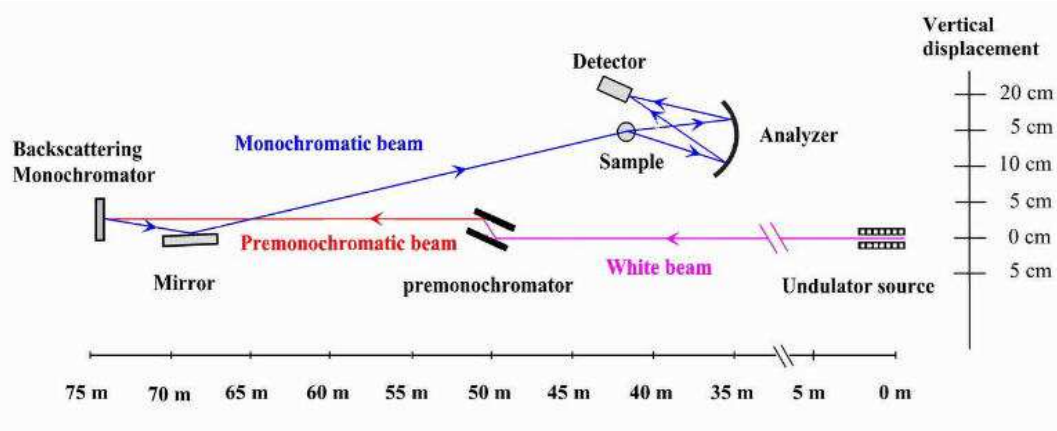

Figure 3.9 Sketch of the inelastic scattering beamline ID16 at the ESRF.

Termed as pre-monochromator, it consists of two Si (1,1,1) crystals with its main role to define the incident energy but also to dissipate most of the excess heat. The resulting beam then impinges onto a second high resolution single crystal monochromator made of pure silicon at a Bragg angle of 89.98° using the silicon (n,n,n) reflection orders. The energy scans are performed by varying the monochromator temperature and so for this reason, the temperature of the Si crystals is monitored with a milli-degree precision. For our experiments, the (12,12,12) reflexion that provides an incident energy of 23.725keV and a resolution of 0.83meV. The beam is then focused vertically and horizontally on the sample with the help of a multilayer mirror. After hitting the sample, the diffused beam is detected with a spherical crystal analyser that allows us to measure 7 Q-values simultaneously ranging from (1 to 6.6) nm^{-1}.

3.2.4 Data treatment

A representative data spectrum $I(Q,\omega)$ is shown in Fig. 3.10. The scattered intensity is proportional to the convolution of the dynamical structure factor $S(Q,\omega)$ with the resolution function $R(\omega)$, assuming that $R(\omega)$ has no Q dependence,

$$I(Q,\omega) \propto R(\omega) \otimes S(Q,\omega) \tag{3.54}$$

The spectra exhibit a triplet including a central Rayleigh peak and two lateral Brillouin peaks. For each value of Q, the calculated dynamic structure factor is multiplied by a Boltzmann term $S(Q,\omega) \rightarrow \exp(\hbar\omega / 2k_B T) S(Q,\omega)$ corresponding to the temperature used in the experiment, so as to satisfy the quantum mechanical detailed balancing condition (equation 3.28).

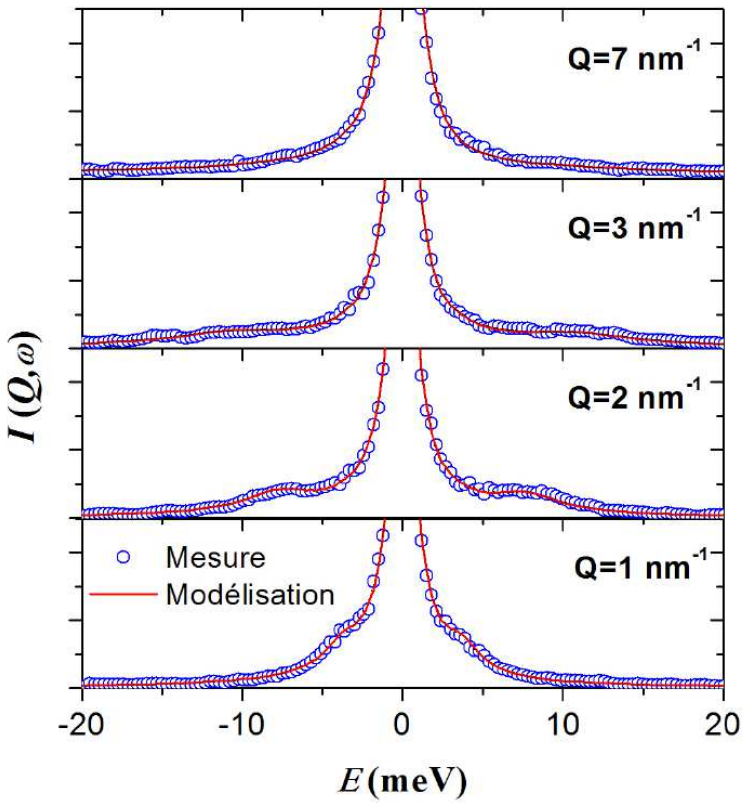

Figure 3.10 Selected IXS spectra for $MgAl_2O_4$ (circles) measured at 2500 K compared with the fit of the two-time-scale model [10].

Within the generalized Langevin equation formalism [11,12], it is possible to express the dynamical structure factor in terms of a complex memory function $M(Q,t)$ which is related to the interaction details. In particular, $S(Q,\omega)$ can be written in terms of the real (M') and imaginary (M'') part of the Fourier–Laplace transform of $M(Q,t)$ [13]:

$$S(Q,\omega) = \frac{S(Q)\pi^{-1}\omega_0^2(Q)\tilde{M}'(Q,\omega)}{\left[\omega^2 - \omega_0^2(Q) + \omega\tilde{M}''(Q,\omega)\right]^2 + \left[\omega\tilde{M}'(Q,\omega)\right]^2} \tag{3.55}$$

Where $\omega_0^2(Q) = k_B T Q^2 / mS(Q)$, m is the atomic mass and k_B is the Boltzmann constant. At low Q (hydrodynamic limit), Eq. (3.55) can be written as a sum of three Lorentzians

$$S(Q,\omega) = \frac{S(Q)}{\pi}\left\{ A_0 \frac{\Gamma(Q)}{\omega^2 + \Gamma^2(Q)} + A_S\left[\frac{\Gamma_S(Q)}{(\omega + \omega_S(Q))^2 + \Gamma_S^2(Q)} + \frac{\Gamma_S(Q)}{(\omega - \omega_S(Q))^2 + \Gamma_S^2(Q)} \right] \right\} \tag{3.56}$$

Where $\Gamma(Q)$ is the width of the central peak, $\Gamma_S(Q)$ and $\omega_S(Q)$ are the width and frequency of the Brillouin peaks and A_0 and A_S are normalizing coefficients. For a damped harmonic oscillator (DHO) model, the excitation frequencies $\Omega_S(Q)$ (renormalized by the damping term) have a linear Q dependence at small Q and its slope gives directly the longitudinal sound velocity [13]:

$$\Omega_S(Q) = \sqrt{\omega_S^2(Q) + \Gamma_S^2(Q)} = v_S Q \tag{3.57}$$

As shown previously [15], this hydrodynamic model is inappropriate to determine the longitudinal viscosity in the studied Q-range. We therefore applied a viscoelastic model. It is convenient to write $M(Q,t)$ as a sum of a longitudinal 'viscous' contribution $M_L(Q,t)$ and a term $M_{th}(Q,t)$ arising from thermal fluctuations,

$$M_{th}(Q,t) \approx (\gamma - 1)\omega_0^2 \exp[-\gamma D_T Q^2 t] \tag{3.58}$$

where D_T is the thermal diffusion coefficient and $\gamma = c_p / c_v$ is the heat capacity ratio. As observed with Al_2O_3 [14] and $MgAl_2O_3$ [10], γ is close to one and the thermal fluctuations corresponding to $M_{th}(Q,t)$ could be neglected. For the viscous part $M_L(Q,t)$, we adopted a model with two time scales: A simple Debye law (exponential decay) to describe the structural relaxation associated with an instantaneous microscopic process (delta function in time). The total memory function is thus defined by

$$M(Q,t) \approx M_L(Q,t) = \Delta^2(Q) e^{-t/\tau(Q)} + 2\Gamma_S(Q)\delta(t) \tag{3.59}$$

Where $\tau(Q)$ is the structural relaxation time and $\Delta(Q)$ the structural relaxation strength. With this model, the longitudinal viscosity η_l is calculated from

$$\Gamma_S(Q) + \Delta^2(Q)\tau(Q) = \frac{\eta_l}{\rho} Q^2 \tag{3.60}$$

Where ρ is the mass density.

REFERENCES

[1] J. Chadwick, Nature 129, 312 (1932).

[2] G.L. Squires; Introduction to the theory of thermal neutron scattering, Cambridge University Press (1978).

[3] S. W. Lovesey; Theory of neutron scattering from condensed matter, Clarendon Press (1986).

[4] H. E. Fischer, A. C. Barnes and P. S. Salmon, Rep. Prog. Phys. 69, 233 299 (2006).

[5] A. Meyer, S. Stüber, D. Holland-Moritz, O. Heinen and T. Unruh, Phys Rev. B. 77, 092201 (2008).

[6] www.ill.fr/YellowBook/IN6/

[7] J.Wuttke and F. Kargl. http://sourceforge.net/projects/frida/ (2007)

[8] J. Als-Nielsen and D. F. McMorrow; Elements of Modern X-Ray Physics, John Wiley and Sons Ltd, Chichester, West Sussex, (2001).

[9] C. Masciovecchio, U. Bergmann, M. Krisch, G. Ruocco, F. Sette et R. Verbeni, Nuclear Instruments & Methods in Physics research B 117, p. 339 (1996).

[10] I. Pozdnyakova, L. Hennet, J. Brun, D. Zanghi, S. Brassamin, V. Cristiglio, D. Price, F. Albergamo, A. Bytchkov, S. Jahn, and M. Saboungi, J. Chem. Phys. p.126, 114505 (2007).

[11] J.P. Boon and S. Yip, Molecular Hydrodynamics, McGraw-Hill International Book Company, New York (1980).

[12] T. Scopigno, G. Ruocco et F. Sette, Rev. Mod. Phys. p.77, 881 (2005).

[13] F. J. Bermejo, M. Alvarez, S. M. Bennington, R. Vallauri, Phys. Rev. E 51, 2250 (1995).

[14] H. Sinn, B. Glorieux, L. Hennet, A. Alatas, M. Hu, E. E. Alp, F.J. Bermejo, D. L. Price, M.L. Saboungi, Science 299, 2047 (2003).

Résumé du Chapitre 4

Ce chapitre présente une analyse détaillée des propriétés structurales déterminées sur les composés CAS ($(CaAl_2O_4)_{1-x}(SiO_2)_x$) pour cinq compositions: x = 0, 0.12, 0.19, 0.33 et 0.50 dans la phase liquide et pour la phase vitreuse. La préparation des échantillons et le dispositif expérimental y sont décrits dans un premier temps.

Nous avons mesuré le facteur de structure $S(Q)$ des CAS par diffraction de neutrons sur l'instrument D4C en utilisant une longueur d'ondes de 0.5 Å qui correspond à une gamme de vecteurs de diffusion Q de 0.3-23 $Å^{-1}$. Il faut noter que la contribution des 4 paires Si-O, Al-O, Ca-O et O-O constitue 90% de la fonction totale et donc que les fonctions $S(Q)$ et $g(r)$ représentent plutôt la structure autour de ces paires. L'évolution en fonction de la concentration en silice des facteurs de structure totaux et des fonctions de corrélation de paire associées est examinée.

Pour la phase vitreuse, les différences principales liées à l'augmentation la composition en silice se situent au niveau du premier pic de S(Q) qui devient plus intense et se décale linéairement vers les petites valeurs de Q. Ceci provient probablement d'une structuration plus importante améliorant l'ordre à moyenne distance. Il est ainsi possible de contrôler assez précisément la composition des verres sur ce joint en reportant la position du pic mesuré avec un verre de ce joint. Pour toutes les compositions des verres, le silicium est en site tétraédrique et l'aluminium est toujours trouvé avec une coordinence 4. Ces résultats sont en bon accord avec les résultats obtenus par RMN, technique beaucoup plus précise pour la détermination des coordinences et qui montrent que l'environnement de l'aluminium dans les verres est principalement tétraédrique avec quelques % de sites Al en coordinence 5. Pour le calcium, on n'a pas détecté une évolution évidente de l'environnement local. Dans tous les cas, on trouve une distance Ca-O de 1.35 Å et une coordinence autour de 5.5. Ceci est en bon accord avec les observations de Petkov et al. [11] qui a étudié diverses compositions sur ce joint et les résultats obtenus par C. Benmore et al. [12] sur le CA.

Pour la phase liquide, la forme globale des courbes $S(Q)$ est similaire à celle des verres. Nous avons observé cependant des différences importantes au niveau du 1er pic moins intense dans le liquide, ce qui est caractéristique d'une structure moins ordonnée à moyenne distance. Comparé aux verres, nous avons mis en évidence une augmentation de la coordinence de l'aluminium. Pour le CA, une coordinence moyenne de 4.54 a été trouvée. Cela est dû à une augmentation des proportions d'aluminium V et VI dans la structure. En particulier, ceci est en très bon accord avec la valeur CN^{Al-O} = 4.4 avec environ 38% d'Al^{V} et 4% d'Al^{VI} déterminée par Poe et al. [14]. Des observations similaires ont été faites sur l'ensemble des compositions CAS étudiées.

Nous avons rencontré une grande difficulté à déterminer l'environnement local autour de la paire Ca-O. Cela est principalement dû à son recouvrement par la contribution des corrélations O-O dans les $g(r)$ (pour les neutrons ainsi que pour les rayons X). Dans le but d'extraire l'environnement local autour du Ca, nous avons donc effectué une expérience de diffraction de neutron avec substitution isotopique (^{44}Ca) sur les phases liquide et vitreuse de la composition x=0 (CA). Les données très récentes sont en cours de traitement mais des résultats préliminaires obtenus sur le verre suggèrent un nombre de coordination de 5.5 qui est consistent avec la valeur présentée dans ce travail. Des mesures d'absorption de rayons X au seuil du calcium sont aussi planifiées dans les mois qui viennent et devraient donner des informations plus précises sur l'ordre local autour des atomes Ca pour toutes les compositions CAS.

CHAPTER 4

4 STRUCTURE

This chapter presents the results of the neutron diffraction study for the structural investigation. It is divided into two main sections. The first one describes the experimental details. The second section is divided into two parts where the results on the glass and liquid states are discussed separately. A conclusive discussion ends this chapter.

4.1 Experimental Details

Sample preparation

The 5 sample compositions $(CaAl_2O_4)_{1-x}$ $(SiO_2)_x$, denoted CA (x = 0), CAS 12.44 (x = 11.82), CAS 19.40 (x = 18.99), CAS 33.33 (x = 33) and CAS 50.25 (x = 50) were provided by D. Neuville from the IPGP (Institut de Physique du Globe de Paris). They were prepared from high purity crystalline $CaCO_3$, Al_2O_3 and SiO_2 powders. The appropriate quantities of powders were melted at 1900 K during 4 hours in a platinum crucible and then quenched to room temperature. The resulting materials were grinded and remelted and this process was repeated several times in order to ensure a good homogeneity of the glasses. The sample preparation is fully described in L. Cormier et al. [1]. The required weighted quantity was then levitated on an air gas flow and melted by laser heating. The melting points, T_m, of CA, CAS 12.44, CAS 19.40 and CAS 33.33 are 1878 K, 1893 K, 1863 K and 1823 K respectively. On cooling, by switching off the laser power, solid spherical samples of 4 mm (for the glass measurements) and 2.7 mm (for the high temperature liquid measurements) diameters were formed.

D4C diffractometer

The experiment was carried out at the D4c instrument at the Institut Laue Langevin (ILL) in Grenoble (France). A concise description of this neutron diffractometer can be found in Fischer et al [2]. This is a two-axis instrument optimized for structural investigations of liquids and amorphous materials. It has basically three main components: the monochromator, the sample chamber and the detectors (See Fig. 4.1). In this study, we used Cu[220] monochromator

giving a working wavelengths of 0.5 Å. The actual values of wavelength and zero-angle shift are determined by means of a Rietveld refinement of a standard diffractogram (Ni powder).

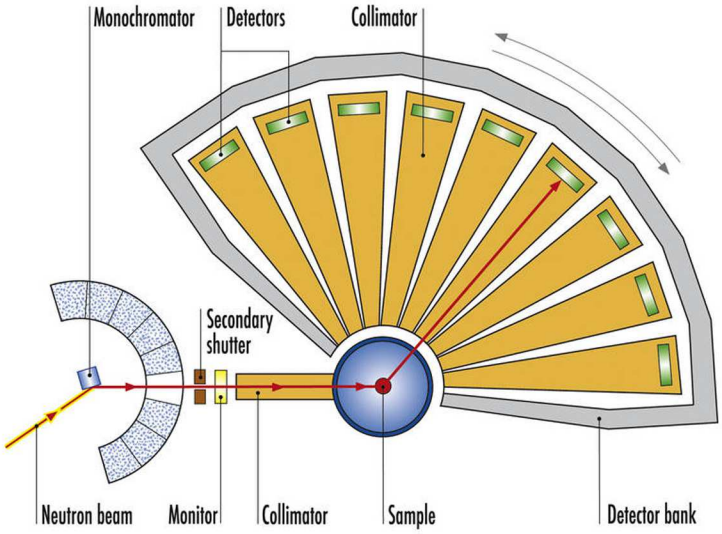

Figure 4.1 Schematic representation of the D4C neutron diffractometer at the ILL.

The vacuum chamber consists of a cylinder 550 mm high and 460 mm in diameter in which the high-temperature device described above is enclosed. The wide-angle detector is scanned over a 1.3–140 ° angular range corresponding to a Q range of 0.3–24 $Å^{-1}$ with an average resolution $\Delta Q/Q = 2.5 \times 10^{-2}$.

Experimental configuration and procedure

For these experiments, we used the aerodynamic levitation setup specifically designed for neutron diffraction at D4c and is well described by Hennet et al. [3]. Fig. 4.2 is a schematic view of the levitation setup integrated into the D4c sample chamber.

During experiments, the chamber is initially pumped down to low pressure (10^{-4} mbar) and then filled with the levitation gas up to atmospheric pressure. This ensures a reproducible atmosphere around the sample and is necessary for removing the background correctly during the data analysis. The entire vacuum chamber is cooled with circulating cooling water. An assembly of vertical and horizontal isotopic $^{10}B_4C$ slits produced a rectangular beam on the sample. The vertical slits were placed very close to the nozzle and adjusted in order to mask the nozzle from the incident beam, thus avoiding any significant scattering from it.

Finally, to extract the scattering cross section from the scattered intensity from the sample, we first subtract the scattering from the entire sample environment and from the absorption contribution and we normalize to a vanadium standard reference. This means that in addition to

the measurement of the sample scattering, it is necessary to measure the diffracted intensity from the levitator alone, from a standard vanadium sample and from the empty diffractometer. Since the nozzle was completely hidden by the bottom part of the slits, the relatively low background intensity was mostly due to scattering from the gas in the chamber.

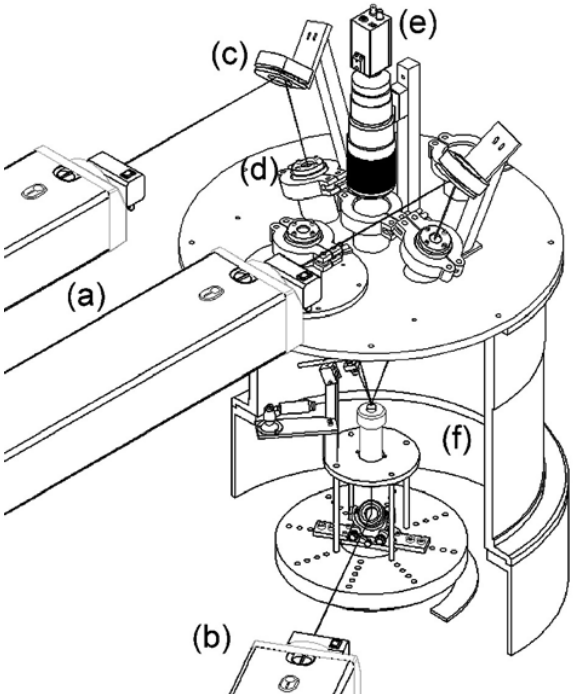

Figure 4.2 Schematic view of the experimental arrangement: laser heads ((a), (b)), spherical mirrors (c), NaCl windows, (d) video camera (e), and levitation device (f).

4.2 Results and Discussion

The total static structure $S(Q)$ factor of $(CaAl_2O_4)_{1-x}$ $(SiO_2)_x$ systems as measured by neutron diffraction can be written as:

$$S(Q)-1=\frac{1}{\left(\sum_{\alpha}c_{\alpha}b_{\alpha}\right)^2}\sum_{\alpha=1}^{n}\sum_{\beta=1}^{n}c_{\alpha}c_{\beta}b_{\alpha}b_{\beta}[S_{\alpha\beta}(Q)-1] \qquad (4.1)$$

where we are taking a weighted average of the $S_{\alpha\beta}(Q)$. Here n=4 (n=3 in the case of CA) denotes the number of chemical species α or β, (c_{α},c_{β}) are the atomic concentration of elements (α,β) and $S_{\alpha\beta}(Q)$ is the corresponding Faber-Ziman partial structure factor [4]. We can then apply the equation for a monoatomic system such as:

$$g(r)-1=\frac{1}{2\pi^2 r\rho_0}\int_0^{\infty}[S(Q)-1]Q\sin(Qr)\mathrm{d}Q \tag{4.2}$$

and the total pair distribution function $g(r)$, which corresponds to the real space information, is then given by:

$$g(r)-1=\frac{1}{\bar{b}^2}\sum_{\alpha=1}^{n}\sum_{\beta=1}^{n}c_\alpha c_\beta b_\alpha b_\beta[g_{\alpha\beta}(r)-1] \tag{4.3}$$

Where $\bar{b}^2$ is equal to $\left(\sum_\alpha c_\alpha b_\alpha\right)^2$, b_α is the coherent scattering length which for X-rays, is a function of Q (atomic form factor) and c_α, c_β are the atomic concentration of elements α and β.

For the natural isotopic abundance, the coherent neutron scattering lengths for the chemical species in our samples are b_O=5.805(4) fm, b_{Al}=3.449(5) fm, b_{Ca}=4.70(2) fm and b_{Si}=4.15071(22) fm [5]. In practice, in order to obtain the coordination number, one uses the total correlation function defined as:

$$T(r)=4\pi\rho_0 r g(r)=\frac{\mathrm{RDF}(r)}{r} \tag{4.4}$$

This is due to the fact that the peaks in $T(r)$ are symmetrically broadened by a finite Q_{max} and thus allows an easier fitting procedure of gaussians. The mean coordination number $CN^{\alpha\text{-}\beta}$, which actually gives the average number of β atoms in a spherical coordination shell of radius $r_1 \le r \le r_2$ centered on an α atom, can then be obtained by integrating over the corresponding peak in the $g_{\alpha\beta}(r)$ as follows:

$$\mathrm{CN}^{\alpha-\beta}=\bar{r}\int_{r_1}^{r_2}T(r)\mathrm{d}r=4\pi\rho_0 c_\beta\int_{r_1}^{r_2}g_{\alpha\beta}(r)r^2\mathrm{d}r \tag{4.5}$$

Table 5. below gives the neutron weighting factors for each $S_{\alpha\beta}(Q)$ partial structure factor. We see that the first 4 atomic pairs (Si-O, Al-O, Ca-O and O-O) constitute up to 90% of the total scattering function. For this reason, almost all the structure information provided by the static structure factors $S(Q)$ measured by neutron diffraction and their corresponding pair-distribution functions $g(r)$ is about these atomic pairs. These will mainly be the interesting contributions to be discussed. The other contributions occur at almost the same position and therefore are somehow difficult to interpret.

Atomic pairs	CA	CAS 12.44	CAS 19.40	CAS 33.33	CAS 50.25
Si-O	--	0.0384	0.0626	0.1130	0.1752
Al-O	0.2643	0.2384	0.2220	0.1879	0.1456
Ca-O	0.1801	0.1624	0.1513	0.1280	0.0992
O-O	0.4446	0.4548	0.4611	0.4741	0.4900
Ca-Ca	0.0182	0.0145	0.0124	0.0086	0.0050
Ca-Al	0.0535	0.0426	0.0364	0.0254	0.0147
Ca-Si	--	0.0069	0.0103	0.0153	0.0177
Al-Al	0.0393	0.0312	0.0267	0.0186	0.0108
Al-Si	--	0.0101	0.0151	0.0224	0.0260
Si-Si	--	0.0008	0.0021	0.0067	0.0157

Table 5. Normalized neutron weighting factors for the Faber-Ziman partial structure factors in the $(CaAl_2O_4)_{1-x}$ $(SiO_2)_x$ systems. Note that the O-O pair correlations contribute more than any other atomic pair at all compositions.

4.2.1 Glasses at Room Temperature

Structure factors

The total structure factors $S(Q)$ for our $(CaAl_2O_4)_{1-x}$ $(SiO_2)_x$ glasses at room temperature as measured by neutron diffraction are plotted in Fig. 4.3. We see that with increasing SiO_2 concentration, the main differences concern the first peak in $S(Q)$ which shifts towards lower Q values with a higher intensity. This shows that the structure is more ordered when the silica content is increased. This has been also observed previously By D. Neuville et al. using XANES experiments at the Ca absorption edge [13].

Fig. 4.4 reports the position of the first peak in $S(Q)$ as a function of SiO_2 content. The first peak position decreases from $Q = 2.08$ Å^{-1} for the CA (no SiO_2 content) to $Q = 1.82$ Å^{-1} for the CAS 50.25. We report as well the FSDP for vitreous silica measured by neutron diffraction from Ref. [6]. Obviously, the dependency of the first peak position on the silica content expresses a linear behavior. This perfect linear behavior thus allows one to define precisely the CAS glass composition along the join R=1 by measuring the position of the first peak in the static structure factor.

Pair distribution functions

Fig. 4.5 shows the total pair distribution functions $g(r)$ for all the compositions studied. For the calculations, we used the glass densities determined by Neuville et al. [7]. For the CA, the first peak arises purely from the contribution of the nearest neighbor Al-O correlations whereas for all the CAS, the first peak corresponds to an overlapped contribution from both the Al-O and the Si-O nearest neighbor pairs. The evolution of the first peak position in $g(r)$ as a function of the different CAS compositions is shown in Fig. 4.6. We can see that the first peak

position moves to lower *r* values upon increasing SiO_2 content. The first peak decreases from a value of $r = 1.76$ Å for CA to a value of $r = 1.66$ Å for the CAS 50.25.

For comparison purposes, we report on the same graph the value of the first peak position in $g(r)$ of pure Silica found at 1.62 Å by A. C. Wright [6]. By inspecting the graph, we can see that the evolution of the first peak position maintains a linear behavior until a certain threshold appeared to be at 50% of SiO_2 concentration where it no more shows a linear trend but continues to decrease smoothly to the value of $r = 1.62$ Å for pure SiO_2.
This actually means that, after this threshold value, the local environment probed tends to be more identical to that of pure silica. XANES experiment performed by Neuville et al. at the O absorption edge [8] shows that the oxygen environment for high SiO_2 concentration CAS is similar to pure SiO_2, an observation which uphold our suggestion.

The second peak in the $g(r)$ at $r \approx 2.3$ Å corresponds to the Ca-O correlations. This peak is well pronounced in the CA, but then undergoes a progressive broadening with increasing SiO_2. This is firstly due to the decrease of the Ca-O contribution from 18% to 9% (for CA and CAS 50.25 respectively (see Table 5), and secondly to the increase in the O-O correlations that actually corresponds to those constituting the SiO_4 tetrahedra which give rise to a peak at $r = 2.65$ Å that is more visible in the highest (50%) SiO_2 composition measured. This value is very close the O-O distance of 2.66 Å determined by A. C. Wright [6] in vitreous SiO_2.

For $CaAl_2O_4$ (CA), the peak at $r = 2.88$ Å in the $g(r)$ arises mostly from the O-O correlations in the AlO_4 tetrahedra. Its intensity decreases progressively due to a decrease in the number of these AlO_4 tetrahedra upon adding SiO_2. The next peak at $r = 3.6$ Å is weakly probed and corresponds to the cation-cation correlations, and its intensity is almost constant for all the compositions. The O-O correlations from the CaO polyhedra should contribute at a distance of about 3.2 Å.

Finally, the barely resolved peaks at $r \approx 4.2$ Å and $r \approx 5.2$ Å correspond to correlations with the second oxygen neighbors.

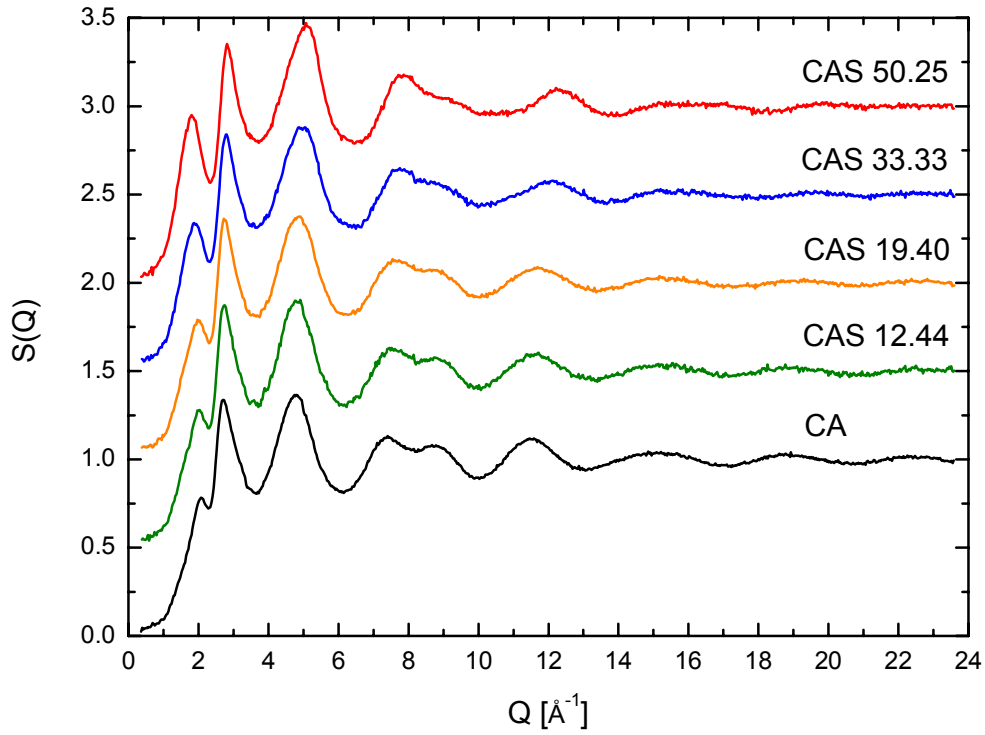

Figure 4.3 The total structure factors $S(Q)$ for the $(CaAl_2O_4)_{1-x}$ $(SiO_2)_x$ glasses at room temperature obtained from neutron diffraction. For clarity, the CAS compositions have been displaced by 0.5.

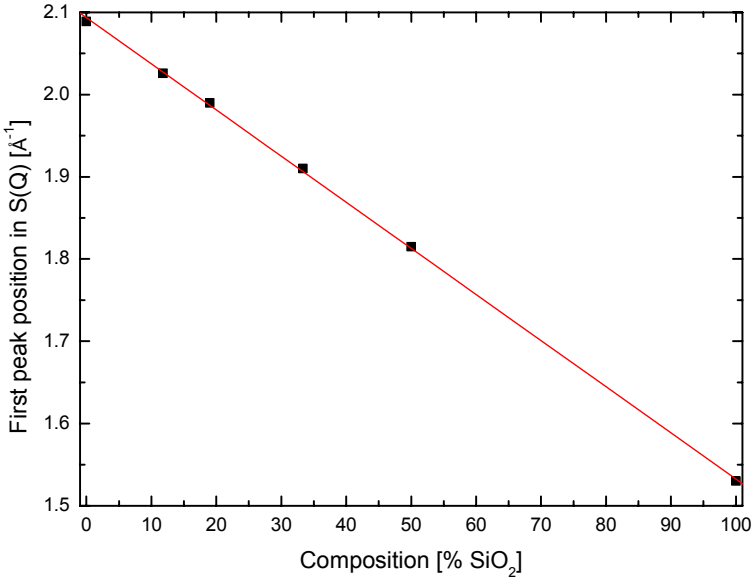

Figure 4.4 Evolution of the first peak in the total structure factor $S(Q)$ of $(CaAl_2O_4)_{1-x}$ $(SiO_2)_x$ glasses at room temperature as a function of SiO_2 concentration. The value corresponding to pure silica (100% SiO_2) is taken from Ref. [6].

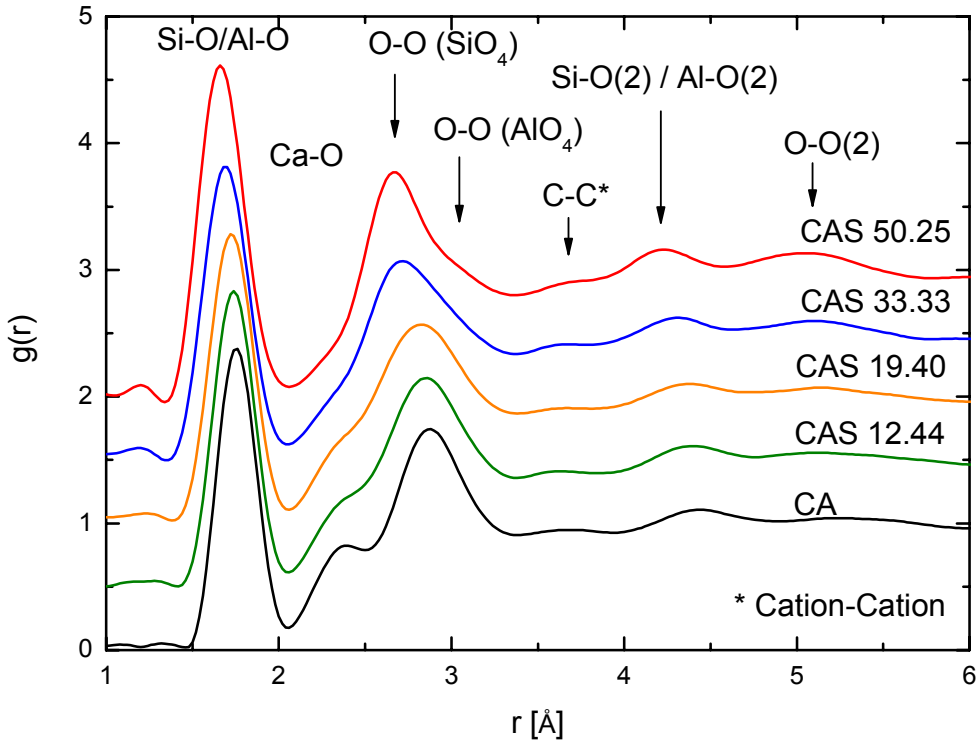

Figure 4.5 The total pair distribution function $g(r)$ for the $(CaAl_2O_4)_{1-x}$ $(SiO_2)_x$ glasses at room temperature as obtained by Fourier transforming the corresponding total structure factors. For clarity, the CAS compositions have been displaced by 0.5.

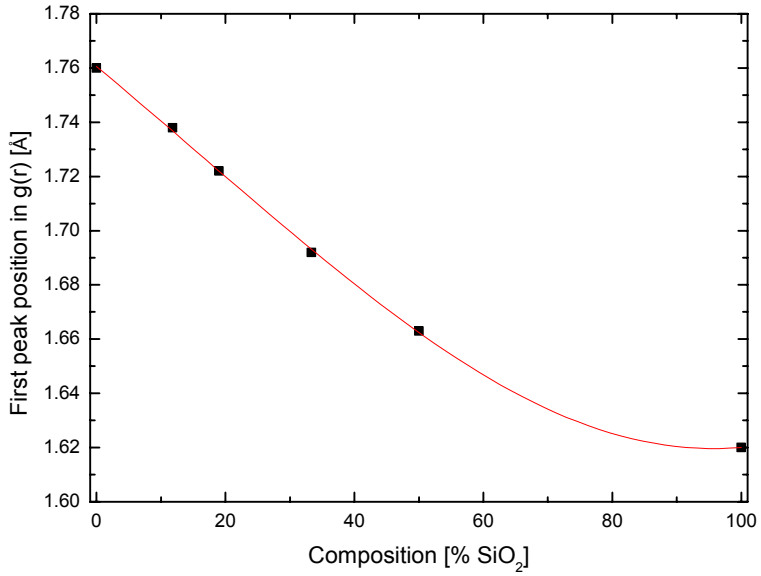

Figure 4.6 Evolution of the first peak in the total pair distribution function $g(r)$ of $(CaAl_2O_4)_{1-x}$ $(SiO_2)_x$ glasses at room temperature as a function of SiO_2 concentration. The value corresponding to pure silica (100% SiO_2) is taken from Ref. [6].

Coordination numbers

The overlapping of the Si-O and Al-O correlations under the first peak in $g(r)$ introduces some uncertainty in the calculation of their distances and coordination numbers. Before fitting the first peak with two Gaussians, one can proceed first in a qualitative way to estimate their different contributions, which is to consider the area *"A"* under the first peak in $T(r)$ as a linear combination of both coordination numbers $CN^{Si\text{-}O}$ and $CN^{Al\text{-}O}$ as follows:

$$A.r_1 = \alpha^{Si\text{-}O} CN^{Si\text{-}O} + \alpha^{Al\text{-}O} CN^{Al\text{-}O} \tag{4.6}$$

where $\alpha^{ij} = b_i b_j / \bar{b}^2$ and r_1 is the position of the first peak in $T(r)$.

For $CaAl_2O_4$ (CA), where there is no silica content, integration over the Al-O peak directly gives the corresponding $CN^{Al\text{-}O}$. However, for the CAS, we make the assumption that the Si is always in a tetrahedral geometry (fourfold coordination) and thus we assume a constant $CN^{Si\text{-}O}$ = 4. By applying this model, we get the Al-O coordination numbers $CN^{Al\text{-}O}$ that are listed in Table 6 for all the compositions.

Composition (Glass)	A.r_1	$\alpha^{Si\text{-}O}$	$CN^{Si\text{-}O}$	$\alpha^{Al\text{-}O}$	$CN^{Al\text{-}O}$
CA	1.8880	0	4	0.4625	4.07
CAS 12.44	1.9543	0.0660	4	0.4102	4.12
CAS 19.40	1.9808	0.1066	4	0.3780	4.11
CAS 33.33	2.0332	0.1883	4	0.3131	4.09
CAS 50.25	2.1143	0.2847	4	0.2366	4.12

Table 6. The Al-O coordination number for $(CaAl_2O_4)_{1-x}$ $(SiO_2)_x$ in the glassy state as calculated by assuming a weighted sum of the overlapped Si-O and Al-O contributions under the first peak in $g(r)$.

The Al-O coordination numbers obtained from the linear combination model are in good agreement with the results obtained by RMN [9,10] and confirm the tetrahedral coordination of O around Al.

In the second step, we model the $T(r)$ curves using a sum of 8 Gaussians, each representing a particular atom pair, where we also distinguish the different oxygen sites: Si-O, Al-O, Ca-O, O-O (in SiO_2), O-O (in AlO_4), O-O (in CaO_6), cation-cation and a last Gaussian to terminate the fit series.

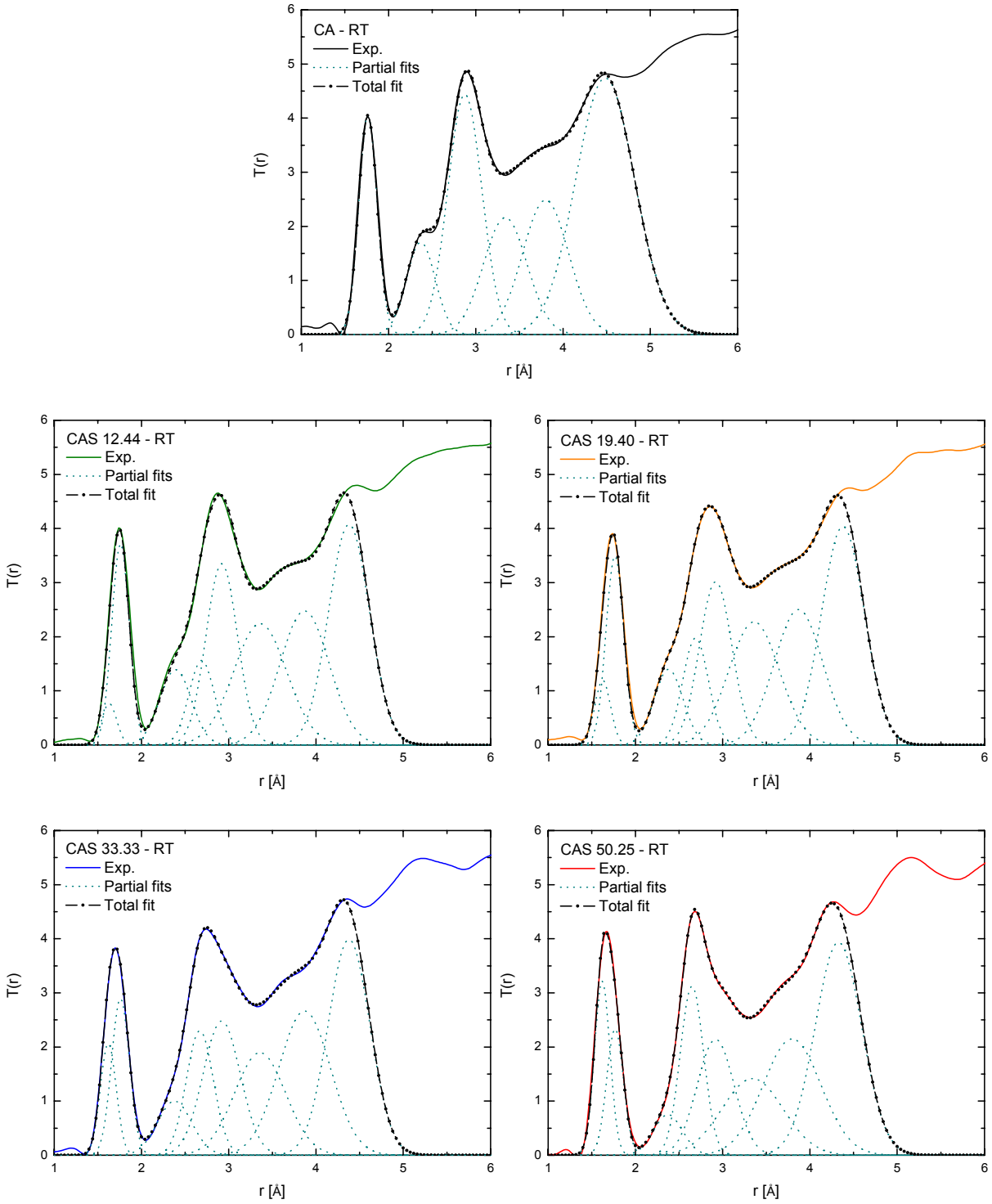

Figure 4.7 The total correlation functions for the $(CaAl_2O_4)_{1-x}$ $(SiO_2)_x$ glasses at room temperature. The dotted lines are the gaussian partial fits for the coordination numbers calculation.

In this way, by integrating over the relevant peak in the total correlation function (see Fig. 4.7), we get the coordination numbers $CN^{Si\text{-}O}$, $CN^{Al\text{-}O}$ and $CN^{Ca\text{-}O}$. The coordination numbers for the O-O pair in SiO_4 and AlO_4 tetrahedra are difficult to obtain because, in addition to their overlapped contribution under the peak at $r \approx 3$ Å, their distances are not precisely defined. When the Si-O and Al-O contributions under the first peak are now fitted with 2 gaussians, we get distances around $r^{Si\text{-}O} \approx 1.62$ Å and $r^{Al\text{-}O} \approx 1.76$ Å. These values are very close to the sum of the corresponding ionic radii and show a very good agreement with published data obtained for some of our compositions [1]. These values were then fixed for all the compositions during the fitting procedure. We report in Table 7 the obtained coordination numbers and the first five distances in $g(r)$ together with the first peak Q_1 in $S(Q)$.

Composition (Glass)	Q_1 [Å^{-1}]	$r^{Si\text{-}O}$ [Å]	$r^{Al\text{-}O}$ [Å]	$r^{Ca\text{-}O}$ [Å]	$r^{O-O}_{SiO_4}$ [Å]	$r^{O-O}_{AlO_4}$ [Å]	$CN^{Si\text{-}O}$	$CN^{Al\text{-}O}$	$CN^{Ca\text{-}O}$
CA	2.09	--	1.76	2.36		2.86	--	4.11	5.43
CAS 12.44	2.03	1.62	1.76	2.38	2.64	2.90	4.02	4.16	5.38
CAS 19.40	1.99	1.62	1.76	2.36	2.66	2.90	4.08	4.14	5.38
CAS 33.33	1.91	1.62	1.76	2.36	2.68	2.90	4.05	4.09	5.51
CAS 50.25	1.82	1.62	1.76	2.36	2.68	2.90	4.04	4.11	5.58

Table 7. The leading peak position Q_1 in $S(Q)$ and the first five peak positions $r^{Si\text{-}O}$, $r^{Al\text{-}O}$, $r^{Ca\text{-}O}$, $r^{O-O}_{SiO_4}$ and $r^{O-O}_{AlO_4}$ in $g(r)$ with the coordination numbers $CN^{Si\text{-}O}$, $CN^{Al\text{-}O}$, $CN^{Ca\text{-}O}$ as measured by neutron diffraction for the $(CaAl_2O_4)_{1-x}$ $(SiO_2)_x$ glasses at RT.

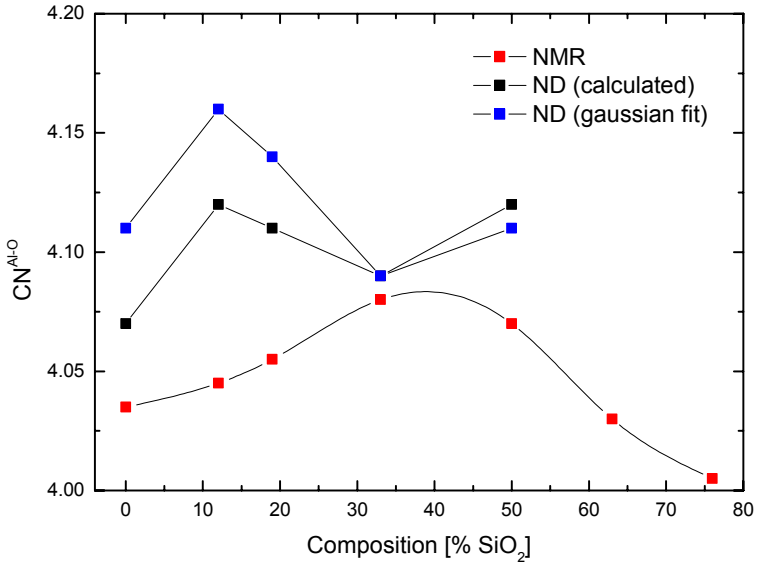

Figure 4.8 Comparison between the Al-O coordination number as obtained from NMR and ND.

Focusing first on the Si and Al environment (Table 7), we notice that, as observed from the weighted sum approximation mentioned earlier; they remain in tetrahedral sites for all the studied compositions. The local environment of these glasses has been extensively studied in details by means of various spectroscopic techniques (RMN, Raman and XANES) [10,13]. We report in Fig. 4.8, our calculated (weighted sum approximation) and experimental (gaussian fitted) Al-O coordination number as obtained from neutron diffraction together with the NMR data obtained by Neuville et Al. [9,10]. We see that although our neutron diffraction study gives good approximation of the coordination number, the NMR technique have a much better precision in quantifying the coordination number around the aluminium in AlOx tetrahedra. Actually, NMR experiments showed the existence of few % of fivefold coordinated aluminium AlO_5 species in the structure of these $(CaAl_2O_4)_{1-x}$ $(SiO_2)_x$ glasses which presents a maximum of about 8% at approx. 40% of SiO_2 (x=0.4) [9].

Now by inspecting the Ca-O distance and coordination number, we see that the calcium local environment doesn't present significant evolution with the increase of SiO_2. Values of $r^{Ca\text{-}O} \approx 2.35$ Å and $CN^{Ca\text{-}O} \approx 5.5$ were found almost constant for all the compositions. These values are in good agreement with those observed by Petkov et al. [11] who studied different compositions along the join R=1 and as well with the results obtained by C. Benmore on the CA composition [12]. XANES measurements (Neuville et al [13]) performed at the Ca absorption edge show that the position of the pre-edge peak doesn't change with the silica content, supporting a constant Ca-O coordination number. The observed decrease of its intensity suggests that Ca sites become more "ordered" upon increasing SiO_2. Nevertheless, the observed modification of the Ca absorption edges suggests that the electronic environment around the calcium atom is modified. This might be connected to the structural changes observed around the O-O bonds in the $g(r)$ that should influence the connectivity of Ca atoms.

4.2.2 High temperature measurements

The first four $(CaAl_2O_4)_{1-x}$ $(SiO_2)_x$ compositions were measured in the liquid state at temperatures close to their respective melting points. The measurement acquisition time was the same as for their glassy state except that of liquid CA which was measured for a longer duration. Here should be recalled that the sample's diameter used for the high temperature measurements was a factor of 1.7 less than that used for the glass at RT.

Fig. 4.9 shows the obtained static structure factors for the different compositions. Compared to the glass spectra, the data for the liquid are much noiser, notably due to the smaller sample volume exposed to the beam. We can observe as well the better statistics of liquid CA compared to the other liquid CAS.

The $S(Q)$ spectra obtained for the liquid state is similar to the ones for the glass. The FSDP stayed almost at the same position; however, the major difference is that its intensity is much lower than that for the glass. This is a characteristic signature of a less ordered system. This decrease in the structural order is as well observed in the duplet peak around $Q \approx 8$ Å^{-1}.

This increase in the structural disordered in the liquid is as well detected in the pair distribution functions presented in Fig. 4.10. Actually, the broader peaks in the $g(r)$ at about 3 Å result in the loss of structural information for the Ca-O correlation which was much pronounced for the glass. The difficulty of solving the Ca-O correlation comes from the fact that this peak is mostly composed of O-O bonds (45 to 50% of the total $g(r)$).

As a first step to solve the Si-O and Al-O correlations under the first peak, we proceed as we did for the glass and assume a weighted sum of both correlations while always fixing the coordination number of Si-O to 4. The obtained results are listed in Table 8.

Composition (Liquid)	A.r_1	$\alpha^{Si\text{-}O}$	$CN^{Si\text{-}O}$	$\alpha^{Al\text{-}O}$	$CN^{Al\text{-}O}$
CA	2.0990	0	4	0.4625	4.54
CAS 12.44	2.1096	0.0660	4	0.4102	4.50
CAS 19.40	2.1842	0.1066	4	0.3780	4.65
CAS 33.33	2.2145	0.1883	4	0.3131	4.67

Table 8. The Al-O coordination number for $(CaAl_2O_4)_{1-x}$ $(SiO_2)_x$ in the liquid state as calculated by assuming a weighted sum of the overlapped Si-O and Al-O contributions under the first peak in $g(r)$.

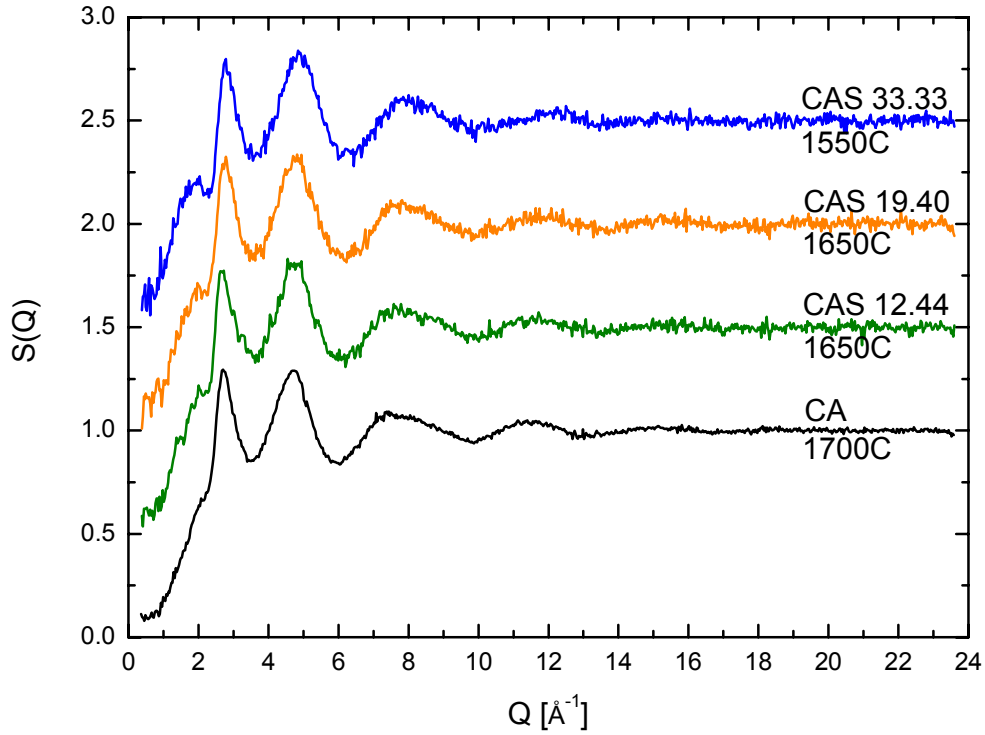

Figure 4.9 The total structure factors $S(Q)$ for the $(CaAl_2O_4)_{1-x}$ $(SiO_2)_x$ liquids obtained from neutron diffraction. For clarity, the CAS compositions have been displaced by 0.5.

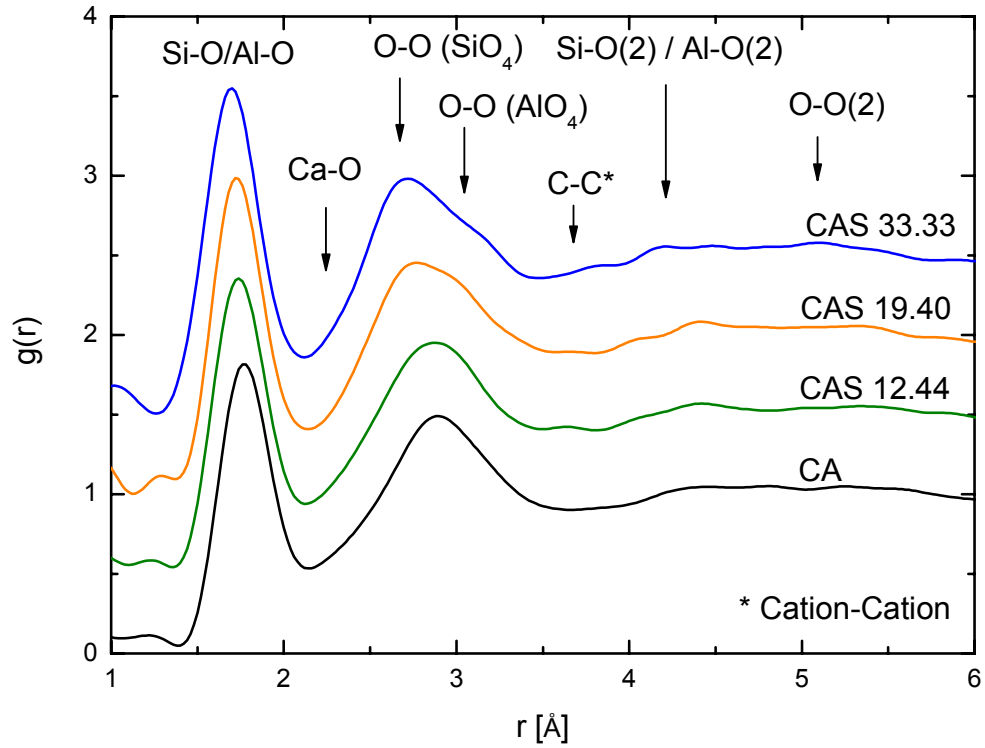

Figure 4.10 The total pair distribution function $g(r)$ for the $(CaAl_2O_4)_{1-x}$ $(SiO_2)_x$ liquids as obtained by Fourier transforming the corresponding total structure factors. For clarity, the CAS compositions have been displaced by 0.5.

As it can be observed, we obtain higher coordination numbers as compared to the glass. This is due to the fact that we have an increase in the fivefold (AlO_5) and sixfold (AlO_6) aluminium species in the structure. Published data for CA resulting from a NMR study indicates a mean coordination number of $CN^{Ca\text{-}O} \approx 4.4$ with 38.3% of AlO_5 and 3.7% of AlO_6 [14]. We can see that our neutron diffraction data are then in good agreement. We found no published data for the other CAS compositions; however, the above obtained coordination numbers allow us to speculate a similar increase with approx. the same proportion of AlO_5 in the CAS structure.

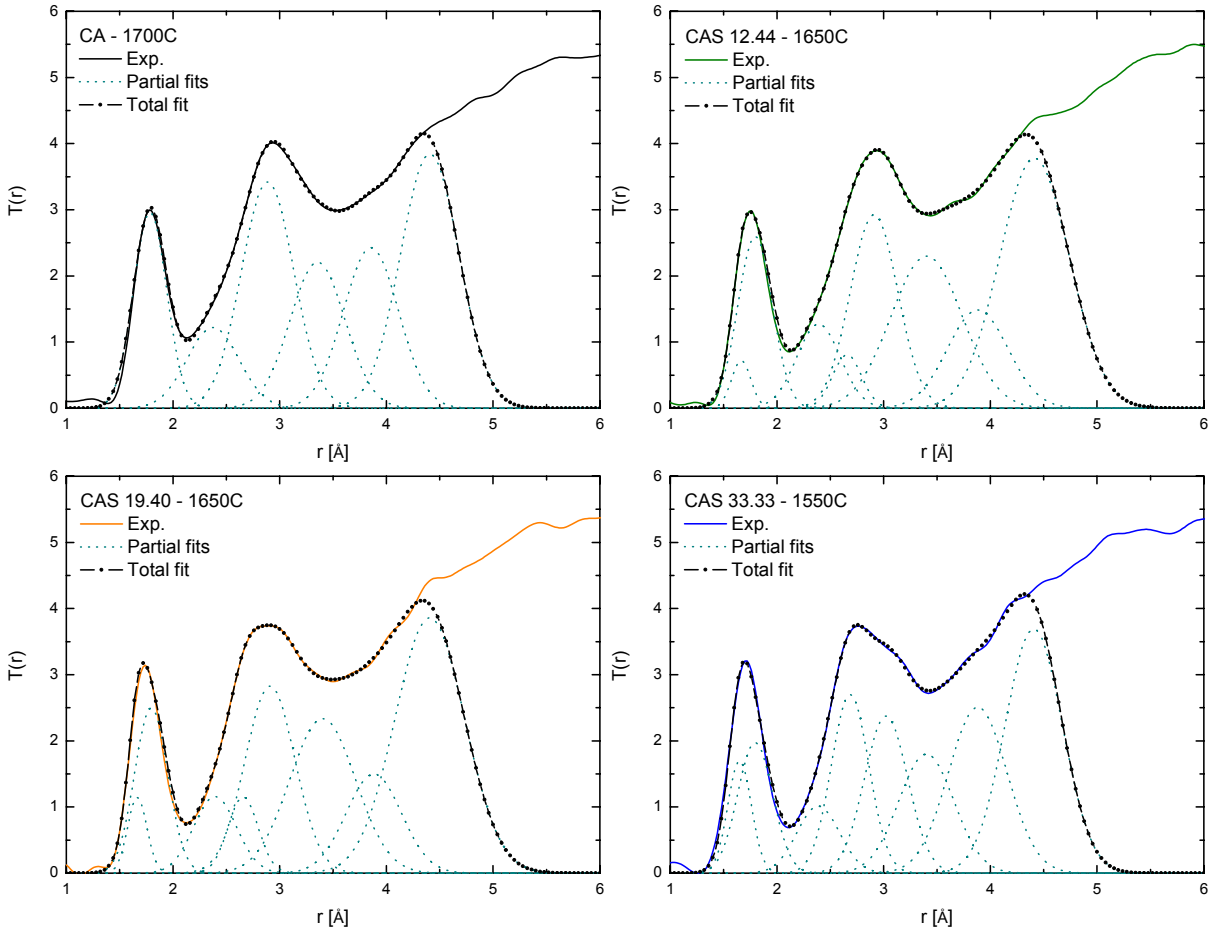

Figure 4.11 The total correlation functions for $(CaAl_2O_4)_{1\text{-}x}$ $(SiO_2)_x$ liquids at high temperature. The dotted lines are the gaussian partial fits for the coordination numbers calculation.

The $T(r)$ for the different compositions was then fitted with Gaussians (same procedure as for the glass) as shown in Fig. 4.11. For all the calculations, we used the densities determined by P. Courtial et al [15]. All the structural parameters obtained are listed in Table 9 below.

Composition (Liquid)	Q_1 [Å^{-1}]	r^{Si-O} [Å]	r^{Al-O} [Å]	r^{Ca-O} [Å]	$r_{SiO_4}^{O-O}$ [Å]	$r_{AlO_4}^{O-O}$ [Å]	CN^{Si-O}	CN^{Al-O}	CN^{Ca-O}
CA	2.09	--	1.79	2.36	--	2.86	--	4.54	5.53
CAS 12.44	2.03	1.66	1.79	2.38	2.66	2.90	4.12	4.57	5.58
CAS 19.40	1.99	1.66	1.79	2.38	2.64	2.90	4.05	4.62	5.41
CAS 33.33	1.91	1.65	1.79	2.38	2.68	3.00	4.05	4.64	5.66

Table 9. The leading peak position Q_1 in $S(Q)$ and the first five peak positions r^{Si-O}, r^{Al-O}, r^{Ca-O}, $r_{SiO_4}^{O-O}$ and $r_{AlO_4}^{O-O}$ in $g(r)$ with the coordination numbers CN^{Si-O}, CN^{Al-O}, CN^{Ca-O} as measured by neutron diffraction for the $(CaAl_2O_4)_{1-x}$ $(SiO_2)_x$ liquid at high temperatures.

We can see that for Al-O, the coordination numbers obtained from the fitting (Table 9) are very close to the one obtained from the weighted sum approximation (Table 8). As it can be seen from Fig. 4.11, the Ca-O correlations experience an overlap from the $g_{O-O}(r)$ partial pair distribution function which actually leads to errors of ± 0.05 Å and ± 1 in the Ca-O distances and coordination numbers respectively. In fact, the O-O correlations are difficult to model because the fits become highly dependent on all the other correlations at high distances values. This is what actually increases the uncertainty in solving the Ca-O correlation.

Information from X-rays

Recently, we performed X-ray diffraction experiments (on the ID11 high energy diffraction beamline at the ESRF) on the same compositions for both the glass and the liquid state for which the data treatment is still in progress. In fact, the X-ray diffraction allows a better detection of the Ca-O peak since the atomic number for Ca (Z=20) is much greater than that for O (Z=8) and so its contribution to the diffracted intensity is higher. Here, we only present the preliminary results for the glass compositions. Fig. 4.12 and 4.13 show the obtained static structure factors and total pair distribution functions obtained by the X-ray scattering denoted $S^X(Q)$ and $g^X(r)$ respectively. By inspecting the $g^X(r)$, we can see that the Ca-O peak (which is now more visible) do not experience significant changes upon adding SiO_2, which in fact explains why we get almost a constant CN^{Ca-O} from our neutron diffraction experiment. However, its corresponding peak is still overlapped by the contribution of the O-O pair from the SiO_4 tetrahedra which makes it more difficult to resolve.

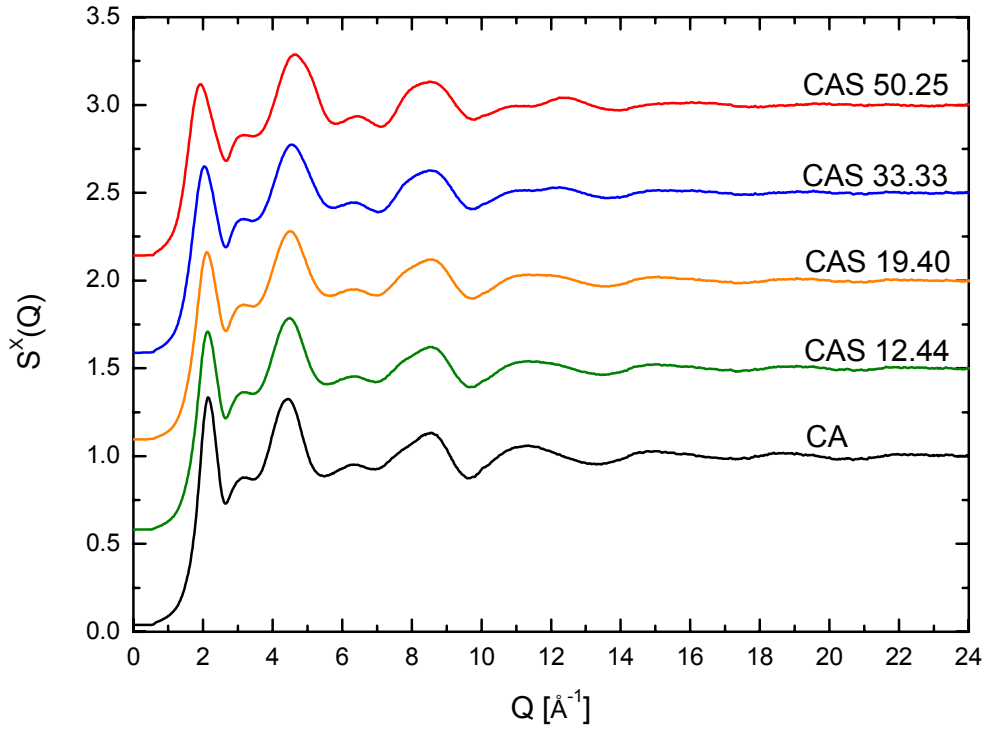

Figure 4.12 The total structure factor $S^X(Q)$ for the $(CaAl_2O_4)_{1-x}$ $(SiO_2)_x$ glasses at room temperature obtained from X-ray diffraction. For clarity, the CAS compositions have been displaced by 0.5.

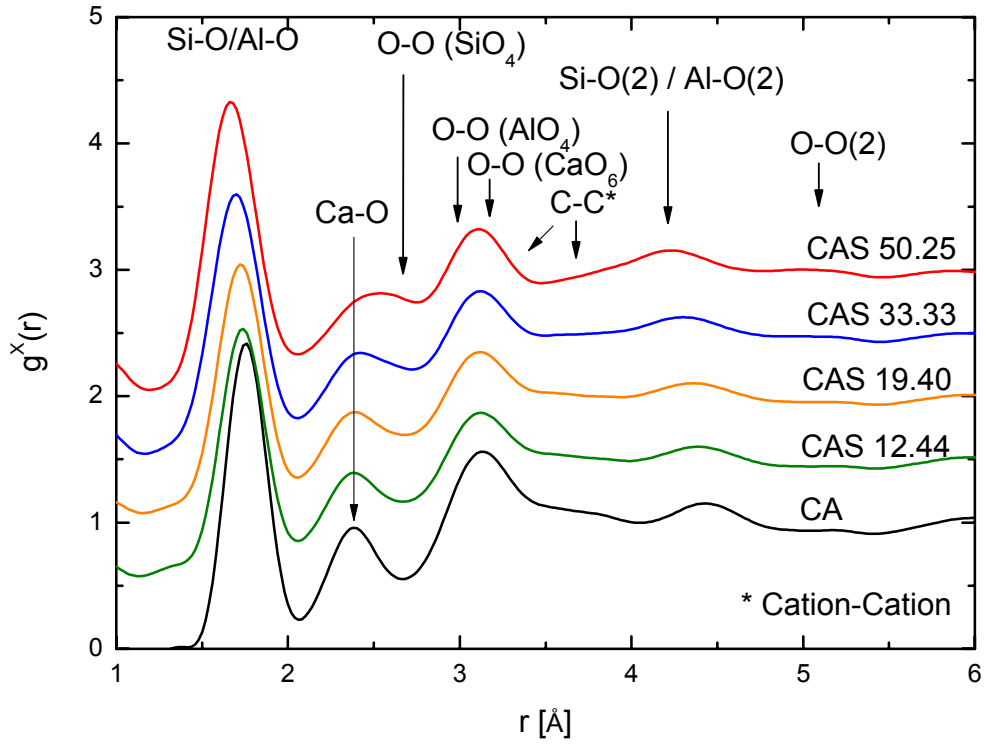

Figure 4.13 The total pair distribution function $g^X(r)$ for the $(CaAl_2O_4)_{1-x}$ $(SiO_2)_x$ glasses at room temperature as obtained by Fourier transforming the corresponding total structure factors. For clarity, the CAS compositions have been displaced by 0.5.

4.3 Conclusion

The objective of the neutron diffraction experiment was to examine the structure of our CAS composition in the short and medium range order which involved the extraction of the bond distances and the average numbers of neighbors. The major results obtained were as follows:

- For a given composition, the FSDP in the $S(Q)$ kept the same position for both states (glass and liquid).
- The dependency of the FSDP position on the silica content expresses a linear behavior. On increasing the silica content, we observe an increase in the FSDP intensity that indicates a more ordered structure (even taking into account $b_{Si} > b_{Al}$).
- In all cases, the Si kept an essentially fourfold coordination.
- The Al-O coordination number increased from ~4 in the glass state to ~4.6 in the liquid state indicating the presence of fivefold and sixfold Al species in the structure (here NMR would give an accurate answer to their proportions).
- No significant evolution in the Si-O, Al-O and Ca-O bond lengths were observed by changing the composition.

We have seen that a major difficulty is the determination of the Ca-O environment due to large overlaps with O-O correlations in the $g(r)$'s (with neutrons and x-rays). In order to extract the local environment around Ca, we conducted recently a neutron diffraction experiment with isotopic substitution (^{44}Ca) on liquid and glassy CA. The data treatment is in progress but preliminary results suggest a coordination number of 5.5 [16] consistent with the results presented here. EXAFS measurements are planned in the next few months and will give more information on the local order around Ca atoms.

Finally, as it has been done with CA [17,18], all the results will be further compared with several MD simulations which are in progress.

REFERENCES

[1] L. Cormier, D. R. Neuville, G. Calas, J. Am. Ceram. Soc. 88, 2292–2299 (2005).

[2] H. E. Fischer, G. J. Cuello, P. Palleau, D. Feltin, A.C. Barnes, Y.S. Badyal and J. M. Simonson, Appl. Phys. A 74, S160 (2002).

[3] L. Hennet, I. Pozdnyakova, A. Bytchkov, V. Cristiglio, P. Palleau, H. E. Fischer, G. J. Cuello, M. Johnson, P. Melin, D. Zanghi, S. Brassamin, J-F. Brun, D. L. Price and M-L. Saboungi, Rev. Sci. Instrum. 77 053903 (2006).

[4] T. E. Faber and J. M. Ziman, Phil. Mag. 11, 153 (1965).

[5] V. F. Sears, Neutron News 3 26 (1992).

[6] A. C. Wright, J. Non-Cryst. Solids, 179 84-115 (1994).

[7] D. R. Neuville, L. Cormier and D. Massiot, Geochim. Cosmochim. Acta, 68 5071-5079 (2004).

[8] G. S. Henderson, D. R. Neuville, L. Cormier, Chem. Geol., 259 54-62 (2009).

[9] D. R. Neuville, L. Cormier, V. Montouillout and D. Massiot, J. Non-Cryst. Solids, 353 180-184 (2007).

[10] D. R. Neuville, L. Cormier, D. Massiot, Chem. Geol., 229 173-185 (2006).

[11] V. Petkov, S. J. L. Billinge, S. D. Shastri, and B. Himmel, Phys. Rev. Lett. 85, 3436-3439 (2000).

[12] C. J. Benmore, J. K. R. Weber, S. Sampath, J. Siewenie, J. Urquidi and J. A. Tangeman, J. Phys. Cond. Mat. 15, S2416 (2003).

[13] D. R. Neuville, L. Cormier, A. M. Flank, V. Briois and D. Massiot, Chem. Geol., 213 153-163 (2004).

[14] B. T. Poe, P. F. McMillan, B. Coté, D. Massiot and J. P. Coutures, Science, 259 786-788 (1993).

[15] P. Courtial, D. B. Dingwell, Geochim. Cosmochim. Acta, 59 3695-3695 (1995).

[16] J. Drewitt, Private communication

[17] V. Cristiglio, L. Hennet, G. J. Cuello, I. Pozdnyakova, M. Leydier, J. Kozaily, H. E. Fischer, M. R. Johnson and D. L. Price, 356 2492–2496 (2010).

[18] J. W. E. Drewitt, S. Jahn, V. Cristiglio, A. Bytchkov, M. Leydier, S. Brassamin, H. E. Fischer, L. Hennet, J. Phys. Cond. Mat., 23 155101 (2011).

Résumé du Chapitre 5

Ce chapitre présente les propriétés dynamiques des CAS essentiellement pour trois compositions: x = 0, 0.1182 et 0.1899 dans le but de déterminer la variation de la fragilité au sens d'Angell.

Dans la première partie de ce chapitre, les premiers résultats des expériences de diffusion quasi-élastique des neutrons sont présentés. Ces expériences ont été effectuées sur l'instrument IN6 en utilisant des longueurs d'onde de 5.1 et 4.1 Å. Ceci correspond à une gamme en Q de 0.3-2.4 $Å^{-1}$. Nous avons pu déterminer les facteurs de structure dynamiques $S(Q,\omega)$ desquels nous avons déduit les fonctions de diffusion intermédiaires $S(Q,t)$ par transformée de Fourier. Pour toutes les compositions étudiées, $S(Q,t)$ décroit d'une manière lisse et continue indiquant l'absence d'effet de cage. Les spectres $S(Q,t)$ présentent une forme exponentielle étirée et ont été mieux décrit par le modèle KWW duquel nous avons extrait les temps de relaxation.
Une observation importante est que, contrairement à la plupart des systèmes cohérents, nous n'avons pas mis en évidence de rétrécissement de De Gennes (De Gennes narrowing) à la position du pic maximal dans le facteur de structure $S(Q)$. En prenant en considération la nature cohérente de notre système, les coefficients de diffusion cohérents ainsi que les énergies d'activation que nous avons trouvés sont en bon accord avec les données publiées. Pour le CA, les temps de relaxation correspondant à la distance interatomique de la première sphère de coordination (FSDP) se positionnent relativement bien avec les données de viscosité macroscopique et celles obtenues par RMN suggérant que le mécanisme de relaxation sondé est le même. Lors de l'ajout de SiO_2, nous avons obtenu des temps de relaxation plus lents ainsi que des coefficients de diffusion cohérents et des énergies d'activation inferieurs à ceux du CA (x=0). Pour obtenir une vision du comportement de la fragilité de ces liquides, nous avons comparé leurs viscosités (temps de relaxation) en les plaçant dans la représentation proposée par Angell. Nous avons pu voir qu'en augmentant la concentration en silice dans la composition, la dépendance de la viscosité sur la température devient plus faible, ce qui indique un caractère moins fragile. Par contre, nous avons remarqué que l'ajout de la silice jusqu'à 20% n'a pas changé de façon significative la fragilité. Pour mieux voir le déplacement de la fragilité vers la limite du liquide fort, il est donc nécessaire d'augmenter d'avantage la proportion de silice.

La seconde partie de ce chapitre présente l'étude de la dynamique à haute fréquence par diffusion inélastique des rayons X. Les expériences ont été effectuées sur la ligne de lumière ID16 de l'ESRF. Nous avons travaillé avec une énergie incidente de 23.725 keV et une résolution de 0.83meV. Pour analyser les facteurs de structure dynamiques, ces derniers ont été analysés en utilisant un modèle provenant de l'hydrodynamique généralisée, qui est une extension de l'hydrodynamique classique associée au formalisme des fonctions mémoires. Ces

dernières décrivent les interactions du système et contiennent les informations sur les propriétés thermodynamiques et les propriétés de transport. Nous avons pu déterminer les relations de dispersion des modes acoustiques longitudinaux ainsi que les processus de relaxation. Les résultats ont montré que les courants longitudinaux et les courbes de dispersion à fréquence infini présentent un comportement linéaire et coïncident dans toute la gamme de vecteurs d'onde Q étudiée (1-5.8 nm^{-1}). On ne voit donc pas la transition entre le régime non relaxé et complètement relaxé. Les vitesses du son longitudinales et isothermes présentent un comportement opposé avec la température et diminuent avec l'ajout de silice. Les temps de relaxation décroissent d'une manière exponentielle en fonction de Q et en extrapolant à la valeur $Q = 0$, nous avons obtenu des valeurs du temps de relaxation qui sont du même ordre de grandeur que les temps obtenus par nos mesures QENS aux alentours du premier pic de diffraction. Finalement, nous avons pu voir que la relaxation structurale dominait la contribution liée à la viscosité longitudinale et que contrairement aux compositions à 10% et 20% de silice qui semblent avoir des degrés de fragilité voisins, l'échantillon à 33% de silice semble présenter un comportement moins fragile.

Il ressort de cette étude qu'il est indispensable de la compléter par des simulations de dynamique moléculaire afin de modéliser précisément la dynamique de ces verres.

CHAPTER 5

5 DYNAMICS

This chapter discusses the dynamical study. It comprises two main sections where the results obtained from the Quasi-elastic Neutron scattering and Inelastic X-ray Scattering are discussed and concluded separately.

5.1 QENS Measurements

As mentioned in the introductory chapter, a goal of this thesis is to study the effects of doping the highly fragile glass-former $CaO\text{-}Al_2O_3$ (CA) with a strong glass-former such as SiO_2. Specifically, in terms of dynamics, to quantify the expected decrease in fragility by extracting average relaxation times, diffusion coefficients as well as the resulting activation energies upon increasing the SiO_2 content. We are considering CA as the starting composition to which the network former is added.

Element	b_{coh} [fm]	σ_{coh} [barns]	σ_{incoh} [barns]
O	5.805(4)	4.232(6)	0.000(8)
Al	3.449(5)	1.495(4)	0.0082(6)
Ca	4.70(2)	2.78(2)	0.05(3)
Si	4.15071(22)	2.1633(10)	0.004(8)

Table 10. The coherent and incoherent cross sections for the different atomic species in the $(CaAl_2O_4)_{1-x}$ $(SiO_2)_x$ system.

Note that we are considering a nearly purely coherent scattering system, which has two consequences:

Firstly, to measure properly single-atom diffusion and/or density of vibrational states in QENS, it's necessary to cover a range of $S(Q,\omega)$ that approaches the self-scattering limit $S(Q) \to \overline{b^2}$. For a strongly incoherent scattering system such as hydrogen, the self-scattering is dominant at low Q values and thus easily accessible with cold neutrons as at IN6. However, a coherently

scattering system generally needs higher Q values, and hence higher incident neutron energy, in order to approach the self-scattering limit corresponding to single-atom diffusion.

Secondly, when a system's scattering is dominated by one incoherent scatterer such as hydrogen, the values of relaxation time and diffusion constant extracted from the QENS data are basically those of that incoherent scatterer. However, in our coherent scattering system, we extract relaxation times and diffusion constants that are an average over all the atomic species, weighted by concentration and coherent neutron scattering length.

In fact, both the scattering length and concentration is greatest for oxygen, which is believed to be the most mobile species, so we are not too handicapped by the averaging over atomic species. In addition, as we will show later, we saw no evidence of de Gennes narrowing in our relaxation times as a function of Q, suggesting that in spite of a limited Q range, our QENS results represent single-atom diffusion, mostly due to oxygen in all likelihood.

Finally, documents [1-7] have provided useful information for this section.

5.1.1 Experimental details

IN6 spectrometer

The IN6 instrument is a time-focusing TOF spectrometer designed for QENS and INS at incident wavelengths in the range of 4 to 6 Å. It is well suited to study the dynamics and relaxation properties in condensed matter. A detailed description of the instrument is given in [8]. In this study, we used an incident neutron wavelength of 5.1 Å and 4.1 Å providing a measured elastic energy resolution (FWHM) of 69 μeV and 170 μeV respectively. The incident neutron beam is pulsed by a system of two Fermi choppers. Higher order contributions of the monochromator are efficiently removed by a Be filter.

The sample chamber can be evacuated down to 10^{-4} mbar. The chamber has a cylindrical shape with an inner diameter of 342 mm at a height of 865 mm. The sample chamber is separated from the He filled flight chamber and the detector bank by a thin aluminium sheet window. This allows for fast pumping of the chamber, thus optimizing measurement time. The sample chamber is also motorized in the vertical direction, which allows to position efficiently the levitated sample in the neutron beam. The detectors cover an angular range of 10° to 115° in 2θ, providing a Q range for elastic scattering of [0.3 - 1.9] $Å^{-1}$ and [1.15 – 2.4] $Å^{-1}$ at an incident neutron wavelength of 5.1 Å and 4.1 Å respectively.

Experimental configuration and procedure

A 3D drawing of the experimental setup is presented in Fig. 5.1. The entire apparatus is mounted on the same support structure in order to assure a stable alignment of the laser optics focused on the sample. A side window in the vacuum chamber (bottom chamber) allows an easy access for sample changing.

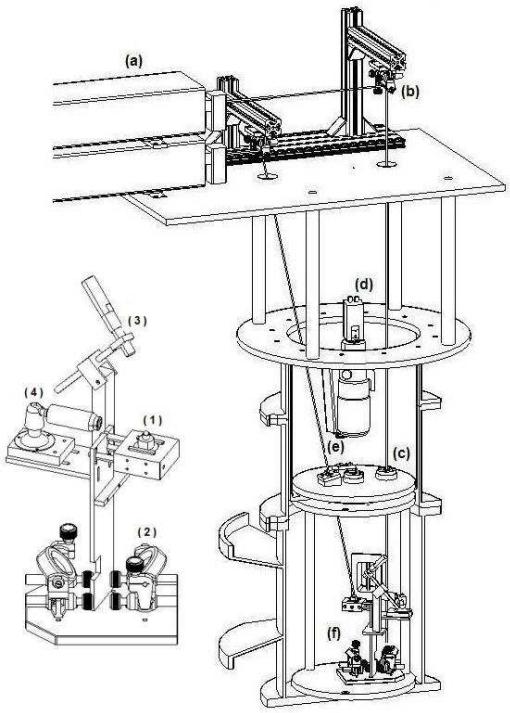

Figure 5.1 Computer Aided Design of the levitation setup at IN6: lasers (a), mirrors (b), NaCl windows (c), video camera (d), external pyrometer (e) and the levitator (f). The insert shows detail of the levitator: levitator nozzle (1), bottom concave mirror (2), internal pyrometer (3) and side view video camera (4).

The position of the sample is aligned with respect to the beam by taking a neutron polaroid photograph of a neutron-absorbing piece of cadmium mounted on the nozzle at the sample position. Other than upstream slits, the incident neutron beam finally striking the sample is reduced via a 10 mm punched cadmium (Cd) mask mounted in front of the nozzle. Background is further reduced by wrapping in Cd all other parts in the sample chamber. There is no danger of melting the Cd since the heating is very localized and the total used-power of the lasers is comparable to that of a household light bulb.

The sample is heated by means of two 125 W CO_2 lasers operating at a 10.6 μm wavelength with an initial beam size of 5 mm. The primary laser beam (providing most of the heat to the sample) is focused from above by a concave mirror onto the sample with a final beam diameter of 2 mm. The second laser beam, of weaker power, is mainly used for temperature-

homogeneity purposes. It is reflected through two flat and one concave copper mirrors before hitting the sample from below, passing through the nozzle's conical interior.

Two single-wavelength optical pyrometers, one internal and another external to the sample chamber, were used to measure the temperature of the levitated sample. They work at a wavelength of 0.85 μm and 1.65 μm respectively, enabling together an accurate measurement of the temperature. Before data acquisition, the sample chamber is pumped down to low pressure and then filled with the levitation gas at atmospheric pressure. This is mainly to avoid air scattering which leads to a broad background in the region of interest around the elastic line. Two test measurements, made ~ 30 min apart, are conducted in order to make sure that there is no evolution in background neutron counts (scattered by the levitation gas), and that the experimental conditions are reproducible.

5.1.2 Results and Discussion

Using an incident wavelength of 5.1 Å and 4.1 Å allowed us to explore a region of momentum transfers within $0.3 \le Q \le 2.4$ Å^{-1}. However, due to the instrumental resolution limitations, the *Q*-region below 1.15 Å^{-1} was not properly accessible at the measured temperatures. And so only data for momentum transfers between $1.15 \le Q \le 2.4$ Å^{-1} (from both working wavelengths) are presented. This range spans the region of the first diffraction peak in the static structure factor *S(Q)*, as measured by neutron and x-ray diffraction [9], and thus allows us to focus on the relaxation processes at the length scale of the nearest neighbors since the coherent part dominates the total scattering of the CAS samples.

CA $(x = 0)$

The measurements were performed in the range of 1753 K to 2473 K in the liquid state. Given the melting ($T_m = 1878\,\mathrm{K}$) and the glass transition ($T_g = 1178\,\mathrm{K}$) temperatures of CA, we were able to go 100 K in the undercooled state and the observed temperature range was $0.93 \le T_m / T \le 1.32$ and $0.48 \le T_g / T \le 0.67$.

From the resulting differential intensity, the scattering function $S(Q,\omega)$ is calculated by interpolation to constant Q values by intervals of 0.2 Å^{-1} over an energy range of [-2, 2] meV. Fig. 5.2 (left) shows selected $S(Q,\omega)$ data for CA $(x = 0)$ from QENS, for which the acquisition time was about 12 hours per temperature except for the two lowest temperatures where a 2mm sample was measured for about 24 hours. The QENS signal is accurately measured outside the resolution of the instrument. The Al phonon dispersive curve is far enough away in (Q,ω) space from our sample's signal to provide data of sufficient quality for FT to the intermediate scattering function $S(Q,t)$, as shown at the right of Fig. 5.2.

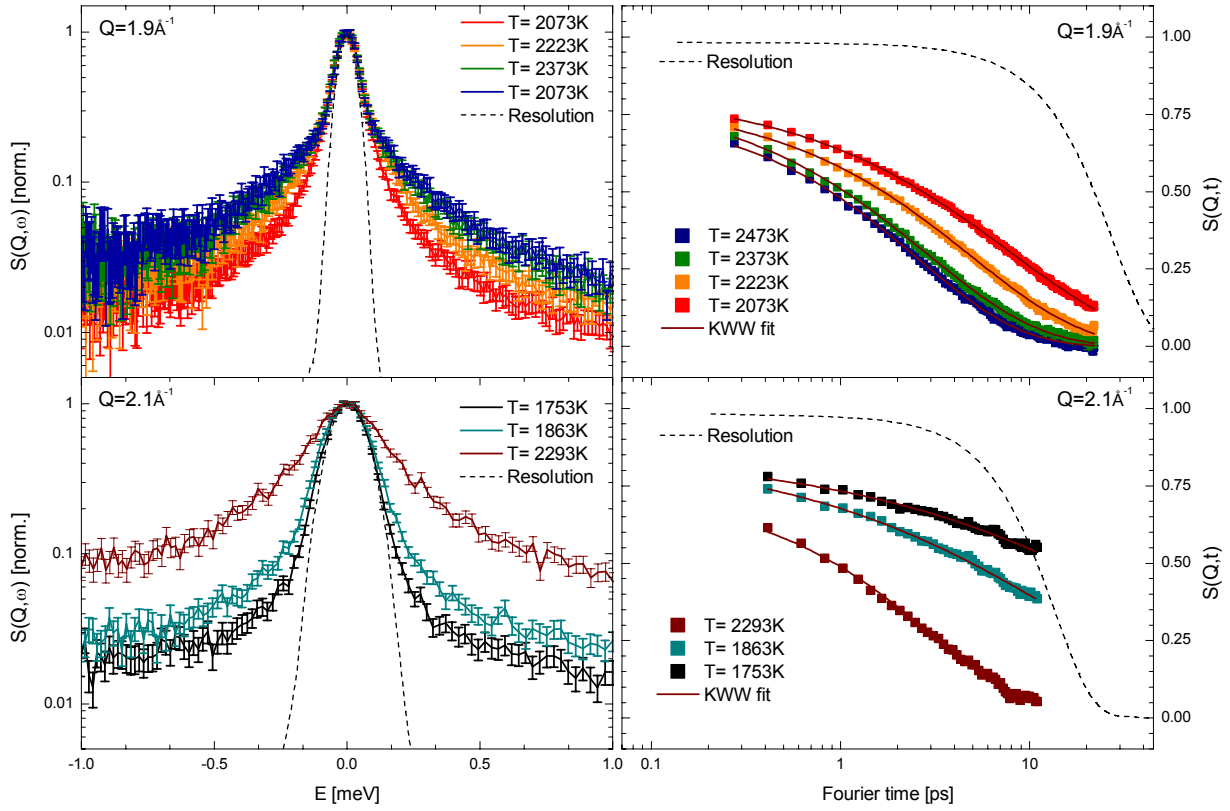

Figure 5.2 $S(Q,\omega)$ spectra for $CaAl_2O_4$ (left) and the corresponding intermediate scattering functions (right) for all the investigated temperatures at two wavevectors around the FSDP. The solid lines are stretched exponential fits.

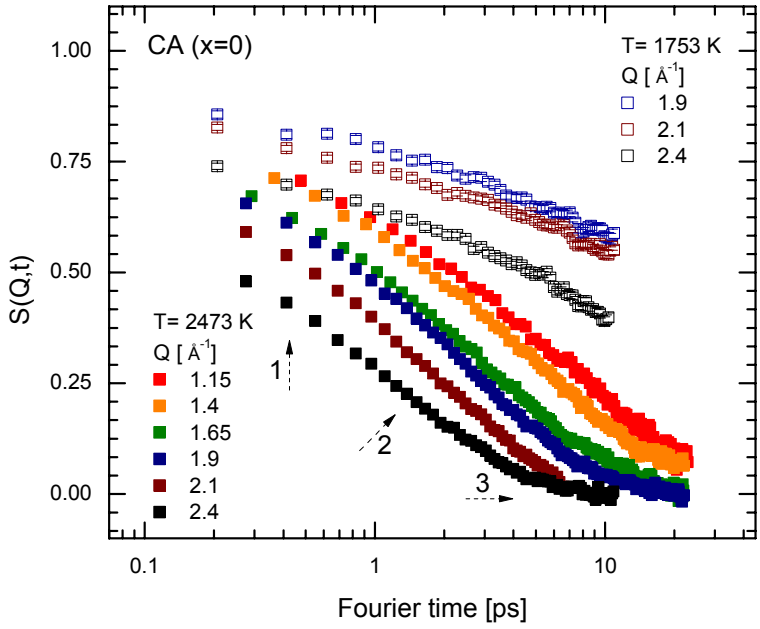

Figure 5.3 Linear-logarithmic plot of the intermediate scattering functions versus time at different wavevector values for the two extreme investigated temperatures, for the CA $(x = 0)$ obtained from QENS.

Fig. 5.3 shows the decay of the intermediate scattering function $S(Q,t)$ as a function of momentum transfer Q and time t. The first important point to realize is that, in the whole temperature range, the $S(Q,t)$ profiles do not display a two-step decay but they evolve in a smooth continuous way following a single-step process in the whole explored time window (0.3-25 ps), without reminiscence of cage effects.

Furthermore, from a comparison of the behaviour at the two temperatures, one can observe at the higher temperature (see the dashed arrows):

1. a greater dispersion in Q
2. a curvature change
3. the reaching of an asymptotic value at long times (plateau).

With increasing Q, the relaxation times become faster. This observation clearly shows the signature of a simple liquid dynamics where a diffusivelike behaviour is occurring.

Fig. 5.2 (right) displays selected $S(Q,t)$ spectra which clearly show stretched functional forms away from the single-relaxation process for all the investigated temperatures. Such behaviour is usually explained by the presence of different superposed simple exponential relaxations, and is a typical feature of fragile glass forming systems.

We have decided to fit the decay of these coherent intermediate scattering functions by the well-known stretched exponential function, more specifically with a Kohlrausch-Williams-Watts (KWW) function,

$$S(Q,t) = A\exp[-(t/\tau)^{\beta}] \tag{5.1}$$

where A is the amplitude, τ is the relaxation time and $\beta < 1$ is the shape parameter or stretched exponent which quantifies the deviation from simple exponential decay $(\beta = 1)$. All the three parameters A, τ and β depend on both transferred momentum and temperature. For this reason, different fitting procedures were performed by adjusting the parameters in a way that presents a definite physical meaning. We were not able to describe the data with a temperature-independent beta value for a given Q-value, nor by fixing beta to a Q-independent constant for all the fits. A free fit for all the parameters was found to work the best.

In Fig. 5.4 (left), the obtained relaxation times as a function of wave-vector are reported for all the temperatures measured. We can see that that the data display a strong dependence on the wave-vector. The relaxation times increase with a decreasing of the wave-vector and

temperature. However, contrary to the behaviour of most coherent scattering liquids, the system does not present a pronounced relaxation time at the position of the first diffraction peak ($Q = 2.1$ Å^{-1}), known as the "De Gennes" narrowing [10].

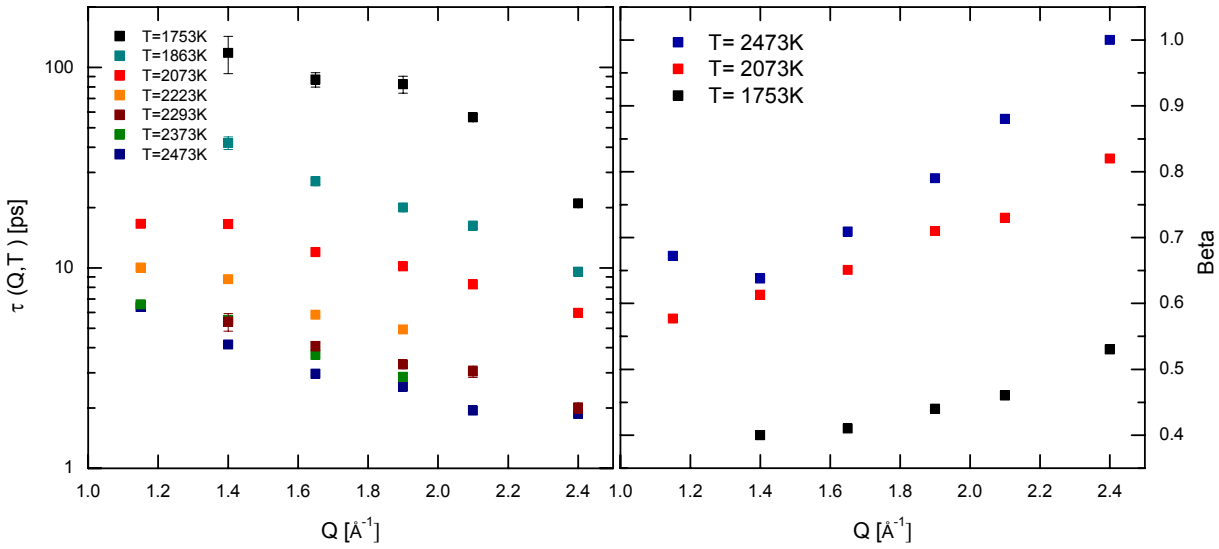

Figure 5.4 wave-vector dependence of the extracted relaxation times (left) and stretching exponent β (right) for selected temperatures (QENS data on CA).

Fig.5.4 (right) shows the Q dependence of the shaping parameter for the two extreme and one intermediate temperature. The results clearly show an increase of the shape parameter as a function of Q and temperature. In the high temperature region, as it could be seen from Fig. 5.5, the significant result is that the intermediate scattering function becomes closer to a single exponential where β increased up to a value of 1 at the highest temperature.

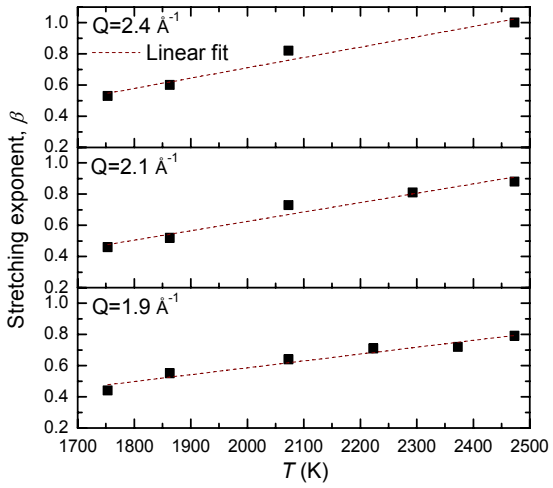

Figure 5.5 Temperature dependence of the stretching parameter β around the Q value corresponding to the first diffraction peak in CA ($Q = 2.1$ Å^{-1}), obtained from KWW fits to QENS data.

Since τ and β are strongly correlated, we decided to consider the mean relaxation time [1] that is:

$$\langle\tau\rangle = \frac{\tau}{\beta}\Gamma\left(\frac{1}{\beta}\right) \tag{5.2}$$

where Γ is the gamma function.

It clearly emerges that if we investigate the *Q*-dependence of the intermediate scattering function in more detail, the mean relaxation rates follow a canonical (Fickian) Q^2 dependence for $Q > 1$ Å^{-1} even though we are dealing with a majoritarily coherent scatterer. Such a dependence is a characteristic feature of stochastic translational diffusion of individual atoms, which therefore is dominating the dynamics on the corresponding length scale of less than $2\pi/Q \approx 6$Å. Again, keeping in mind that CA is a mostly coherent scatterer, the diffusion coefficients $D = 1/\langle\tau\rangle Q^2$ were estimated from linear fits to all the data points with an offset fixed to zero. The data are summarized and presented in Fig. 5.6.

Fig. 5.7 shows the evolution of the diffusion coefficient with regard to the temperature. The diffusion coefficient decrease with a decreasing temperature. Values range from (9.8 ± 0.3) $\times 10^{-10}$ m^{2}s^{-1} at 2473 K to (0.3 ± 0.08) $\times 10^{-10}$ m^{2}s^{-1} at 1753 K. At the melting point, the diffusion coefficient of CA is (~ 0.9 ± 0.12) $\times 10^{-10}$ m^{2}s^{-1} (table 11).

Over this relatively restricted temperature range, a logarithmic plot shows that the diffusion coefficients follow almost a linear behavior (insert in Fig. 5.7). We then described the temperature dependence *D* with an Arrhenius behaviour,

$$D = D_0 \exp(-E_A / k_B T) \tag{5.3}$$

where D_0 is a prefactor and E_A the activation energy. The best fit gives $E_A = (1.8 \pm 0.1)$ eV/atom = (172 ± 9) kJ mole^{-1}. Urbain et al. [11] measured the shear viscosity of five $(CaO)_x$ $(Al_2O_3)_{x-1}$ (x = 0.374, 0.5, 0.576, 0.621 and 0.813) liquids and estimated their activation energy from the viscosity-temperature dependency using the Weymann relation. Their CA (x = 0.5) appeared to have the highest activation energy of $E_A = (189 \pm 5)$ kJ mole^{-1}, in good agreement with our value.

The data points in red were obtained from a previous INS measurement on the triple axis spectrometer IN8 [12] at the ILL. A wavelength of 2.36 Å was used which provided a *Q*-range of $0.7 \le Q \le 2.7$ Å^{-1}.

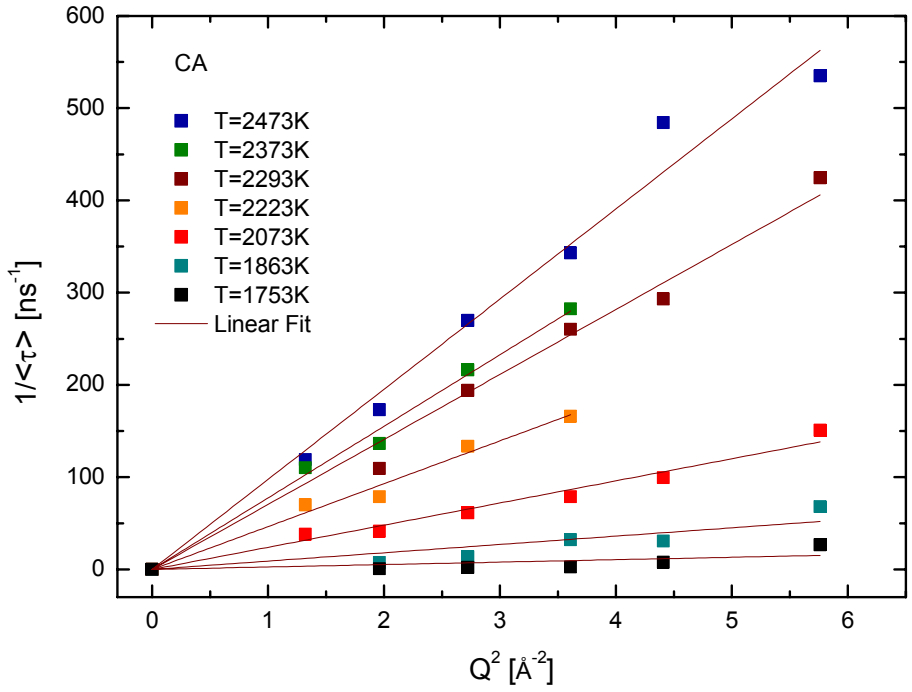

Figure 5.6 The mean relaxation times for CA show a Fickian Q^2 dependence. The solid lines are linear fits to estimate the coherent diffusion coefficient.

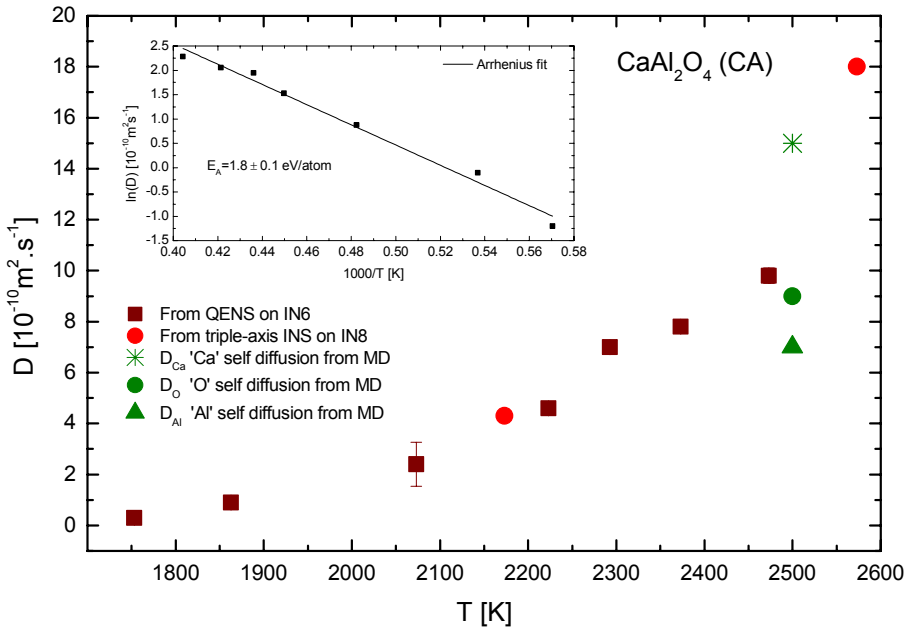

Figure 5.7 Temperature dependence of the coherent diffusion coefficient for CA as obtained by QENS. The red dots are the data obtained by INS on IN8 and the green symbols represent the self diffusion coefficient for the different atomic species obtained by MD simulations taken from [13].

The diffusion coefficients were extracted from the IN8 data using an energy-domain analysis as described by [14] as follows: $D = \lim_{Q\to 0}(\Gamma_{\text{trans}} / Q^2)$ where Γ is the Half Width at Half Maximum (HWHM) of the $S(Q,\omega)$ fitted with a simple lorentzian. We can see that both sets of experimental data, from the IN8 and IN6 instruments, are consistent with each other. S. Jahn et al. [13] performed molecular dynamics simulations on $CaAl_2O_4$ at 2500 K. The calculated partial diffusion coefficients of each atomic species in the sample are reported in green as well. We can see that the closest values to our data are the partial diffusion of Ca cations and that of the oxygen anions. Aluminium is reported to have the lowest diffusivity.

T [K]	D [10^{-10} m^2s^{-1}]
2473	9.8 ±0.30
2373	7.8 ±0.18
2293	7 ±0.20
2223	4.6 ±0.16
2073	2.4 ±0.86
1863	0.9 ±0.12
1753	0.3 ±0.08

Table 11. CA coherent diffusion coefficient measured by quasielastic neutron scattering [T_m(CA)=1878 K].

Now if we focus, for a given Q value, on the temperature dependence of the mean relaxation time $\langle\tau\rangle$, or viscosity η according to the Maxwell law $\tau_s = \eta_s / G_\infty$ (τ and η are roughly proportional since G_∞ is much less temperature-dependent than τ or η), we clearly see that the relaxation exhibits a non-Arrhenius behavior.

Fig. 5.8 (Down) shows an Arrhenius plot of the mean relaxation times for different Q values around the FSDP. Macroscopic viscosity data measurements of Urbain [11] are as well reported for comparison. When the macroscopic experimental data are fitted with a modified form of the Vogel-Fulcher-Tamman (VFT) equation (the solid line in Fig. 5.8):

$$\eta = \eta_0 \exp(DT_0 / T - T_0) \tag{5.4}$$

where the single parameter D describes the extent to which the liquid follows the Arrhenius behavior. It is well known that a large value of D, on the order of 100, implies a strong liquid whereas a small value of D (less than 10) indicates a very fragile or non Arrhenius liquid. One obtains a value of D = 3.20, which is close to those obtained for the most fragile glass-forming systems observed to date and a value of T_0 = 1205 K, that is a value close to the measured glass transition temperature (T_g = 1178 K) which is also a characteristic of a fragile liquid system.

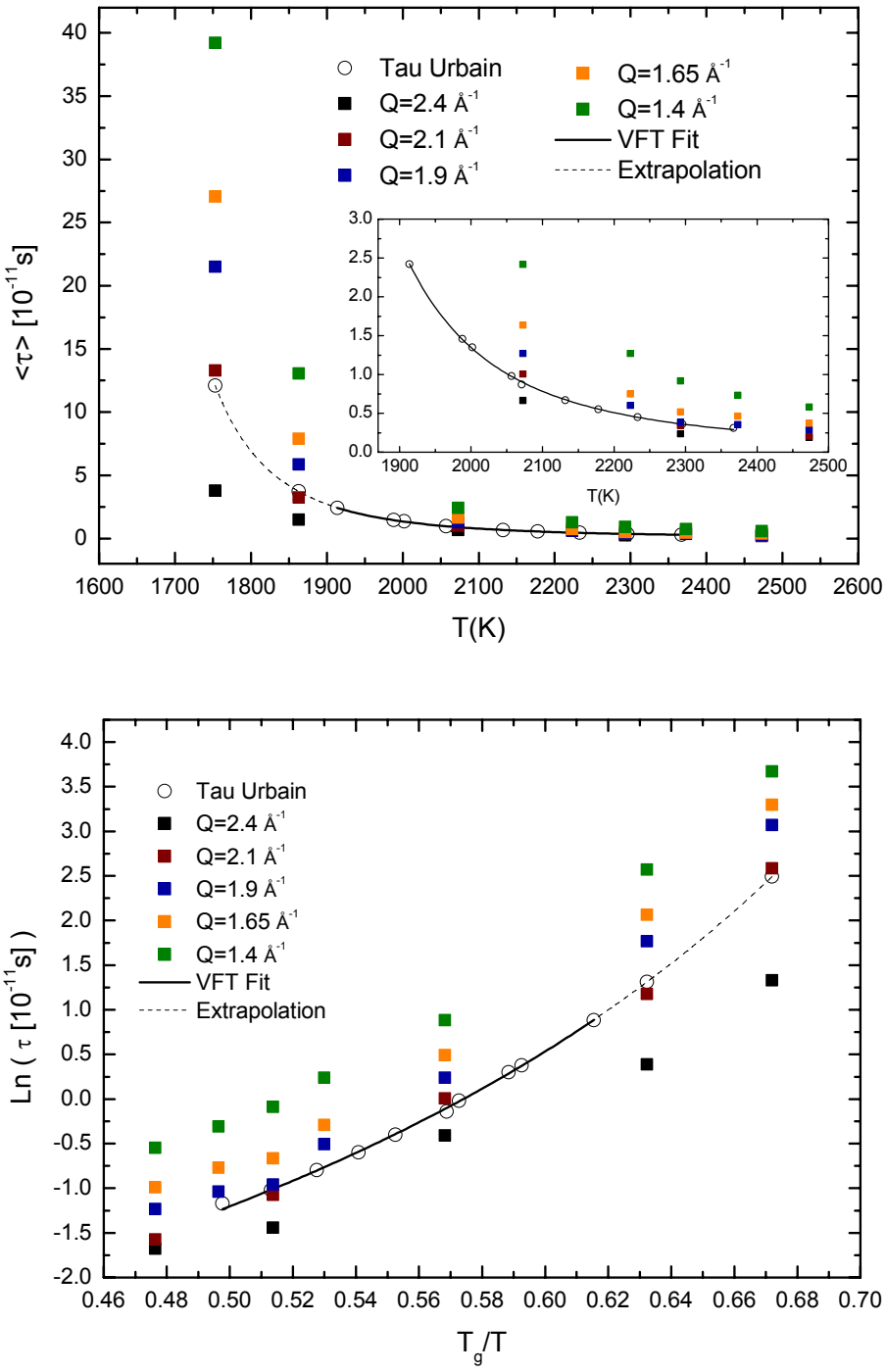

Figure 5.8 (Up) Temperature dependence of the mean relaxation times obtained by QENS on $CaAl_2O_4$. Macroscopic shear viscosity (scaled) taken from [11] is also reported. The dotted line is an extrapolation to lower temperatures of the VFT fit (D = 3.2 and T_0 = 1205 K) to the measured shear viscosity [15]. (Down) Arrhenius representation for the same data.

If we look at the insert of Fig. 5.8 (Up), where the temperature scale was limited to the lowest temperature measured by Urbain (T = 1914 K), we see that the mean structural relaxation times are very comparable to the shear relaxation times. At high temperatures, the relaxation times for the different wave vector converge to short time values. However, on lowering the temperature, we see a larger dispersion in tau values and the relaxation times corresponding to $Q = 2.1$ Å^{-1} seem to be the closest ones to the macroscopic values. When we extrapolate the VFT fit (dashed line) to the lowest two temperatures measured ($T \approx T_m$ and $T \approx T_m - 100$) in our QENS experiment, we see that the data at the first peak in the structure factor $S(Q) = 2.1$ Å^{-1} are still in an excellent agreement with the extrapolated VFT fit.

Actually, Poe et al. [15] calculated viscosities from the oxygen diffusivity in liquid CA at much higher temperatures by performing ion dynamics simulation and using the Stokes-Einstein relation $\eta = k_B T / 6\pi\mu r$. His results were found to follow the same VFT fit. We can see as well in Fig. 5.9 the NMR relaxation times obtained by Massiot et Al. [16] (left hand side) and our QENS data (right hand side) reported together with the viscosity data taken by Urbain [11].

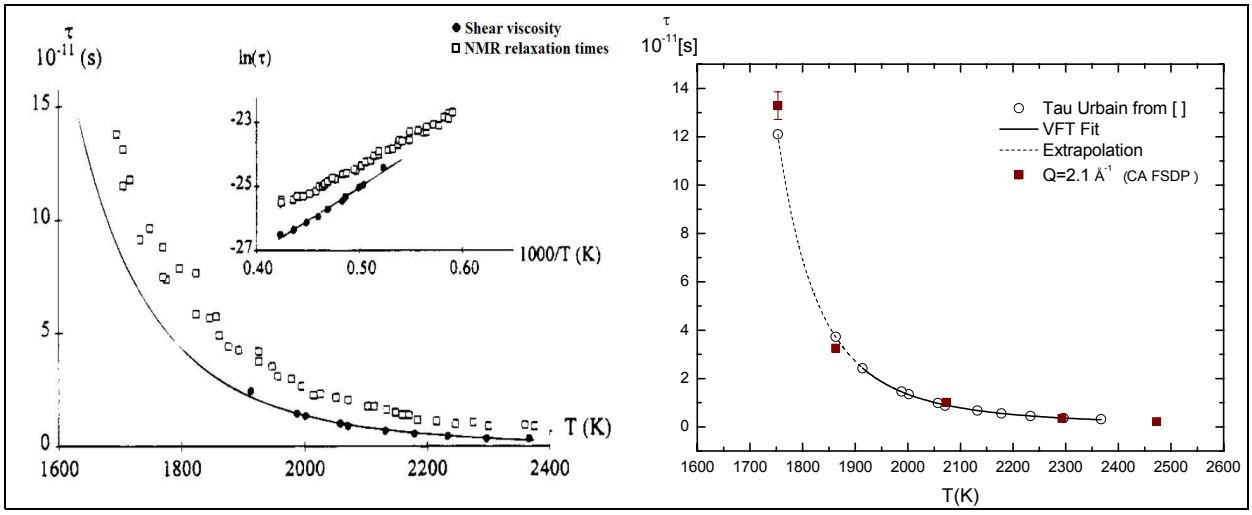

Figure 5.9 Relaxation times obtained by NMR [16] (left) and QENS (right) reported together with the shear viscosity.

The most important observation is that the relaxation time values obtained on IN6 closely match the data obtained by viscosity and NMR measurements, also showing the same temperature dependence which strongly suggests that the relaxation mechanism is the same.

Finally, we present in Fig. 5.10 the resulting $\langle\tau\rangle$ ($Q = 2.1$ Å^{-1}) parameters on an Angell plot reported with the macroscopic viscosity data obtained by Urbain. If we fix the high and low temperature limits to -4 and 13 respectively, the VFT fit (red dashed line) to our mean relaxation times $\langle\tau\rangle$ ($Q = 2.1$ Å^{-1}) obtained by QENS measurement gives a value of $D = 5 \pm 1.8$

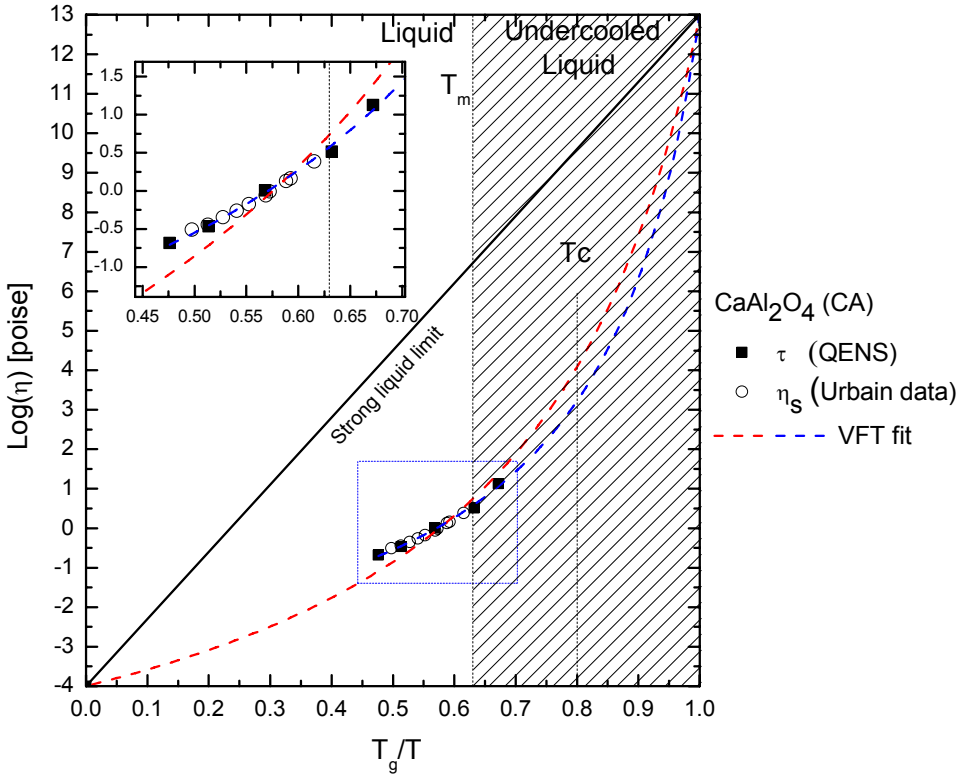

Figure 5.10 Angell representation of the mean relaxation times at the FSDP ($Q = 2.1$ Å^{-1}) for liquid $CaAl_2O_4$ obtained by QENS. Macroscopic viscosity data taken from [11] are as well reported. T_m indicates the melting temperature of CA whereas Tc refers to the critical temperature where significant structural changes are reported to occur upon quenching [17].

and T_0 = 908 ± 85 K. We can observe the non Arrhenius behavior that characterizes fragile liquids. For direct determination of the fragility from the slope of the curves at T_g, the attained temperature range is not sufficient and therefore we limit our fragility index to the D parameter.

However, by looking at the insert of Fig. 5.10, we observe that the fit doesn't match correctly the experimental data. Actually, it has been showed that one VFT expression is not always sufficient to fit the experimental data. A satisfactory account is sometimes obtained by an Arrhenius expression at high temperatures with a crossover to a VFT expression at some temperature T_A and another crossover to a second VFT expression at a lower temperature T_B [18]. For this reason, we performed a second VFT fit (blue dashed line) applied only to the lower temperature limit by fixing only the relaxation time (i.e 100s or 10^{13} poise) corresponding to the glass transition. We see a very good agreement between the fit and the experimental data giving a value of D = 2.7 ± 0.2 and T_0 = 1007 ± 9 K. Here should be mentioned that the value of D = 3.2 and T_0 = 1205 K obtained by Poe et Al. [15] mentioned earlier were extracted from a VFT fit which was limited to the experimental data without any extrapolation to the $T_g/T = 0$ and 1 limits.

Addition of SiO_2

Two $(CaAl_2O_4)_{1-x}$ $(SiO_2)_x$ liquids CAS 12.44 (x = 11.82) and CAS 19.40 (x = 18.99) were examined in order to study the influence of the silica content in this ternary system. Given their melting and glass transition temperatures 1893 K and 1137 K for CAS 12.44 and 1863 K and 1137 K for CAS 19.40 respectively, the observed temperature range was $0.48 \le T_g / T \le 0.62$ for CAS 12.44 and $0.51 \le T_g / T \le 0.62$ for CAS 19.40. The lowest temperature measured was closed to their melting points. We note that, for comparison purposes, all the figures in this sub-section contain as well the respective parameters for CA.

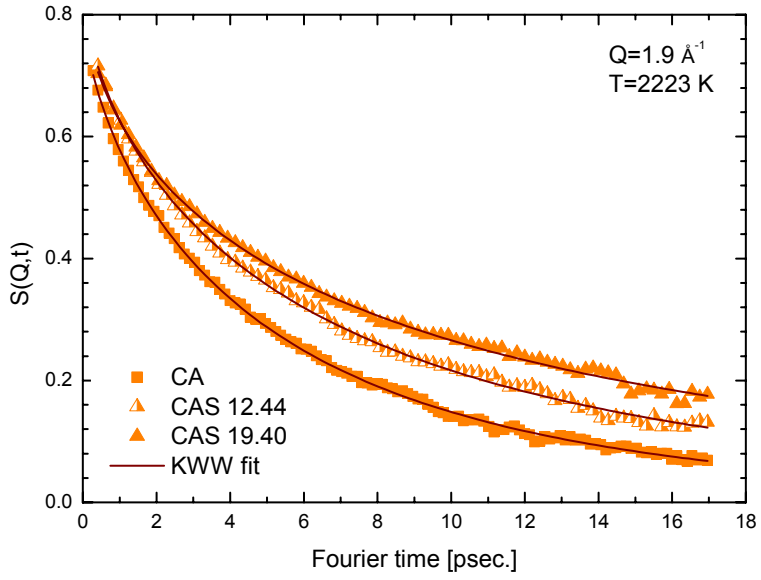

Figure 5.11 Comparison between the CA, CAS 12.44 and CAS 19.40 intermediate scattering function decay at 2223 K for Q=1.9 $Å^{-1}$.

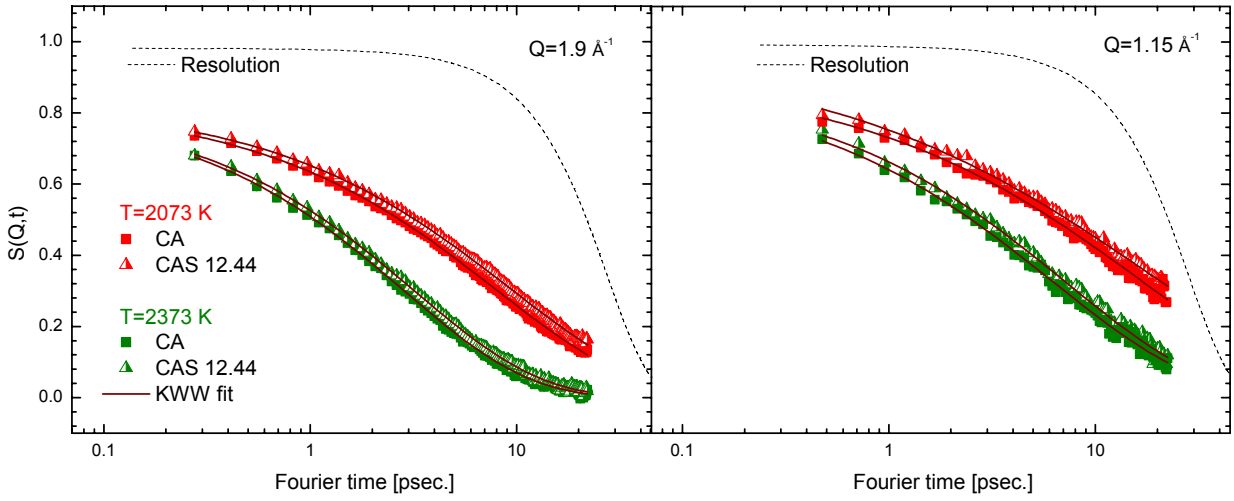

Figure 5.12 Comparison between the CA and CAS 12.44 intermediate scattering function decay at the indicated wave vectors and temperatures (semi logarithmic plot).

In Fig. 5.11, the decay of the intermediate scattering functions for the two compositions studied CAS 12.44 and CAS 19.40 are reported together with the one for CA for the same inspected temperature 2223 K and wave vector $Q = 1.9$ Å^{-1}. We can clearly see that the addition of small amount of silica to the Calcium Aluminate leads to a slower relaxation rates as it can be observed from the intensity profiles. For comparison purposes, we show in Fig. 5.12 the difference in the intermediate scattering functions for CA and CAS 12.44 at two distant wave vectors and two common measured temperatures (indicated on the graph). The solid lines in Fig. 5.11 and Fig 5.12 represent the KWW fit and we can see the good agreement between the experimental data and the fit.

The *Q*-dependency of the obtained relaxation times for all the investigated composition (including CA) are presented in Fig. 5.13 for the common (and some close) temperatures measured. First we can observe that, for a fixed *Q* value, the relaxation time increases with increasing the SiO_2 concentration and secondly, similarly to the CA, the CAS keep the same increasing trend in τ with decreasing *Q* value.

Considering that the "Si" atom is also a nearly pure coherent scatterer, we recall that the estimated coherent diffusion coefficients for CAS again refer to an average collective atomic motion in our system. We present in Fig. 14 the coherent diffusion coefficients calculated for all our compositions which are also listed in table 12.

	D [10^{-10} m^2s^{-1}]		
T [K]	CA	CAS 12.44	CAS 19.40
2473	9.8 ± 0.30	--	--
2373	7.8 ± 0.18	6.7 ± 0.19	--
2293	7 ± 0.20	--	--
2223	4.6 ± 0.16	3.1 ± 0.13	2.6 ± 0.16
2073	2.4 ± 0.86	2 ± 0.01	--
2053	--	1.9 ± 0.10	--
1973	--	--	1.1 ± 0.17
1873	--	0.8 ± 0.02	--
1863	0.9 ± 0.12	--	--
1823	--	--	0.5 ± 0.07
1753	0.3 ± 0.08	--	--

Table 12. Coherent diffusion coefficients for liquid $(CaAl_2O_4)_{1-x}$ $(SiO_2)_x$ obtained by QENS.

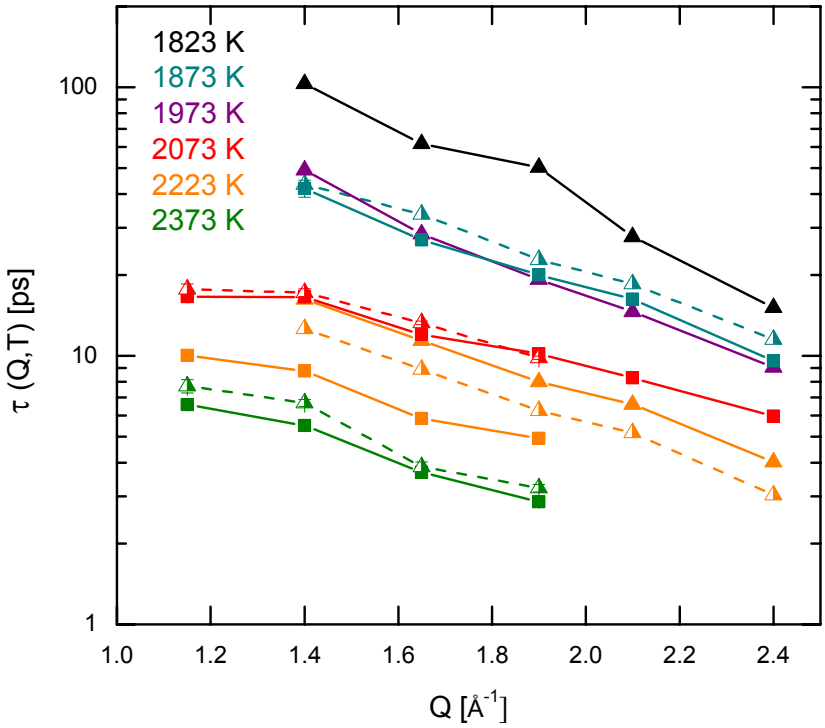

Figure 5.13 Structural relaxation times for CA (squares), CAS 12.44 (half open triangle) and CAS 33.33 (full triangle) at the indicated temperatures obtained by QENS.

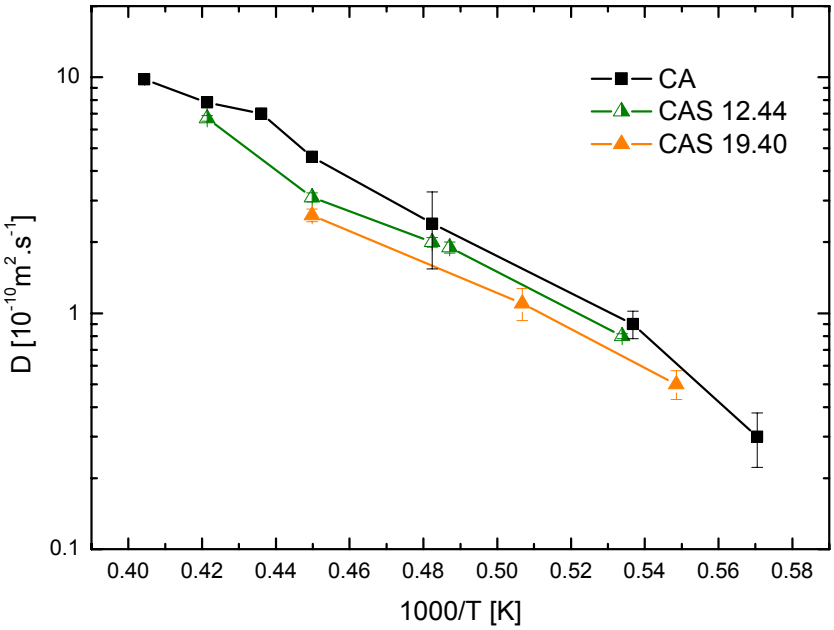

Figure 5.14 Arrhenius plot of the coherent diffusion coefficient for liquid $(CaAl_2O_4)_{1-x}(SiO_2)_x$ obtained by QENS.

We can see that the diffusion coefficient decreases upon increasing the concentration of SiO_2. This can be explained at least by two facts. The first one is that the Si atoms have a lower self diffusion coefficient compared to the other atomic species in the $(CaAl_2O_4)_{1-x}$ $(SiO_2)_x$ system as known by MD simulations [19]. The second one is that the Si atoms form SiO_4 tetrahedra which could slow down the diffusion of the other atomic species, mainly the O and Ca.

Although the number of the temperature points measured for the CAS is relatively poor, we can still attribute an Arrhenius behavior (see Fig. 5.14) to their coherent diffusion coefficients. We find an activation energy of $E_A = (1.56 \pm 0.11)$ eV/atom for CAS 12.44 and $E_A = (1.43 \pm 0.09)$ eV/atom for CAS 19.40. Compared to the E_A value for CA ($E_A = (1.8 \pm 0.1)$), We can deduce that the activation energy is decreasing upon increasing the SiO_2 content.

It is interesting to highlight that the 2073 K and 2053 K temperature points for the CAS 12.44 were performed at a working wavelength of 5.1 Å and 4.1 Å respectively. We can see that both values are in good agreement with each other, which actually show that the results obtained are independent of the wavelength used. This was also observed by comparing the respective intermediate scattering function at both wavelengths.

In order to study the fragility evolution of our $(CaAl_2O_4)_{1-x} - (SiO_2)_x$ melts upon increasing the composition x of the strong glass former SiO_2, we report our mean relaxation times (from neutron data) on an Angell plot. Since the first peak position in $S(Q)$ was observed to decrease from $Q = 2.1$ Å^{-1} (for CA) to $Q = 1.99$ Å^{-1} (for CAS 19.40), it is then convenient to have an Angell representation for these two wave vectors as shown in Fig. 5.15. Due to the small number of temperature points for the CAS compositions, it was found more adequate to extrapolate the VFT fit to both temperature limits (because more standard for later reference). Otherwise, a fit to the small number of points from only one side of the temperature scale would introduce a big uncertainty on the fragility parameters. The extracted parameters from the VFT fit (Eq. 5.4) are listed in table 13 below. The relatively large final uncertainties are not surprising since these VFT parameters result from a fit to points that themselves result from a KWW fit.

	CA (T_g=1178K)		CAS 12.44 (T_g=1137K)		CAS 19.40 (T_g=1125K)	
Q[Å^{-1}]	D	T_0	D	T_0	D	T_0
2.1	5 ± 1.8	908±85	5.71 ± 3.4	851 ± 145	5.9 ± 3.4	835 ± 140
1.9	5.5 ± 1.4	892±68	5.9 ± 3.5	842 ± 141	6.43 ± 3.7	815 ± 147

Table 13. Extracted fragility parameters for liquid $(CaAl_2O_4)_{1-x}$ $(SiO_2)_x$ from the VFT fit to the mean relaxation times around their FSDP.

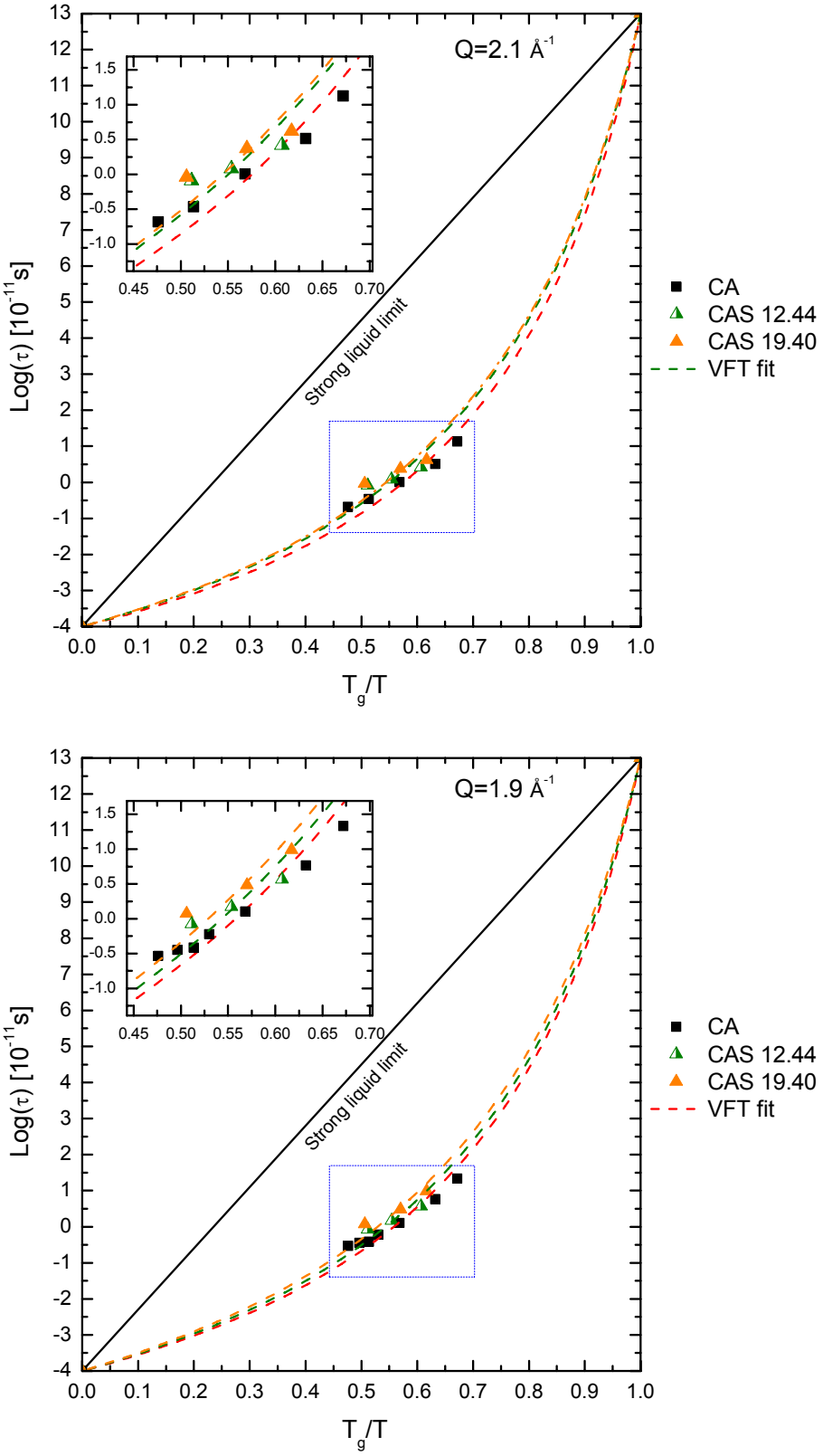

Figure 5.15 Angell representation of the mean relaxation times at $Q = 2.1$ Å^{-1} (Up) and $Q = 1.9$ Å^{-1} (Down) obtained by QENS on liquid $(CaAl_2O_4)_{1-x}$ $(SiO_2)_x$.

By inspecting Fig. 5.15, we observe that increasing the SiO_2 concentration gives rise to a stronger suppression of the dynamics together with a weaker temperature dependence of the viscosity, which actually indicates a less fragile character. This is also reflected by the increase of the fragility parameter *D* with increasing SiO_2 (Table 13).

5.1.3 Conclusion

The objective of the Quasi Elastic Neutron Scattering was to examine the structural relaxation times of the different CAS composition. The lower energies of neutrons compared to x-rays allowed QENS to probe more directly the viscosity-related slow relaxation in these oxide melts. The results showed that:

- For all the studied compositions, the intermediate scattering functions show a smooth and continuous decay in the investigated temperature range indicating a single-step process without reminiscence of cage effects.
- All the $S(Q,t)$ spectra show stretched exponential functional form and tend to a single exponential relaxations at very high temperatures.
- Contrary to the behavior of most coherent scattering liquids, the CAS melts do not present a De Gennes narrowing.
- Taking into consideration the coherent scattering nature of CA, the coherent diffusion coefficients and activation energies show good agreement with published (some unpublished) data.
- For the CA, the relaxation times at the scale of the nearest neighbor (corresponding to the FSDP) scale relatively well with the data obtained by viscosity and NMR measurements suggesting that the relaxation mechanism is the same.
- The addition of small amount of silica to the Calcium Aluminate (CA) leads to slower relaxation rates and a decrease of the coherent diffusion coefficient and corresponding activation energy.
- Increasing the SiO_2 concentration gives rise to a weaker temperature dependence of the viscosity, which in fact indicates a less fragile character. However, in order to follow further the decrease in fragility towards the strong glass limit, we would have to increase the silica content in the sample (may be more than 33%).

5.2 IXS Measurements

The dynamics of liquids are reasonably well understood in terms of two regimes of length scale L. When L is much longer than interatomic distances, corresponding to Q values close to zero, hydrodynamic theory can be applied. The other case is when L is of the same order of interatomic distances. This corresponds roughly to Q values above the first peak in $S(Q)$. In this case, we can apply kinetic theory. The intermediate region remains a challenge for modern statistical physics. Kinematic restrictions of neutron scattering make it impossible to reach a full range of energy transfers $\hbar\omega$ at low Q values. The high resolution inelastic X-ray scattering (IXS) technique goes beyond these limitations and has been widely used to study various liquids including metallic and oxide melts [20,21]. For all these studies, the data interpretation is based on generalized hydrodynamics, which is an extension of classical hydrodynamics with a frequency dependence adopted for transport coefficients like the viscosity.

5.2.1 Experimental details

As mentioned previously, the IXS experiments were performed at the ID16 beamline at the ESRF. Operating at the Si (12,12,12) reflection of the analyzers provided an incident energy of 23.725 keV and a resolution of 0.83 meV. The sample compositions measured were the same as for the QENS experiment; however, we added an additional composition, CAS 33.33 (x = 33.33) where its melting and glass transition temperatures are 1823 K and 1116 K respectively. The dynamics in approx. 180 K in the supercooled state were investigated.

The aerodynamic levitation setup is shown in Fig. 5.16 where the levitation operation is the same as described above for the neutron experiment. The chamber has a cylindrical shape made of stainless steel where a 15 mm diameter kapton window was made at the inlet of the x-ray beam. After scattering by the sample, the signal is then collected through 9 independent spherical silicon crystals (analyzers) which backscatter the beam on 9 detectors placed near the sample position. The analysers are mounted at a fixed angular position on a long arm which can rotate around the vertical scattering axis of the sample. This system allows us to collect 9 different IXS spectra simultaneously corresponding to different equidistant Q-values (Q-set). Different Q-sets are obtained by rotating the detection arm.

Since our samples required a relatively long acquisition time, we performed the measurements at only one Q-set (Q_1 = 1, 2.6, 4.3 and 5.8 nm^{-1}) that was sufficient enough to provide a good interpretation of the data. Here should be noted that for Q values above 5.8 nm^{-1}, the signal (Brillouin peaks) is no more detected. Only the CA sample was measured at two Q-sets (Q_1 and Q_2= 3, 5 and 6.6 nm^{-1}).

After placing the sample in the levitator, the chamber is pumped down to 10^{-4} mbar then filled with the levitation gas to atmospheric pressure. Along with argon, oxygen and helium were introduced with small quantities in order to reduce the attenuation of the x-ray beam due to the absorption.

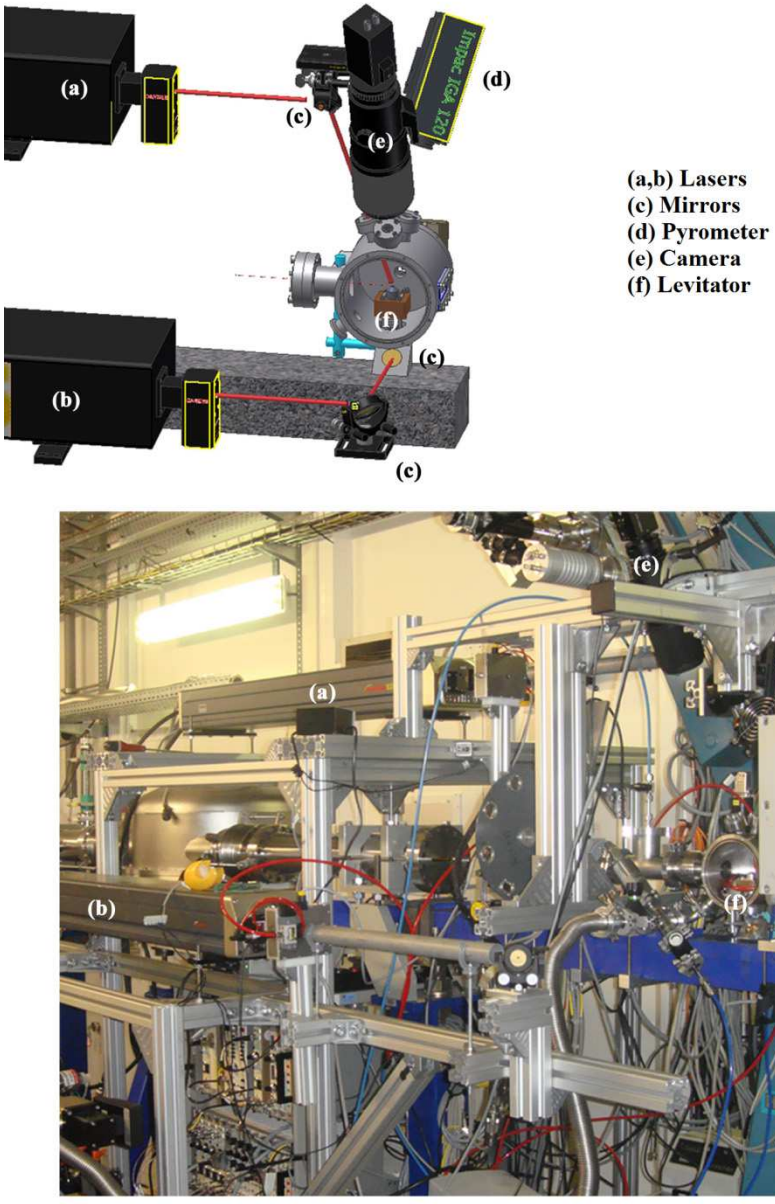

Figure 5.16 Aerodynamic levitation setup at ID16 for IXS experiments.

5.2.2 Results and Discussion

The obtained IXS spectra corresponding to the different compositions and temperatures are shown normalized in Fig. 5.17 and Fig. 5.18 for the four *Q*-values. The frequency of the excitations ranged between [-40, 40] meV; however, for clarity, the x-axis is limited to [-30, 30] meV. We can see for all the *Q*-values, the inelastic shoulders, representing acoustic phonons, are well outside the corresponding resolution function. The data were first fitted by a Damped Harmonic Oscillator (DHO) model but the fit didn't show any agreement with the experimental data. The theoretical viscoelastic model was needed to well describe the experimental values.

Since we neglected the specific heat ratio γ(Q) and the thermal relaxation time $\tau_t(Q)$ in our model (refer to section 3.2.4), we reduced the free fit parameters to four as follow:

- The overall intensity factor, A.
- The Q-dependent generalization of the isothermal sound frequency, ω_0.
- The infinite frequency sound frequency, ω_∞.
- The intensity of the instantaneous relaxation, Γ_s.

Looking at Fig. 5.17 and Fig. 5.18, we see an excellent agreement between the experimental data (black dotes) and the corresponding best fit (red line). The broadening of the Brillouin peaks increases with *Q* for the same fixed temperature.

Dispersion curves

The first fundamental information we can get from the IXS spectra is the characteristic frequency of the longitudinal acoustic modes ω_L which is the maximum of the longitudinal current spectrum $J_L(Q,\omega)$,

$$J_L(Q,\omega) = \frac{\omega^2}{Q^2} S(Q,\omega) \tag{5.5}$$

This equation is a direct consequence of the mass conservation principle for a non relativistic fluid. However, using directly the measured raw data $S(Q,\omega)$ to calculate $J_L(Q,\omega)$ is not appropriate since the instrumental resolution function has a Lorentzian shape and the obtained maxima of these currents are not visible and pronounced enough. For this reason, we use the model function of our fit deconvolued from the instrumental resolution function.

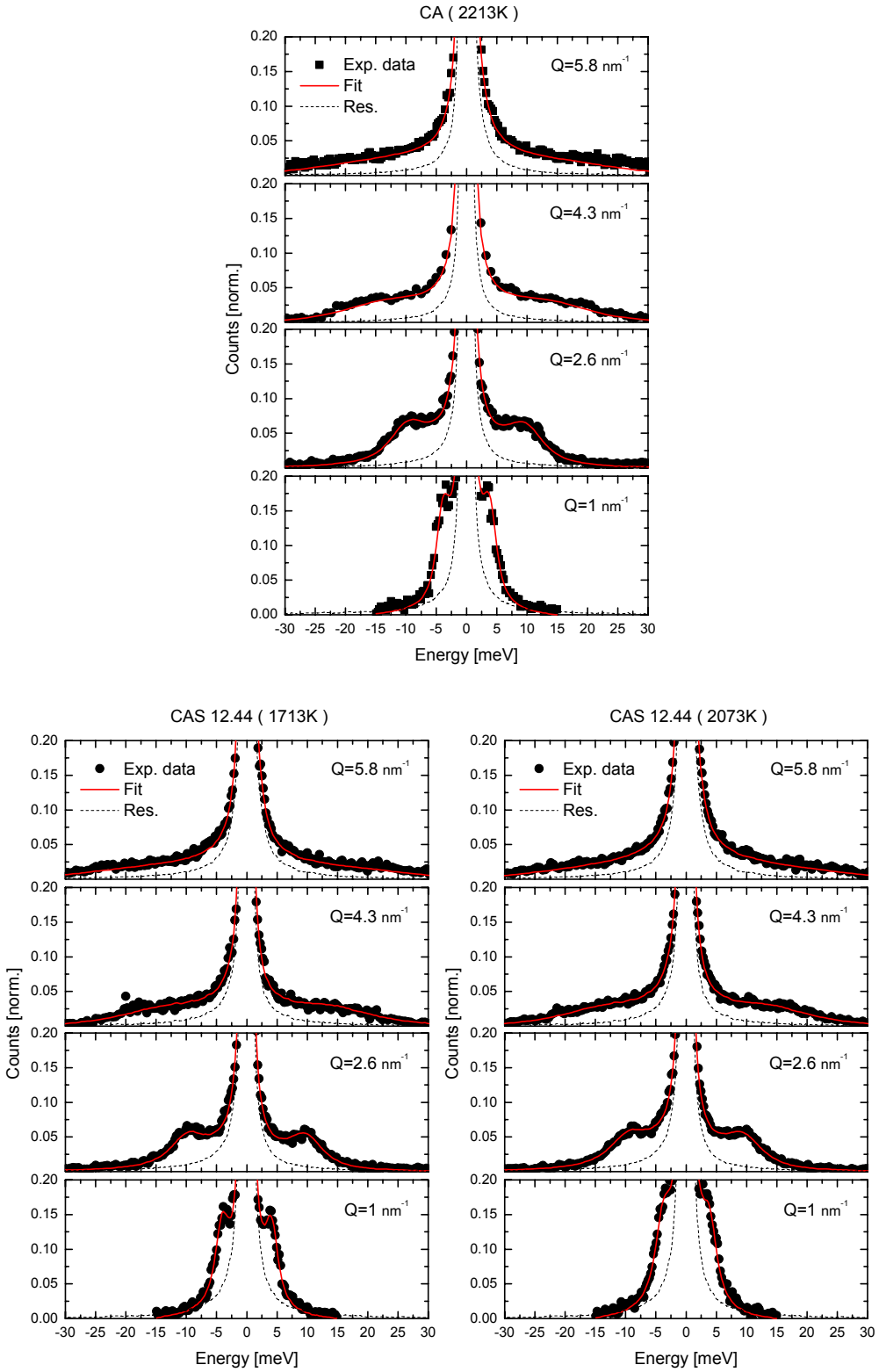

Figure 5.17 IXS spectra for CA and CAS 12.44 at the indicated temperatures and wave vectors.

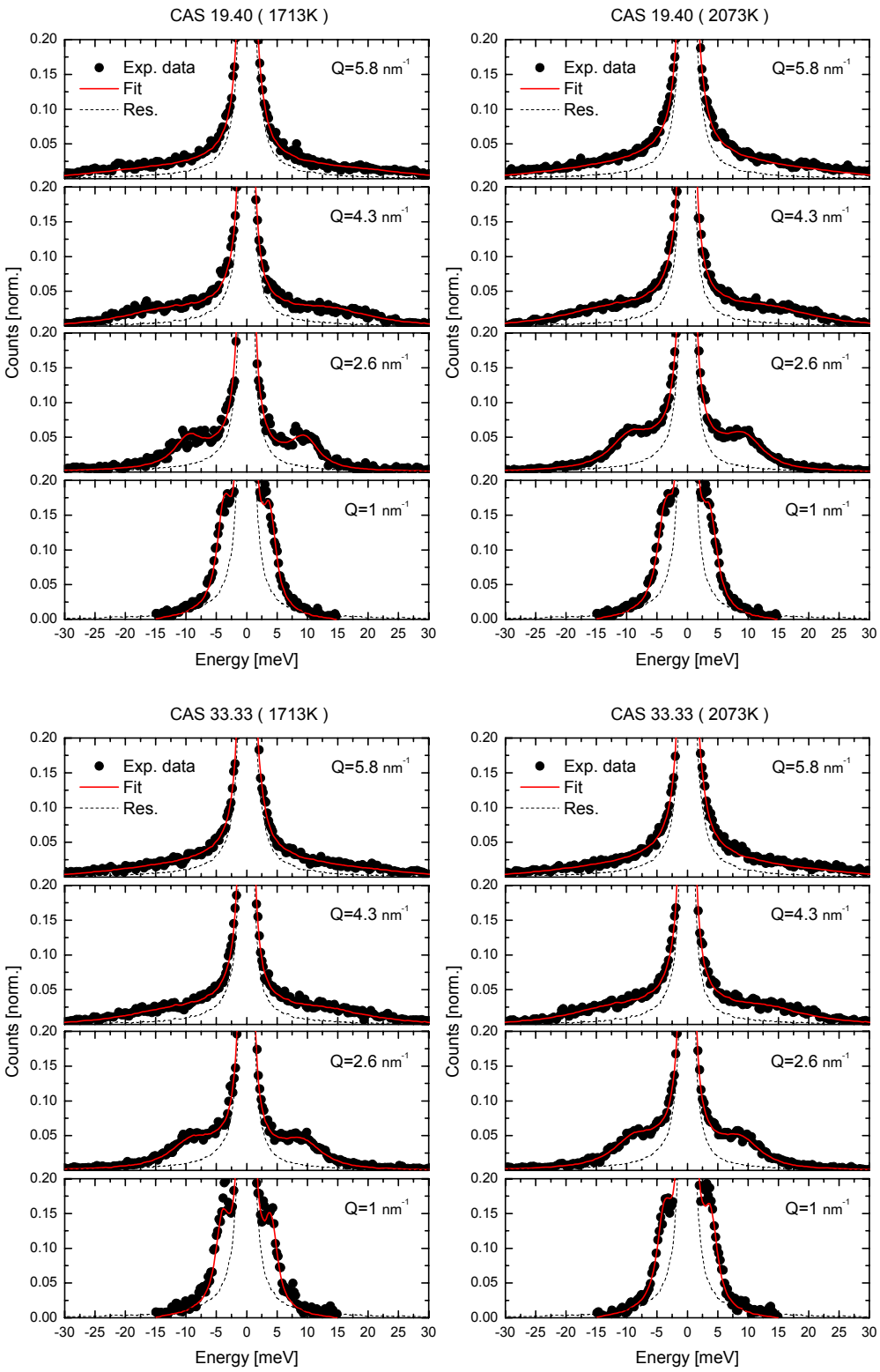

Figure 5.18 IXS spectra for CAS 19.40 and CAS 33.33 at the indicated temperatures and wave vectors.

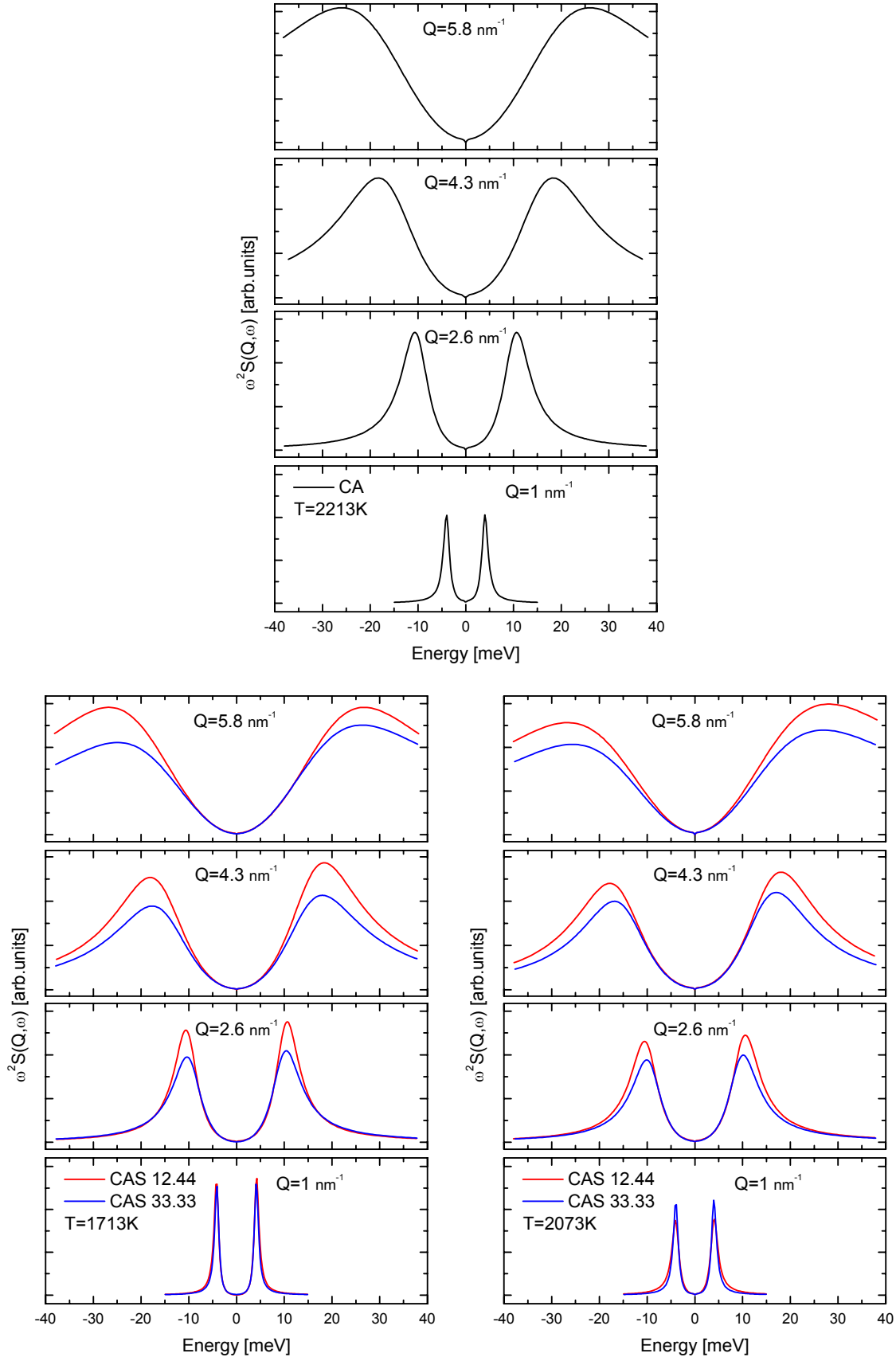

Figure 5.19 Longitudinal current spectra for all the studied compositions.

Fig. 5.19 shows the longitudinal current for selected sample compositions and temperatures. We notice by inspecting the spectra that the tails of $S(Q,\omega)$ are all well measured except at the wave vector Q = 5.8 nm^{-1} where the $S(Q,\omega)$ tail exceed the measured energy range and is not fully probed.

This will introduce a small error in our extracted fit parameters at this Q value. But the maxima ω_L of the currents are clearly visible and are depicted in Fig. 5.20 for the CA sample along with the isothermal and infinite-frequency sound frequencies.

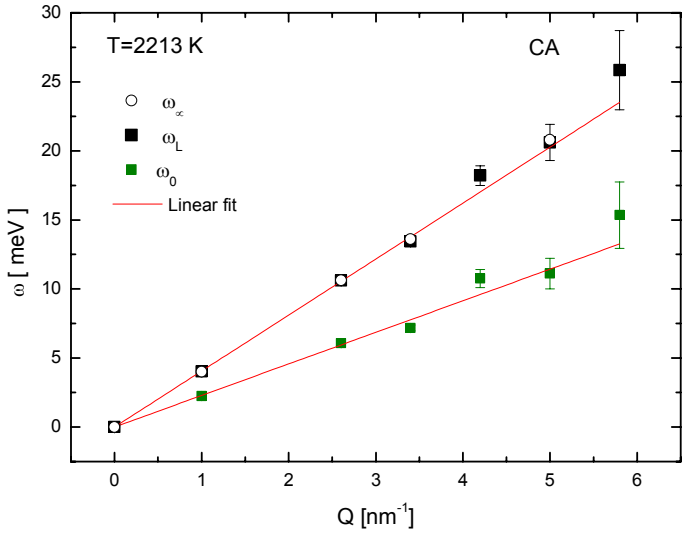

Figure 5.20 Wave vector dependence of the second frequency moment ω_0, the maxima of the longitudinal current correlation ω_L and the high-frequency limit for structural relaxation ω_∞ for $CaAl_2O_4$ (CA) at 2213K as obtained by IXS from the fitting parameters of the viscoelastic model with two time scales. The solid lines are linear fits.

We can see that all the dispersion sound frequencies exhibit a linear behaviour in the inspected Q-range. It is evident that we have an isothermal dispersion $\omega_0(Q) = c_0 Q$ that is lower than the infinite dispersion ω_∞. However, we notice that the longitudinal current dispersion joins the infinite one at the lowest Q-value measured. This means that we do not see the transition between the unrelaxed ($\omega\tau >> 1$) and the fully relaxed ($\omega\tau << 1$) regime. The frequency of the excitations is much higher than the structural relaxation rate and in this case, the liquid exhibits a purely elastic behaviour. The crossover regime ($\omega\tau \approx 1$) should be present at Q values lower than 1 nm^{-1} where the fully unrelaxed regime ($\omega\tau >> 1$) holds over all the investigated wave vectors.

The same behaviour was observed for all the compositions / temperatures studied. In Fig. 5.21, we show the low and high frequency sound frequencies for the CAS 12.44 and CAS 33.33 for the two extreme temperatures measured where they always present a linear behaviour in this low Q-range.

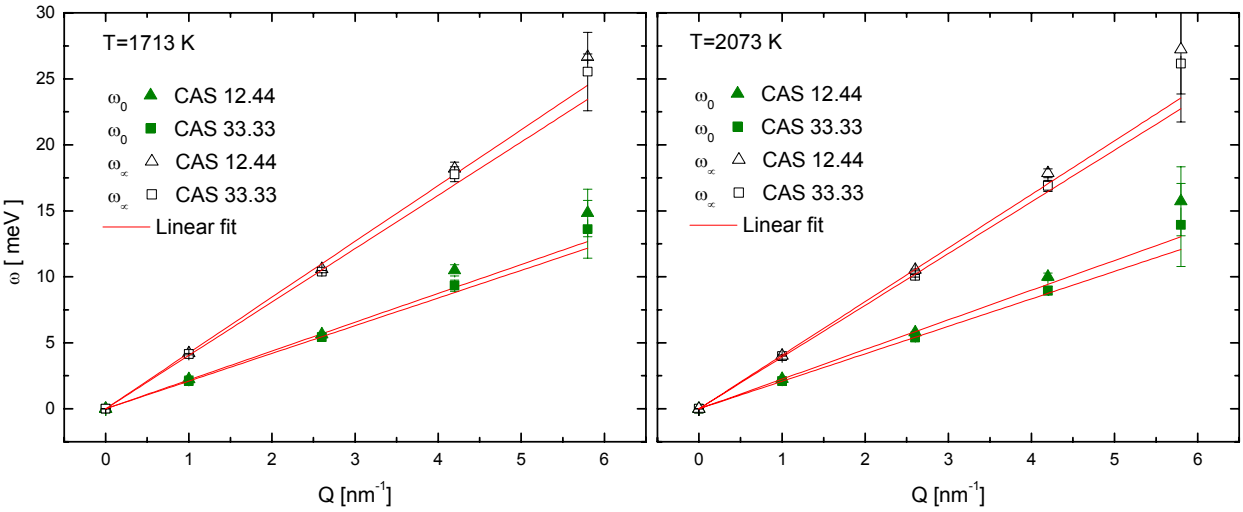

Figure 5.21 Comparison of the CAS 12.44 and CAS 33.33 zero-frequency and infinite-frequency sound frequencies for the indicated temperatures.

When interpolating all the dispersions with a linear error weighted fit:

$$\omega_{0,\mathrm{L},\infty}(Q) = c_{0,\mathrm{L},\infty} Q \tag{5.6}$$

we obtain the corresponding sound velocities. These values can be considered as a macroscopic $(Q = 0)$ property of the system since they are independent of Q.

Fig. 5.22 and Fig. 5.23 show respectively the isothermal and longitudinal sound velocities plotted against the different compositions and temperatures. For the CA at the highest temperature T = 2213 K, The best fit gives a $c_0 = 3474 \pm 37$ m/s and a $c_\mathrm{L} = 6235 \pm 53$ m/s. Comparing both velocities with regard to the compositions shows that they both have a tendency to decrease with increasing the SiO_2 content in the system. At T = 2073 K for instance, c_0 and c_L decrease by 250 and 380 m/s respectively while going from 10% to 30% of SiO_2. However, looking at their temperature dependence, both velocities show opposite trends. The low-frequency sound velocity c_0 seems to increase with temperature while the apparent velocity (longitudinal velocity) c_L decreases with temperature.

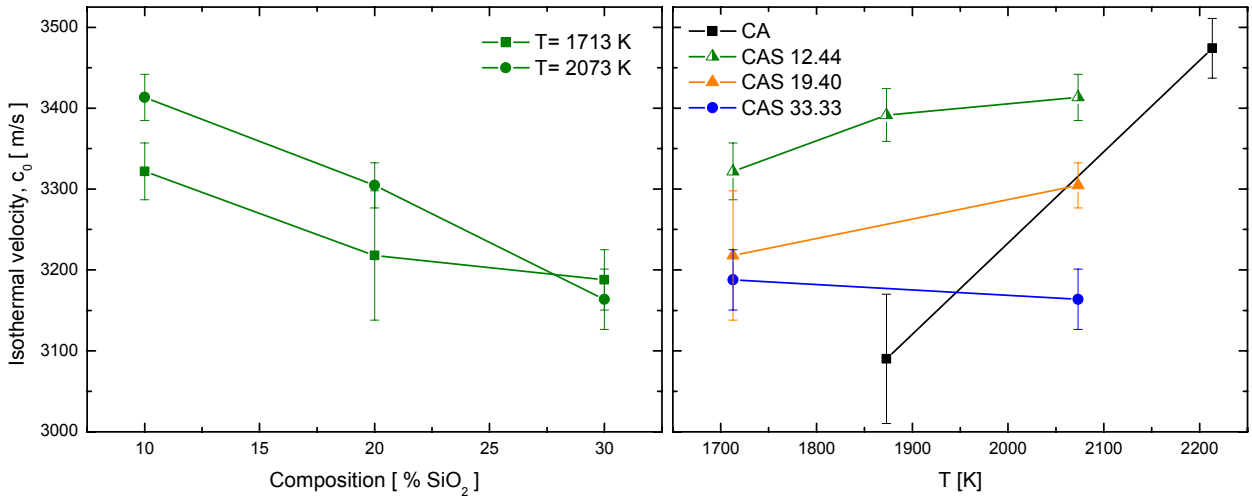

Figure 5.22 The isothermal sound velocity c_0 for the $(CaAl_2O_4)_{1-x}$ $(SiO_2)_x$ liquids as measured by IXS.

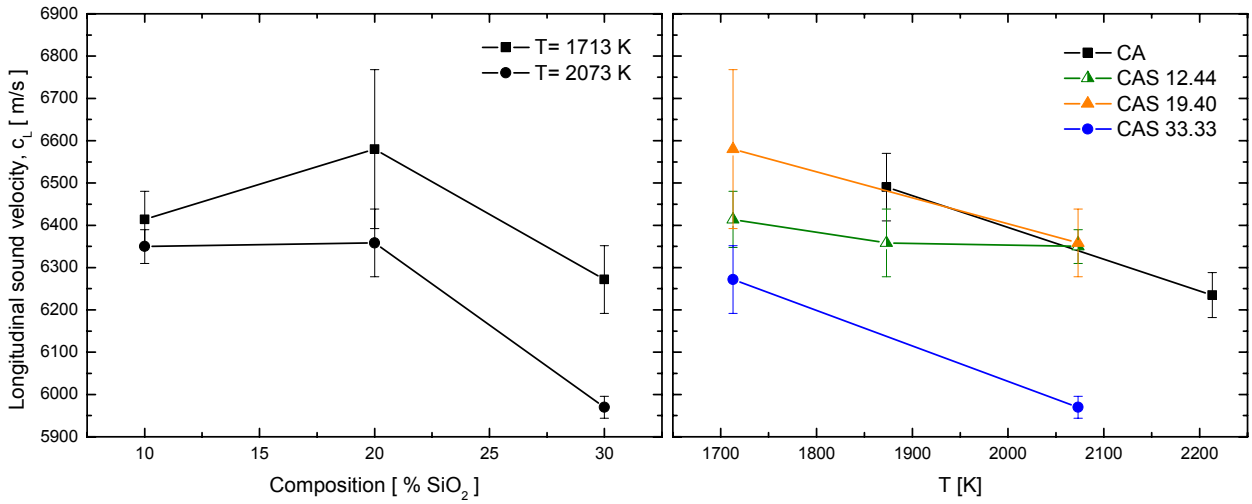

Figure 5.23 The longitudinal sound velocity c_L for the $(CaAl_2O_4)_{1-x}$ $(SiO_2)_x$ liquids as measured by IXS.

Structural relaxation

The phenomenological viscoelastic model approach (Eq. 3.56) was found to well describe the frequency and temperature dependence of the sound velocity in our glass forming liquids. Actually, in our high-frequency case, the system is probed on a timescale much shorter than the structural relaxation time τ_α and the liquid behave like an amorphous solid because the particles don't have the time to diffuse and form bonds. In this case, the acoustic wave doesn't have the time to dissipate energy in the inter-atomic interactions.

In the total memory function, the structural relaxation is described by an exponential time decay with the time constant τ_α (Eq.3.59). In the hydrodynamic limit ($t \to \infty$ or $Q \to 0$), the exponential reduces to a delta function. So in order to fulfill the hydrodynamic limit, the viscoelastic model assumes that the relaxation time is linked to the width of the Rayleigh peak Γ by $\Delta_\alpha^2 \tau_\alpha = \Gamma Q^2$ where $\Delta_\alpha^2 = \omega_\infty^2 - \omega_0^2$ is the structural relaxation strength.

Fig. 5.24 shows the *Q*-dependence of the structural relaxation time $\tau_\alpha(Q)$ thus obtained for Calcium Aluminate at the highest temperature *T* = 2213 K. Similarly to the QENS experiment, we observe that $\tau_\alpha(Q)$ decreases with increasing *Q*. The red line is an exponential decay fit and we see that it describes well the data. If we extrapolate the $\tau_\alpha(Q)$ to $Q = 0$ using the exponential decay equation, we get a value of $\tau_\alpha = 5.1 \pm 0.23$ ps. The QENS experiment on CA at approx. the same temperature yielded a mean relaxation time of 6.1 ps at the highest Q measured ($Q = 1.9$ Å^{-1}, Fig. 5.8). We see that both QENS and IXS relaxation times are within the same order of magnitude where the structural relaxation at this temperature is tracked down to few picoseconds.

The relaxation times for CAS 12.44 and CAS 33.33 are presented in Fig. 5.25 for two lower temperatures. Looking at the $\tau_\alpha(Q)$ for the CAS 33.33 at the right hand side of Fig. 5.25, we can see that the data are noisier than that of CA where $\tau_\alpha(Q)$ does not follow exactly a proper exponential decay. The red lines in the figure should only be considered to be a guide to eye. The reason for this can be due to many artifacts. One remarkable observation is the relatively larger errors at $Q = 1$ nm^{-1} where the two Brillouin shoulders are very close to the central peak (Fig. 5.17, 5.18). This is well observed in the case of CAS 12.44 at the left hand side of Fig. 5.25 where the $\tau_\alpha(Q = 1\,\mathrm{nm}^{-1})$ at the lowest temperature *T* = 1873 K present a higher error than that of the one at *T* = 2073 K. This is because we are getting close to the resolution function of the instrument. Nevertheless, the tau data were as well fitted and extrapolated to $Q = 0$ with an exponential decay function. $\tau_\alpha(Q = 0)$ values are compared to the QENS $\langle\tau\rangle(Q)$ (around the FSDP) in table 14.

Composition	T [K]	τ_α [ps] (IXS) $(Q \to 0)$	$\langle\tau\rangle$ [ps] (QENS) $Q = 2.4$ Å^{-1}	$Q = 2.1$ Å^{-1}	$Q = 1.9$ Å^{-1}
CA	2223 (±30)	5.1 ± 0.23	--	--	6.1
CAS 12.44	2073 (±30)	14.9 ± 6.6	8.12	12.1	14.9
CAS 12.44	1873 (±30)	40 ± 20	22.2	26.2	36.8

Table 14. Comparison between the $Q = 0$ extrapolated structural relaxation time obtained by IXS and the mean relaxation time around the FSDP obtained by QENS.

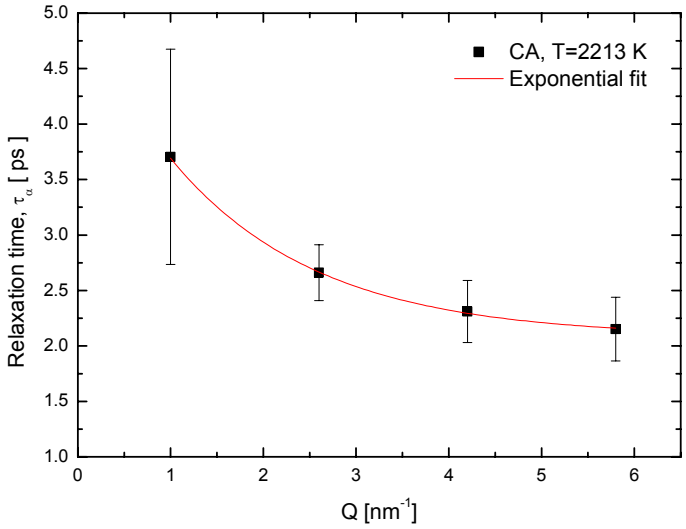

Figure 5.24 Structural relaxation times for $CaAl_2O_4$ at 2213 K obtained by IXS. The solid line is an exponential fit.

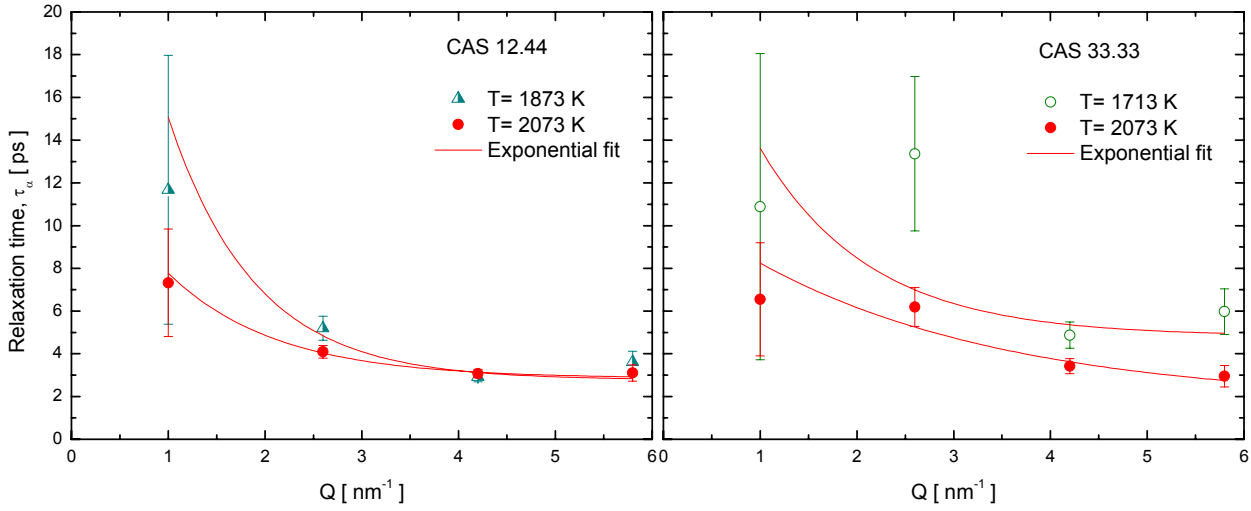

Figure 5.25 Structural relaxation times for CAS 12.44 (left) and CAS 33.33 (right) as obtained by IXS. The solid line is an exponential fit.

Longitudinal viscosity

The generalized Q-dependent viscosity $\eta_l(Q)$ can be extracted from the memory function parameters by:

$$\eta_l(Q) = \frac{\rho[\Delta_\alpha^2(Q)\tau_\alpha(Q) + \Gamma_S(Q)]}{Q^2} \tag{5.7}$$

The structural relaxation length, $\Delta_\alpha^2(Q)$, is responsible for the sound wave velocity increase from c_0 to $\sqrt{c_0^2 + \Delta_\alpha^2}$. Once the fitting parameters of the memory function are obtained, one can calculate $\Delta_\alpha^2(Q)$ which is related to the isothermal and infinite-frequency sound velocities through $\Delta_\alpha^2(Q) = [c_\infty^2(Q) - c_0^2(Q)]Q^2$. The second contribution to the longitudinal viscosity is the instantaneous relaxation. This type of relaxation is usually called "microscopic" relaxation and is associated to the extremely fast dynamics in the system resulting from the atomic vibrations. Additional very short time relaxations can add up to the $\Gamma_S(Q)$ term as well due to the fact that our system is fully unrelaxed. Actually, the plane wave of the incident excitation upon facing the elastic response from the system, will decompose into different eigenstates of different frequencies that will dephase each other over time and give rise to a very short characteristic timescale. The integrated intensity of $\Gamma_S(Q)$ can be obtained from the fitting procedure.

Fig. 5.26 shows the partial contributions to the longitudinal viscosity from the slow i.e. τ_α (structural) and the fast i.e. Γ_S (instantaneous) components for e.g. the CAS 12.44 at the two measured temperatures. We can observe that the viscosity associated to the structural relaxation is almost 40 times the high-frequency one. In addition to this, $\Delta_\alpha^2(Q)\tau_\alpha(Q)$ looks more temperature dependent than $\Gamma_S(Q)$. One can proceed in many ways to derive a Q-independent viscosity (i.e. an exponential dependence of $\eta_l(Q)$). We have chosen to fit both contributions with a quadratic function and the obtained longitudinal viscosities can thus be compared to macroscopic ones.

		η_l[mPa.s]		
T [K]	CA	CAS 12.44	CAS 19.40	CAS 33.33
1713	--	155 ± 8	143 ± 17	207 ± 18
1873	--	116 ± 12	--	--
2073	--	116 ± 6	111 ± 54	119 ± 12
2213	83 ± 4	--	--	--

Table 15. Longitudinal viscosities of $(CaAl_2O_4)_{1-x}$ $(SiO_2)_x$ liquids as obtained from IXS through the generalized hydrodynamic model.

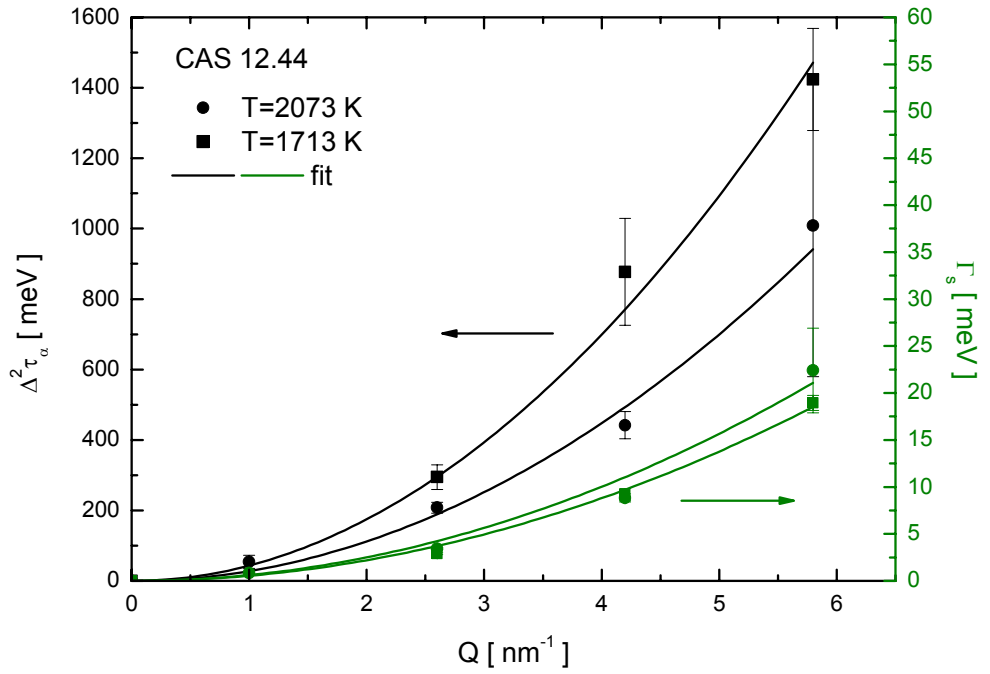

Figure 5.26 The quadratic behavior of the partial contributions to the longitudinal viscosity from the slow (structural) and the fast (instantaneous) components for the CAS 12.44 at 1713K and 2073K.

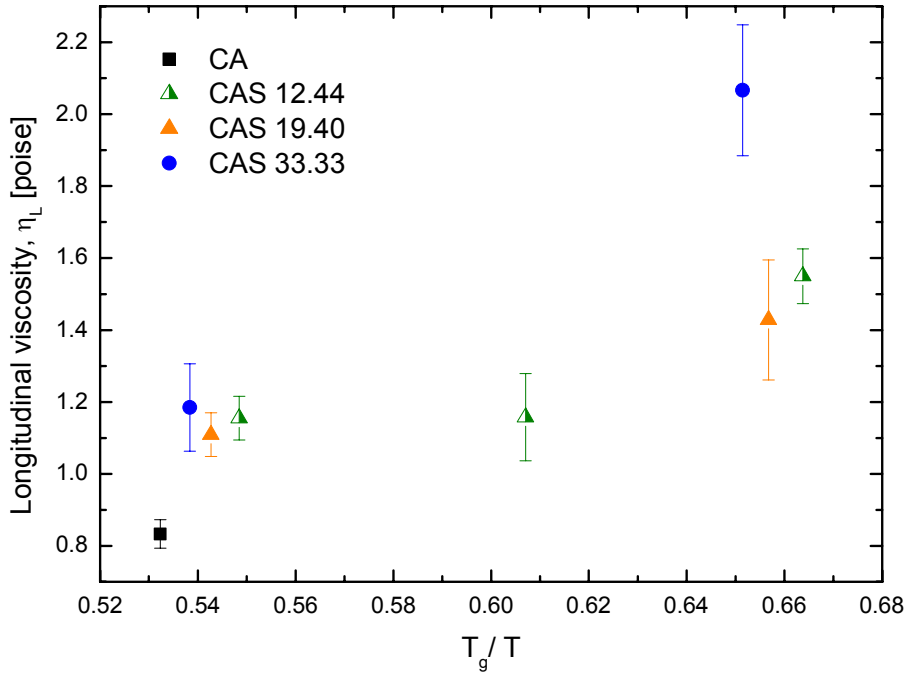

Figure 5.27 Angell representation of the longitudinal viscosities of liquid $(CaAl_2O_4)_{1-x}$ $(SiO_2)_x$ as obtained from IXS.

The longitudinal viscosities calculated are listed in table 15. For Calcium Aluminate at 2213K, we obtained a value of $\eta_l = (83 \pm 4)$ mPa.s. which is in the same order of magnitude of the macroscopic shear viscosity $\eta_s \approx 49$ mPa.s. measured by Urbain [11]. In many simple liquids, the ratio between these two viscosities is observed to be almost constant as a function of temperature [22-26]. In our case, we found a ratio of $\eta_l / \eta_s = 1.7$. Unfortunately, we didn't find published viscosity data at very high temperature for the CAS in the public domain in order to compare our η_l obtained from IXS.

Fig. 5.27 shows an Angell representation of the obtained viscosities where η_l is plotted as a function of inverted temperature normalized to the corresponding T_g for each composition. The lack of sufficient measured temperature points explains why the data are not fitted with a VTF function. However, by inspecting the graph, one can observe several important points. The viscosities increase and present the expected trend while lowering the temperature. At high temperatures, the three CAS compositions show similar viscosities, whereas at lower temperatures, we see a bigger dispersion. Finally, an important point to highlight is that the highest silicate content CAS 33.33 shows a pronounced deviation from the other two CAS compositions that show comparable values, indicating a pronounced decrease in fragility.

.

5.2.3 Conclusion

The objective of the Inelastic X-ray Scattering was to examine the dispersion relations of the different CAS composition. This allowed us to calculate the longitudinal viscosities through the generalized hydrodynamics theory. The results showed that:

- The infinite frequency dispersion exhibits a quasi linear behavior over the entire *Q*-range studied, i.e. c_∞ is quasi *Q*-independent.
- The longitudinal current and infinite-frequency dispersions coincide at all the inspected wave vectors. The crossover regime between unrelaxed and fully relaxed regime appeared to be at *Q* values lower than 1 nm^{-1}, and therefore outside of our measured *Q* range.
- The isothermal velocity increases with temperature while the longitudinal sound velocity decreases.
- Both, the isothermal and the longitudinal sound velocities decrease with an increase of the SiO_2 content in the CAS.
- The structural relaxation times show an exponential decay. The extrapolated values $\tau_\alpha(Q=0)$ are within the same order of magnitude of the relaxation times obtained from QENS measurements near the first diffraction peak.
- The structural relaxation time dominates the contribution to the longitudinal viscosity.

- At the lowest temperature, the viscosity of CAS 33.33 shows a pronounced deviation from that of the other (lower SiO_2) CAS that were found to have close values, implying a pronounced decrease in fragility for CAS 33.33.

REFERENCES

[1] A. Arbe and J. Colmenero, Phys. Rev. E 80, 041805 (2009).

[2] R. Perez-Aparicio, A. Arbe, F. Alzarez, J. Colmenero and L. Willner, Macromolecules 42, 8271-8285 (2009).

[3] M. Brodeck, F. Alvarez, A. Arbe, F. Juranyi, T. Unruh, O. Holderer, J. Colmenero and D. Richter, J. Chem. Phys. 130, 094908 (2009).

[4] J. Wuttke and W. Petry, J. Chem. Phys. 12, 105 (1996).

[5] J. Wuttke and W. Petry, J. Chem. Phys. 12, 105 (1996).

[6] A. Tolle, Rep. Prog. Phys. 64, 1473-1532 (2001).

[7] F. Demmel, A. Diepold, H. Aschauer and C. Morkel, phyc. Rev. B 73, 104207 (2006).

[8] www.ill.fr/YellowBook/IN6/

[9] J. W. E. Drewitt, S. Jahn, V. Cristiglio, A. Bytchkov, M. Leydier, S. Brassamin, H. E. Fischer, L. Hennet, J. Phys. Cond. Mat., 23 155101 (2011).

[10] P. G. deGennes, Physica (Amsterdam) 25, 825 (1959).

[11] G. Urbain, Rev. Int. Hautes Temp. Réfract., **20**, p135-139 (1983).

[12] www.ill.fr/YellowBook/IN8/

[13] S. Jahn et al. (unpublished)

[14] S. Magazu, F. Migliardo et M. Telling, J. Phys. Chem. B 110, p. 1020 (2006).

[15] B. T. Poe, P. F. McMillan, B. Coté, D. Massiot, J-P. Coutures, J. Am. Ceram. Soc, **77**, p1832-1838 (1994).

[16] D. Massiot, D. Trumeau, B. Touzo, I. Farnan, J-C. Rifflet, A. Douy and J-P. Coutures, J. Phys. Chem. 99, 16455-16459 (1995).

[17] L. Hennet, I. Pozdnyakova, V. Cristiglio, G. J. Cuello, S. Jahn, S. Krishnan, M-L.

Saboungi and D. L. Price, J. Phys. Condens. Matter 19 455210 (2007).

[18] K. L. Ngai, J. Non-Cryst. Solids **275**, 7-51 (2000).

[19] N. Jakse et al. (unpublished)

[20] T. Scopigno, G. Ruocco and F. Sette, Rev. Mod. Phys., 77, 881 (2005).

[21] I. Pozdnyakova, L. Hennet, J. Brun, D. Zanghi, S. Brassamin, V. Cristiglio, D. Price, F. Albergamo, A. Bytchkov, S. Jahn, and M. Saboungi, J. Chem. Phys. p.126, 114505 (2007).

[22] E. Herzfeld and T.A. Litovitz; Absorption and Dispersion of Ultrasonic Waves, (Accademic Press, New York) 1959.

[23] G. Monaco, A. Cunsolo, G. Ruocco and F. Sette, Phys. Rev. E, 60 5505 (1999).

[24] C.M. Davis and T.A. Litovitz; Physical Acoustics, W.P. Mason, New York (1969).

[25] J. Rouch, G.C. Lai and S.H. Chen, J. Chem. Phys., 65, 4016 (1976).

[26] J.O. Hirschfeld, C.F. Curtiss and R.B. Bird; Molecular Theory of Gasses and Liquids, John Wiley & Sons, New York (1954).

CONCLUSIONS AND RECOMMENDATIONS FOR FUTURE WORK

To help advance the study of liquids at very high temperatures, it was deemed worthwhile to extend the aerodynamic levitation technique to Inelastic Neutron Scattering, a successful enterprise that has enriched the study of the dynamics of molten oxides.

The objective of the present work was to conduct structural and dynamical investigations on Calcium AluminoSilicate $(CaAl_2O_4)_{1-x}$ $(SiO_2)_x$ liquids in order to give more insight into their fragility as a function of SiO_2 content and to follow the rapid change in their dynamical properties like viscosity while approaching T_g. Different compositions were studied at very high temperatures down to the supercooled regime by means of Neutron Diffraction, X-ray diffraction, Quasi-Elastic Neutron Scattering and Inelastic X-ray Scattering.

In the goal of performing QENS experiments on our high-temperature levitated oxides, numerical CFD models were first developed in order to design a new optimized version of the aerodynamic levitation technique that overcame earlier restrictions to small sample sizes, thus enabling the QENS measurements presented here and which are in fact the first QENS results for levitated molten oxides.

By performing both x-ray and neutron scattering experiments, we were able to exploit not only a greater range of scattering length contrast, but also a wider range of time and energy scales. For example, the lower energies of neutrons compared to x-rays allowed QENS measurements to probe more directly the viscosity-related slow relaxation in oxide melts.

In contrast to the readily quantified variations in dynamical properties as a function of temperature and composition, we observed relatively minor variations in local chemical order from the structural measurements (XRD, ND). This could be explained in part by the rather high sensitivity of dynamical properties to minor structural modifications in general, or it could be a signal that the structural aspects which we probed less precisely, namely the O-O and Ca-O pair correlations, are the most implicated in the observed variations of the dynamical

properties. For example, due to its larger scattering length and high concentration in our compositions, the oxygen atom would contribute greatly to the measured dynamical properties and perhaps even play a dominant role. In addition, our structural measurements cannot determine very accurately the amount of AlO_5 created when adding SiO_2 to the sample composition (but here NMR would give an accurate answer), and it's possible that the AlO_5 motif plays an important role in the observed dynamics. Finally, as mentioned earlier, we hope to perform Ca-edge EXAFS experiments to probe with more sensitivity the structural environment of the Ca atoms.

As presented in the Dynamics chapter, our QENS results for relaxation time as a function of temperature match closely those from published NMR measurements sensitive to only the Al atom dynamics. Such a convergence of results strongly suggests that the two techniques are probing the same or related microscopic properties which could be elucidated via accurate simulation work, such as Ab-Initio Molecular Dynamics (AIMD). However, due to a few unlucky events (e.g. reactor shutdowns) amounting to a delay of almost 2 years towards performing our neutron diffraction measurements, there was not enough time during this thesis work to use $S(Q)$ data for AIMD simulation work or as a complement to QENS data. Such simulations on SiO_2-doped CA represent therefore a promising area of future work.

Finally, to reiterate a point made in the introductory chapter, this thesis work was not limited to obtaining and analyzing results from various experimental techniques, but also emphasized instrumentation development, in particular the design and construction of the aerodynamic levitation technique for QENS measurements. As a result, this thesis not only presents scientific results on the structure and dynamics of CAS systems, but also offers to the neutron scattering community a new tool for future dynamical studies of high-temperature liquids.

CONCLUSION ET PERSPECTIVES (FRANÇAIS)

Afin de faire progresser l'étude des liquides à très hautes températures, un objectif instrumental de ce travail de thèse était d'associer la technique de lévitation aérodynamique avec chauffage par laser à des mesures de diffusion inélastique des neutrons, une technique importante qui nous a permis d'enrichir l'étude de la dynamique des oxydes fondus.

L'objectif scientifique de ce travail était de mener des études structurales et dynamiques sur des aluminosilicates de calcium $(CaAl_2O_4)_{1-x}$ $(SiO_2)_x$ à l'état liquide afin de mieux comprendre leur fragilité en fonction de la composition en SiO_2 et donc, de suivre l'évolution rapide de leur propriétés dynamiques, comme la viscosité à l'approche de T_g. Plusieurs compositions ont été étudiées à des températures très élevées et aussi dans le régime de surfusion en utilisant les techniques de diffraction des neutrons (ND) et des rayons X (XRD), diffusion quasi-élastique des neutrons (QENS) et diffusion inélastique des rayons X (IXS).

Dans le but de réaliser nos expériences de QENS sur les oxydes à très haute température en lévitation, des modèles de simulation numérique CFD ont d'abord été développées afin de concevoir une nouvelle version optimisée de la buse de lévitation aérodynamique. Le nouveau montage a permis de dépasser les restrictions antérieures pour les échantillons de petites tailles, permettant ainsi les mesures QENS présentées ici et qui sont en fait les premiers résultats QENS vraiment exploitables sur des oxydes fondus en lévitation réalisées sur un spectromètre en temps de vol.

En effectuant des mesures de diffusion inélastique des neutrons et aussi des rayons X, on a pu exploiter non seulement une grande gamme de longueurs de diffusion mais aussi une large gamme de temps et d'énergies. Par exemple, l'énergie plus faible des neutrons comparé à celles des rayons X a permis de sonder plus directement les temps de relaxation liés à la viscosité dans ces oxydes fondus.

Contrairement aux variations facilement détectées dans les propriétés dynamiques en fonction de la température et de la composition, nous n'avons observé que des variations relativement mineures dans l'ordre chimique local à partir des mesures structurales (XRD, ND). Cela

pourrait s'expliquer en partie par la sensibilité assez élevé des propriétés dynamiques à ces modifications structurales mineures en général, ou cela pourrait montrer que tous les aspects structuraux que nous avons sondés de façon moins précise, notamment les corrélations de paires O-O et Ca-O, pourrait-être les plus impliquées dans les variations observées dans les propriétés dynamiques. En fait, due à sa grande longueur de diffusion et son importante concentration dans nos compositions, l'atome d'oxygène contribue largement aux propriétés dynamiques mesurées et devrait même jouer un rôle dominant. De plus, les techniques de diffraction utilisées dans notre étude structurale donne une information globale et n'ont pas permis de quantifier d'une manière précise la proportion d'AlO_5 formée lors de l'ajout de la silice dans la composition de nos échantillons (mais ici la technique RMN donne une réponse bien plus précise), et il est probable que le motif d'AlO_5 joue un rôle important dans le comportement des propriétés dynamiques observées. Enfin, comme mentionné précédemment, nous espérons effectuer des mesures d'EXAFS au seuil de l'atome Ca afin de pouvoir sonder avec plus de précision l'environnement structural autour du calcium.

Comme nous l'avons montré dans le chapitre sur la dynamique, les temps de relaxation obtenus par nos mesures QENS sont en bon accord avec les données publiées obtenues par les mesures RMN de l'aluminium, qui est donc seulement sensible à la dynamique de l'atome Al. Une telle convergence des résultats suggère fortement que les deux techniques tentent de sonder des propriétés microscopiques identiques ou très liées entres elles. Cela pourrait être élucidé grâce à un travail de modélisation précis en utilisant des méthodes de simulation comme la Dynamique Moléculaire classique (MD) ou *ab-initio* (AIMD). Toutefois, en raison de quelques événements non-contrôlables (arrêts du réacteur, par exemple) qui a causé un délai de plus de deux ans avant de pouvoir effectuer nos mesures de diffraction de neutrons, nous n'avons pas eu suffisamment de temps au cours de cette thèse pour modéliser les données structurales (facteurs de structure $S(Q)$) par des simulations MD et AIMD, ce qui nous aurait aussi permis de complémenter nos mesures de QENS et IXS. La réalisation de telles simulations sur ces CAS constituent donc une suite importante et nécessaire à donner à ce travail expérimental.

Finalement, pour rappeler un point déjà mentionné au début, ce travail de thèse ne s'est pas limité juste à l'obtention et l'analyse des résultats provenant de diverses techniques expérimentales mais a montré que la technique de la lévitation aérodynamique a prouvé sa capacité à permettre des mesures de diffusion inélastique des neutrons sur les oxydes et qu'elle constitue un nouvel outil pour la communauté scientifique pour l'étude de la dynamique des liquides à haute température.

Jad KOZAILY

Structure et dynamique d'aluminosilicates de calcium fondus

Résumé :

L'étude des silicates fondus présente un intérêt dans divers domaines de recherche comme la géologie ou la fabrication des verres avec des applications technologiques importantes telles que par exemple, le confinement des déchets nucléaires. Ces recherches demandent des informations fondamentales sur la structure et la dynamique de ces liquides au niveau microscopique mais l'acquisition des données est très souvent limitée par les températures de fusion élevées des composés étudiés. Notre travail s'est donc basé sur l'utilisation de techniques sans contact afin de s'affranchir de cette difficulté.

Dans le cadre de cette thèse, nous nous sommes intéressés à l'étude des propriétés structurales et dynamiques de divers aluminosilicates de calcium (CAS) fondus. Pour cela, nous avons développé un dispositif utilisant la lévitation aérodynamique afin d'effectuer des expériences de diffusion quasi-élastique des neutrons. En combinant ces mesures avec la diffusion inélastique des rayons X, nous avons pu obtenir des résultats sur la dynamique microscopique des CAS à l'état liquide ainsi que dans le régime de surfusion. En particulier, nous avons pu déterminer l'évolution de la viscosité avec la température et les coefficients de diffusion cohérents. Nous avons pu aussi étudier l'évolution de la dynamique de ces verres en fonction de l'augmentation de la quantité de silice dans la composition.

En parallèle de nos travaux sur la dynamique, nous avons aussi réalisé des expériences de diffraction de neutrons et de rayons X sur les mêmes compositions et températures afin d'examiner l'ordre atomique local et essayer de le corréler aux propriétés dynamiques observées.

Mots clés : Calcium aluminosilicates, Liquides, Lévitation, Diffusion inélastique, Diffraction

Structure and dynamics of calcium aluminosilicate melts

Summary:

Because of their interesting properties as glass-forming systems, molten silicates play an important role in the geology of the Earth's crust and mantle and are also of industrial interest for nuclear waste treatment. Research in these areas requires fundamental information on the microscopic structure and dynamics of silicate melts, but such measurements are hampered by the very high melting points of these systems.

By extending the technique of aerodynamic levitation to inelastic neutron scattering, and also making use of inelastic synchrotron x-ray scattering, we have obtained results on the microscopic dynamics of silicates both above the melting point and in the supercooled regime. In particular, we have determined the temperature evolution of the viscosity and diffusion coefficient of calcium aluminosilicates, and thereby quantified the decrease in fragility of this glass-forming system as a function of increasing silica content.

In parallel with our dynamical studies, we have performed x-ray and neutron diffraction experiments on the same compositions and temperatures in order to examine the local chemical order pertinent to the observed dynamical properties.

Keywords : Calcium aluminosilicates, Liquids, Levitation, QENS, Diffraction

Institut Laue Langevin (ILL)
6, rue Jules Horowitz BP 156
38042 Grenoble Cedex 9, France

CEMHTI site HT
1d, avenue de la Recherche Scientifique
45071 Orléans Cedex 2, France